

Universiteit
Leiden
The Netherlands

Simulations of biopolymer networks under shear

Huisman, E.M.

Citation

Huisman, E. M. (2011, April 14). *Simulations of biopolymer networks under shear*. *Casimir PhD Series*. Lorentz Institute for Theoretical Physics, Faculty of Science, Leiden University. Retrieved from https://hdl.handle.net/1887/16716

Version:	Corrected Publisher's Version
License:	Licence agreement concerning inclusion of doctoral thesis in the Institutional Repository of the University of Leiden
Downloaded from:	https://hdl.handle.net/1887/16716

Note: To cite this publication please use the final published version (if applicable).

Simulations of biopolymer networks under shear

P R O E F S C H R I F T

ter verkrijging van
de graad van Doctor aan de Universiteit Leiden,
op gezag van Rector Magnificus prof. mr. P. F. van der Heijden,
volgens besluit van het College voor Promoties
te verdedigen op donderdag 14 april 2011
klokke 13.45 uur

door

Elisabeth Margaretha Huisman

geboren te Leeuwarden
in 1982

Promotiecommissie:

Promotor:	prof. dr. G. T. Barkema
Co-Promotor:	dr. C. Storm (Technische Universiteit Eindhoven)
Overige leden:	prof. dr. F. C. MacKintosh (Vrije Universteit Amsterdam)
	prof. dr. M. L. van Hecke
	prof. dr. H. Schiessel
	prof. dr. J. van Ruitenbeek

Casimir PhD Series, Delft-Leiden 2011-05
ISBN 978-90-8593-096-9

voor mijn ouders

CONTENTS

1 Introduction **1**
- 1.1 Polymer networks in biology . . . 2
  - 1.1.1 Biopolymers . . . 2
  - 1.1.2 Biopolymer structures in cells . . . 2
  - 1.1.3 Extracellular structures . . . 4
  - 1.1.4 Experiments on biopolymer networks . . . 6
- 1.2 Elastic and viscous modulus . . . 8
- 1.3 Non-affinity . . . 11
- 1.4 Models of single filaments . . . 13
  - 1.4.1 Freely jointed chain . . . 14
  - 1.4.2 Semiflexible worm-like chain . . . 15
- 1.5 Models of biopolymer networks . . . 17
  - 1.5.1 Single-filament based models . . . 17
  - 1.5.2 Network based models in two dimensions . . . 19
- 1.6 Methods used in this thesis . . . 23
  - 1.6.1 The Monte Carlo method . . . 23
  - 1.6.2 Relaxation method . . . 25
  - 1.6.3 Dynamical matrix . . . 26
- 1.7 Overview of this thesis . . . 28

2 Generation of networks **31**
- 2.1 Introduction . . . 32
- 2.2 Network generation and equilibration . . . 33
  - 2.2.1 Network free energy . . . 33
  - 2.2.2 Interpolation formula for the segment free energy . . . 36
  - 2.2.3 Network generation . . . 37
- 2.3 Mechanical response of the network . . . 39
  - 2.3.1 Strain stiffening . . . 41
  - 2.3.2 Non-affine behavior and ordering . . . 44
  - 2.3.3 Collective rearrangements . . . 51
- 2.4 Conclusions . . . 53

3 Deformation of composite networks **55**
3.1 Introduction . . . 56
3.2 Setup of the numerical simulations . . . 58
3.3 Results . . . 58
3.3.1 Composites at low fraction of stiff filaments . . . 60
3.3.2 Percolation . . . 62
3.4 Conclusions . . . 63

4 Internal stresses, normal modes and non-affinity of networks **65**
4.1 Introduction . . . 66
4.2 Maxwell counting . . . 66
4.3 Network model . . . 67
4.4 Maxwell counting in our networks . . . 68
4.5 Shear response . . . 68
4.6 Mode analysis . . . 72
4.7 Conclusions . . . 73

5 Frequency-dependent response of networks **75**
5.1 Introduction . . . 76
5.2 Network dynamics . . . 77
5.3 Dynamic moduli in shear . . . 79
5.4 Measurements of G' and G'' . . . 80
5.5 Dynamical suppression of non-affinity . . . 80
5.6 Classification of regimes . . . 82
5.7 Large shear amplitudes . . . 83
5.8 Relation to prior work . . . 85
5.9 Conclusions . . . 86

Bibliography **87**

Samenvatting **93**

Publications **99**

Curriculum vitae **101**

Dankwoord **103**

Chapter 1

Introduction

This chapter provides an introduction into the exciting field of the physics of biopolymer networks. These networks are ubiquitous in biomaterials, on the level of structures inside single cells as well as in extracellular structures. Scientists have only started to reveal the wide range of functions of these networks, among which are the stability, elasticity and force transduction of cells and extracellular structures. One specific area of interest in this field is the relation between forces and deformation of these networks. With the advance of experimental techniques, the level of detail of microscopic data is increasing rapidly. As a result, the models evolve from coarse-grained constitutive relations to descriptions that relate the microstructure of these networks to the observed dependencies of forces on deformations. We start this chapter with a description of biopolymers and biopolymer structures in cells and in extracellular materials, and give a short overview of experiments performed on biopolymer structures. We continue with introducing the measure for stiffness commonly used to describe the behavior of biopolymer structures under deformation. An important aspect of this behavior is the structural rearrangement during deformation, characterized by the non-affinity, and the single-polymer behavior. Next, some models that have been developed to describe the physics of biopolymer networks are introduced. The model which we present in chapter 2 and use in chapters 3 and 4 is an elaboration of these models, with a more detailed microscopic description. We end with providing background information on some simulation techniques; this will be helpful to understand the work described in the remainder of this thesis.

1.1 Polymer networks in biology

To combine strength with flexibility, nature makes use of biopolymer networks. We encounter these networks at different levels of organization, such as inside cells, in between cells, in multicellular structures and in tissues such as skin and blood vessels. What are biopolymers? What kind of structures do they form? And what is the functional role of these structures in biology? In this section we will address these questions by giving a short overview of intracellular and extracellular biopolymer networks and discussing some of the early experiments. But before we focus on the structures of biopolymers, we first discuss what biopolymers are made of.

1.1.1 Biopolymers

Biopolymers are supramolecular polymers, consisting of macromolecules. Three different types of macromolecules formed by the cell are polynucleotides, polysaccharides and polypeptides. DNA and RNA are *polynucleotides*, that both carry the genetic information. *Polysaccharides* are mostly used to store energy. In this thesis we focus on structures made from *polypeptides*. Polypeptides are also called proteins, and play an important role in many different functions of cells and tissue. For instance, they play a key role in the catalysis of chemical reactions, the transport of molecules, the communication between cells and the determination of the structure of cells and tissue. One specific way of organization of proteins is the formation of linear structures. In this thesis, we focus on these long arrays of proteins and call them *biopolymers*. Biopolymers are essentially long filaments, of which the monomers are proteins. These monomers are bound together by non-covalent interactions such as hydrogen bonds or van der Waals forces. These biopolymers are living polymers, which implies that they are dynamic objects out of equilibrium, that continuously change shape. Under the influence of specific proteins and nucleotides that carry energy, they grow, shrink, depolymerize and form higher-order structures such as networks and bundles. The time scales of these processes have a large spread, depending on polymer type, tissue/cell type and environment. For example, actin monomers in cells can polymerize into networks in a couple of seconds to minutes, when they are placed in appropriate conditions [1]. In steady state, the monomer addition rates for actin filaments in cells are estimated to be 3 to 60 s^{-1} [1–3].

1.1.2 Biopolymer structures in cells

All living organisms consist of cells. A commonly made division is that of *prokaryotic* cells, which are the cells of single-cell organisms like bacteria, and *eukaryotic* cells, of which plants, fungi, animals and humans are made. All eukaryotic cells possess some generic features. They have a plasma membrane which separates the inside from the outside of the cell and which permits small molecules to permeate through the cell boundary. The cells possess organelles, which are small compartments in cells which are separated from the rest of the cell by a thin membrane. The cell nucleus,

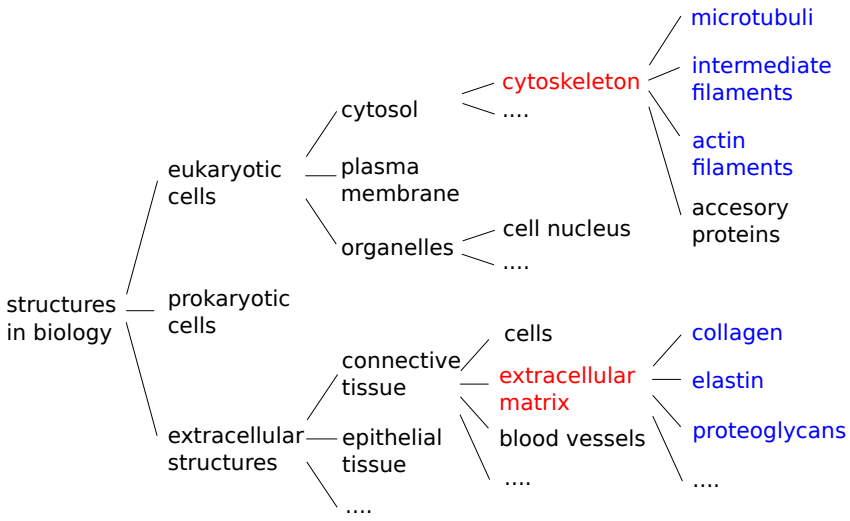


Figure 1.1: Schematic overview of building blocks of structures in biology. Biopolymers are colored blue, the biopolymer network structures are colored red.

containing the DNA, is one of the most well-known organelles. The interior of the cell that is not incorporated by organelles is the cytosol, an ionic liquid that contains a vast range of proteins. An important component of the cytosol is the cytoskeleton, a dynamical fibrous network consisting of different proteins. Figure 1.1 summarizes the information given in this and the following section.

The cytoskeleton has many functions. It makes cells physically robust, such that they can withstand forces. It supports the thin plasma membrane, which would be extremely floppy without the cytoskeleton. The cytoskeleton is important in the overall organization of the cells, such as the positioning of the cell nucleus and other organelles. The cytoskeleton can alter its shape, by which it allows the cells to change shape. Besides, it allows the cell to mechanically interact with the cell environment and move around.

The three main components of the cytoskeleton are microtubuli, intermediate filaments and actin filaments. All three of these are fibrous structures that are built by the linkage of small proteins into a larger structure. These fibers are highly dynamic structures that grow and shrink continuously. The *intermediate filaments* are mainly involved in giving mechanical strength to the cell. The *microtubuli* are important for intracellular transport, driven by motors walking along the fibers. By pushing against the plasma membrane, the network of microtubuli helps to position the cell nucleus and other structures. *Actin filaments* are important for the determination of the shape of the cell and are mostly found close to the plasma membrane. These filaments are necessary for whole cell locomotion, a process in which the cytoskeleton assembles

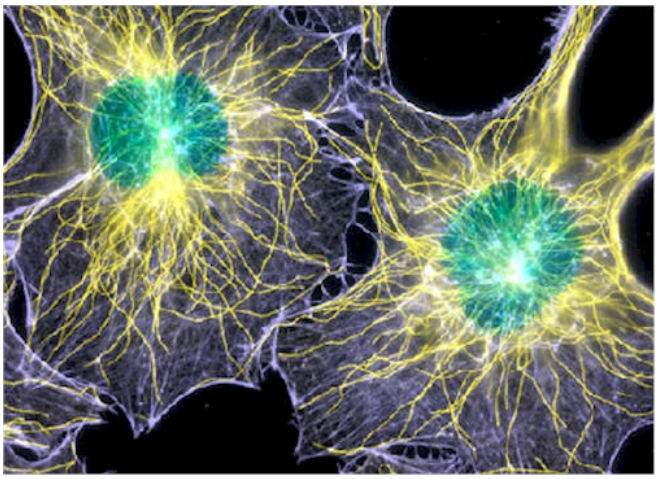


Figure 1.2: Cell in which the cytoskeleton is stained with yellow (microtubuli) and blue (microfilaments or actin filaments). The cell nucleus is stained azure. Picture taken from http://www.microscopyu.com/smallworld/gallery/index.html

on one end and disassembles on the other end, such that the cell as a whole moves. Figure 1.2 shows an image of a eukaryotic cell in which the microtubuli and actin filaments can be distinguished.

Besides these three main components of the cytoskeleton, many accessory proteins are known that fulfill various functions in these networks, such as linking different filaments together, cutting filaments, connecting filaments to the plasma membrane and transporting filaments. One class of accessory proteins are for instance the actin binding proteins, that connect different actin filaments. Depending on the precise morphology of these proteins, the resulting structures of filaments can be either bundled, web-like or branched-like [4, 5].

1.1.3 Extracellular structures

Eukaryotic organisms are more than just a clump of cells; they possess structures at scales much larger than that of single cells. An important and widespread example of such large-scale structures is the connective tissue. In this structure the relatively soft cells are embedded in an extracellular matrix (ECM), consisting of different types of biopolymers such as the stiff collagen, much softer elastin and proteoglycans. These biopolymers form a viscoelastic structure that can have a wide range of properties and that determines the stiffness of the connective tissue. Bone, retina and tendon are some examples of cells embedded in an ECM in which the resulting multicellular structure has varying optical, mechanical and elastic properties. In these structures,

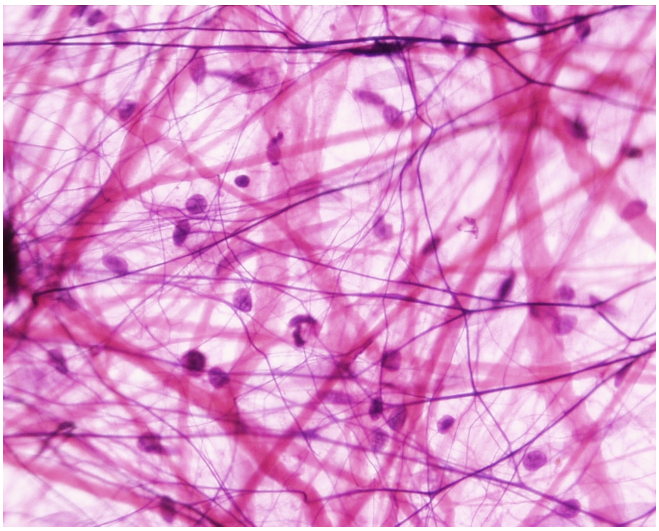


Figure 1.3: Areolar connective tissue consisting of loosely organized fibers, mostly collagen en elastin (light-colored large structures), blood vessels (dark-colored thin structures) and some cells (small dots). Figure taken from http://www.carlalbert.edu/dwann/

the cells are attached to the ECM and vice versa, such that the cells can pull on the matrix and on each other via the matrix. This interaction between the ECM and the individual cells is not only used as a way to transmit mechanical signals, but is also used by the cell to move in the ECM. The origin of many diseases lies in the organization of the ECM. One typical example is Marfan Syndrome, a genetic disorder in the connective tissue which, among other characteristics, makes the tissue softer for deformation. Figure 1.3 shows an image of connective tissue.

Another way of cellular organization can be found in epithelial tissue. Here, cells are closely bound together. Integrins bind the cytoskeletons of the adjacent cells in the tissue. The resulting stiffness of the tissue comes from the cytoskeletons of the individual cells and the stiffness of the connections between them.

Although the basic functions of these intra- and extracellular structures are known, many questions are still open. What is the interplay between the different constituents in these structures? How is the network structure related to the function of these networks? And how can these structures be controlled, adjusted and reformed? Experiments and modeling are necessary to answer these questions. In the following section we will give a short overview of early and more recent experimental techniques used in the study of biopolymer networks, and some of the findings.

1.1.4 Experiments on biopolymer networks

The field of biopolymer structures started with the study of *in vivo* biopolymer structures, such as red blood cells, tendons, skin, muscles and lung tissue [6]. The focus has been on studying the *mechanical* properties, inspired by the mechanical function these structures have in living tissues and cells. Small parts of tissue are taken from organs, and stretched, sheared and compressed to understand their response to deformation. These tissues show some generic behavior: a nonlinear stress-strain relationship, hysteresis under cyclic loading and stress relaxation at constant strain. To understand the effect of trauma of the dissection, whole-organ experiments are performed, for example on lungs or arteries. The precise response under deformation largely depends on the type of tissue. Tendons are rather stiff to deformation and can withstand stretch up to only 5%, while arteries and veins can be stretched by about 60%. Most of the tissue-specific behavior can be related to the function of that specific tissue. One example is the uterine cervix, connected to the womb. Early experiments on rat tissue showed softening during pregnancy, induced by changes in ground substance and in water composition of the uterine cervix [6].

Studies of red blood cells are another example of experiments performed in the 1960s and 1970s. With optical microscopic imaging, the shape and size of blood cells in an isotonic solution can be observed, as well as the circulation of blood cells in capillary blood vessels. Some basic information on the elastic properties of the cell membrane is deduced from the amount and precise geometry of the osmotic cell swelling. Among other experimental techniques used to characterize the red blood cells is microscopic imaging of the recovery of the shape of the cells after micropipette aspiration. These experiments show that cells are viscoelastic materials, which means that the deformation of these materials has both an elastic and a plastic component.

These experiments laid the foundation of the contemporary experiments on biopolymer structures. Recent improvements and refinements of experimental techniques have increased the accuracy, the level of control and the level of detailed information obtained by experiments. Some examples of these new experimental techniques are bulk rheology, traction force microscopy, microrheology and atomic force microscopy. In *bulk rheology* single cells or small pieces of tissue are sheared and the response under deformation can be accurately measured, see figure 1.4a. In *traction force microscopy* tracer beads are placed in a flexible substrate interacting with cells, see figure 1.4b. The displacements of the beads are imaged and are related to the forces exerted by the cells. Both microrheology and atomic force microscopy are used to measure the local stiffness. *Microrheology* (figure 1.4c) allows for the determination of the local stiffness throughout a sample: micrometer-size beads are placed inside a sample and their displacements in time or under deformation are monitored. *Atomic force microscopy* allows for a more direct way of measuring the local relation between stress and deformation, but can only be applied at the surface of samples, as shown in figure 1.4d. In this type of experiments, small stresses are applied to tissues and cells and the displacement of the microscope's cantilever is related to the local stiffness of the cells or tissue. Another important development is the increas-

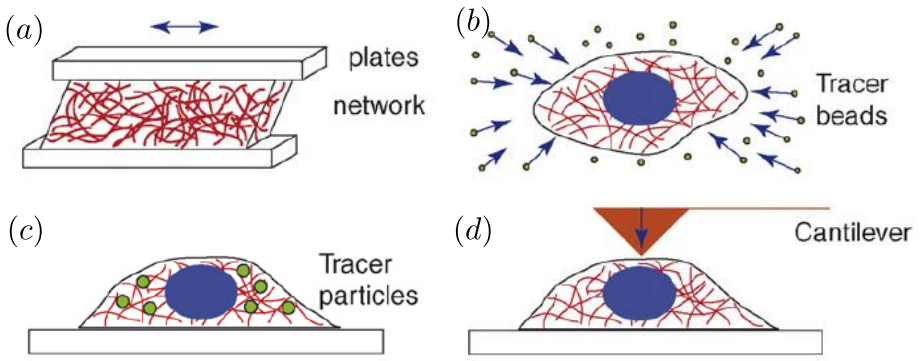


Figure 1.4: Illustration of four experimental techniques commonly used to determine the viscoelasticity of biopolymer networks. (a) Bulk rheology: a small sample is sheared and the response is measured. (b) Traction force microscopy: the displacements of small beads placed in a flexible substrate can be related to the forces exerted by the cell placed on top of the flexible substrate. (c) Microrheology: small beads are placed in a cell/gel/substrate and allow for determining the local stiffness and network structure. (d) Atom force microscopy: a cantilever exerts local strains and measures local stresses and vice versa. Illustrations taken from [7].

ing knowledge of the biochemical properties of the different constituents of biopolymer networks in cells and tissues, that allows for protein-specific staining and deletion. New imaging techniques increase the resolution of the information. Contrary to early experiments, these experimental developments make it possible to quantitatively unravel the intriguing relationships between the network constituents, the network structure and topology and the network response under deformation.

The insights gained from these new instruments have been enhanced by studies of *in vitro* systems. As stated before, cells contain different types of biopolymers, integrated into network-like structures. More than a hundred different types of proteins play a role in this structural organization by binding, bundling and cutting these polymers. Because of the enormous complexity of these structures inside cells, it is hard to link experimental observations to cellular structures and functions. This same problem holds for extracellular tissue, where many different constituents and patterns of organization contribute to the overall stiffness of a living material. A more controlled way to gain insight in biopolymer networks is by *in vitro* experiments. Here, purified biopolymers are treated and mixed with proteins such that under the right conditions, such as the appropriate concentrations, temperature and pH-value, the biopolymers will form bonds with each other and subsequently form connected networks. Since the polymer concentration, crosslinking density, types of bonds and average lengths of the polymers can be controlled by the experimentalist, these type of

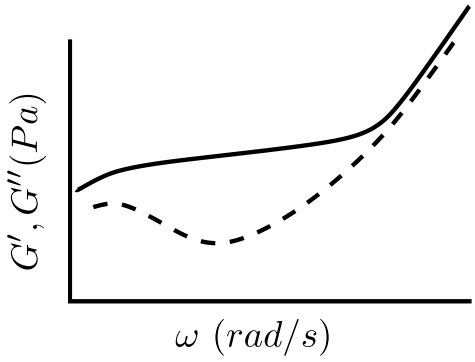


Figure 1.5: Schematic illustration of G' and G'' as a function of frequency ω.

experiments allow for a bottom-up exploration of a large parameter range. Actin filamentous networks are extremely well-studied examples of such *in vitro* biopolymer networks.

These new experimental methods call for theoretical modeling beyond the level of simple constitutive equations. Although the insights from the coarse grained modeling have been many and insightfull, the explanatory power of this type of modeling is limited. In order to explain the experimental findings and to describe the mechanical behavior of these networks, the single-segment properties of the network constituents and the network structure have to be taken into account, as we will do in this thesis. In the remainder of this introduction we discuss models of single polymers. We also introduce the concept of non-affinity to describe how the topology and single-filament properties decide the network response under deformation. But first we give some background information on the elastic and viscous modulus in materials, since these are the most commonly used quantitative measures of viscoelasticity in biopolymer networks.

1.2 Elastic and viscous modulus

Materials may deform elastically or plastically. The elastic response is reversible: the material deforms under stress but will return back to its original configuration once the stress is released. The viscous response is irreversible: the deformation due to the applied stress remains when the stresses are released. Most biopolymer networks are visco-elastic materials, and show a combination of both a viscous and an elastic response under deformation. For isotropic materials, the response under small deformation is characterized by two quantities: the material stiffness under compression, generally known as the bulk modulus B and the stiffness under shear, known as the shear modulus G. These two moduli can be decomposed into an elastic and a viscous

component.

The visco-elastic properties of biopolymer networks are often measured with a rotating disc rheometer. In this type of measurement, either a sinusoidal shear strain is applied while measuring the shear stress, or a sinusoidal shear stress is applied while measuring the shear strain. Since these kinds of deformation are volume-conserving, the incompressibility of the liquid does not pose problems. In this thesis we mainly consider the network response under shear deformation, and therefore calculate the shear modulus while leaving the bulk modulus out of our discussion. Here we present a derivation of the relation between the stress, strain and the viscous and elastic shear moduli, and discuss some experimental results.

If a sinusoidal strain with frequency ω is applied, the shear can be expressed as

$$\gamma^\star(t) = \gamma_0 \exp(i\omega t). \tag{1.1}$$

In linear response theory, the (complex) stress $\sigma^\star(t)$ can now be related to the shear $\gamma^\star(t)$ by the complex shear modulus $G^\star(\omega)$,

$$\sigma^\star(t) = G^\star(\omega)\gamma^\star(t). \tag{1.2}$$

The resulting stress can be expressed as

$$\sigma^\star(t) = \sigma_0 \exp(i(\omega t + \delta)), \tag{1.3}$$

and the complex shear modulus is then given by

$$G^\star(\omega) = \frac{\sigma^\star(t)}{\gamma^\star(t)} = \frac{\sigma_0}{\gamma_0} e^{i\delta} = G' + iG''. \tag{1.4}$$

Here, γ_0 is the amplitude of the shear strain, σ_0 is the amplitude of the shear stress and δ is the phase shift that measures how much energy is stored and how much is dissipated. G' is the elastic modulus of the material, also known as the storage modulus; G'' is the viscous modulus, also known as the loss modulus. We can express G' and G'' as a function of the strain and stress amplitudes and the phase shift,

$$\begin{aligned} G' &= \frac{\sigma_0}{\gamma_0}\cos(\delta) \\ G'' &= \frac{\sigma_0}{\gamma_0}\sin(\delta). \end{aligned} \tag{1.5}$$

Recent experiments show that whether the cells are malleable or rigid under deformation, depends on the rate of deformation [8]. Figure 1.5 shows a schematic of G' and G'' as a function of ω. This figure is based on experimental measurements of the stiffness of crosslinked f-actin networks at low and high frequencies, such as those reported in references [9, 10]. The frequency dependence mirrors the relaxation times of the modes in the network: at high frequencies, only the fastest modes in the networks can relax, while with decreasing frequencies more and more network

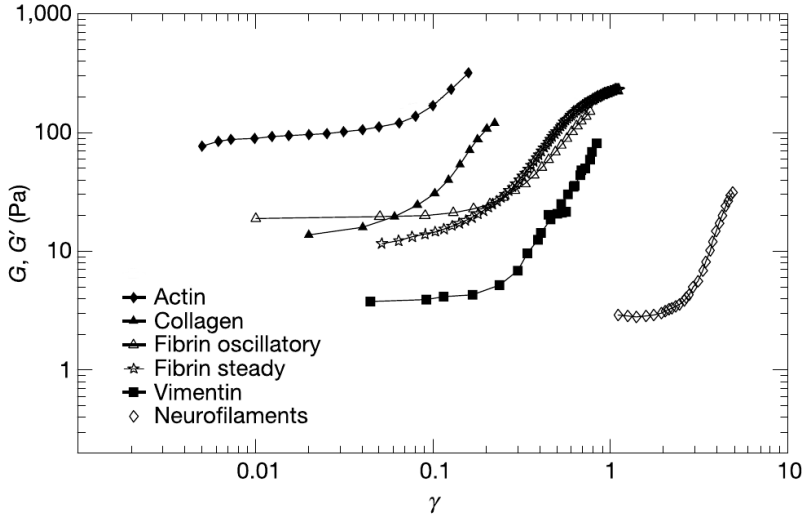


Figure 1.6: Elastic modulus of several types of biopolymer networks as a function of shear amplitude γ. Figure taken from [15].

modes can relax during deformation. At the smallest frequencies, G' and G'' are of the same order and the networks are highly viscous materials. This is attributed to crosslinker binding dynamics that remodel the networks [11, 12]. At the highest frequencies, both G' and G'' steeply increase with increasing frequency, approximately in a power-law fashion. Generally, this is attributed to the single-segment relaxation of semiflexible polymers that gives rise to a characteristic $\omega^{3/4}$ scaling of the stiffness with frequency [9, 13, 14]. In chapter 5 we will offer a more elaborate explanation for the increase of G' and G'' at higher frequencies. As is the case with entangled solutions of biopolymers, in crosslinked networks we can distinguish an intermediate regime where G' is almost constant. This regime is generally called the rubber regime. The stiffness depends on filament concentration, filament stiffness and crosslinker concentrations. Typically, G' in the intermediate regime lies between one and a few hundred Pa. For crosslinked networks in this regime, G' is typically ten times larger than G'', and the elastic response is thus dominant in this regime. For small deformations, the stress scales linearly with the deformation, thus in this intermediate regime we can simply describe the elastic response by a single constant G', that does not depend on γ anymore

$$\sigma = G'\gamma. \tag{1.6}$$

Most of the modeling is done in the regime where $G' \gg G''$.

Experiments show that the cellular response to *large* deformations is highly nonlinear, such that the stiffness of the cells depends to a large extent on the amplitude

of the applied stress [16]. Figure 1.6 shows the strain response of different types of densely crosslinked *in vitro* biopolymer networks. As shown, densely crosslinked networks show an increased stiffness with increasing strain. This property of *strain stiffening* sets them apart from many other materials, which often show strain softening: the restoring force increases less than linearly with applied strain. For living tissues, this feature is extremely important. It implies that tissues are soft under small deformations but rigid under large stresses, thus preventing large deformations that could threaten tissue integrity [15].

At these large strains, the network response ceases to be linear and higher-order terms in the network response should be taken into account. The stress response on a sinusoidal strain with frequency ω can then be represented as a series containing multiple harmonics [17]

$$\sigma^{\star}(t) = \sum_{n=0} \sigma_n \exp(i((n+1)\omega t + \delta_n)). \tag{1.7}$$

Obviously, calculating the elastic modulus from the measured stress or strain response according to equation (1.5) is no longer justified. To overcome this problem, the network response can be more precisely quantified by the differential elastic modulus, defined as

$$K = \frac{\partial \sigma}{\partial \gamma}. \tag{1.8}$$

This quantity can be experimentally obtained by applying a fixed stress, after which a small oscillatory stress is superposed [18]. In the regime where $\sigma \propto \gamma$, G' and K are identical, but for larger strains they deviate from each other.

1.3 Non-affinity

In experiments, if networks are deformed, one or more degrees of freedom of the network are constrained: the network is forced to accommodate a specific global shear. The number of degrees of freedom of a network is however much larger than the few imposed constraints. The microscopic displacements will then be decided by the condition of minimal free energy, constrained by the imposed global deformation. Figure 1.7 shows a schematic example, in which two connected springs with a finite rest length are placed in a two-dimensional box at zero temperature. Before shear is applied, the two springs are at their equilibrium length and the energy in the box is zero. Now a shear is applied along the boundaries of the box. Figures 1.7b and 1.7c show two possible modes of deformation of the springs. Figure 1.7b shows the deformation of the system in the case the system deforms affinely, i.e. all microscopic degrees of freedom follow the global deformation. In this case, the strings are stretched and compressed and the energy of the system is non-zero. Figure 1.7c shows the actual mode of deformation. Here, the system deforms non-affinely, such that the springs are neither elongated nor compressed; the energy remains zero at finite strain. The arrow indicates the difference between the affine and non-affine

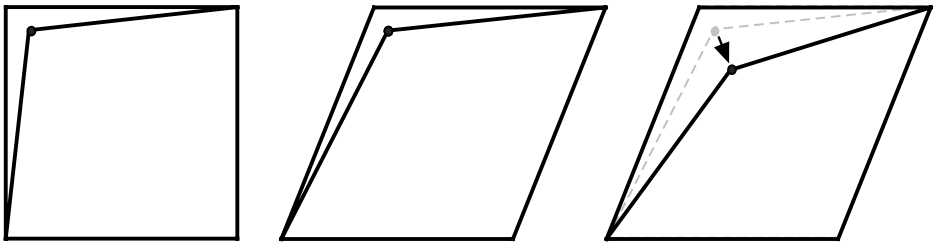


Figure 1.7: System consisting of two connected springs shown at rest (left panel), under affine shear deformation (middle panel) and the actual shear deformation with non-affine relaxation (right panel).

position of the point of contact of the two springs. The length of this arrow is a measure for the non-affinity of the network. Clearly, as long as this is possible, the system will deform non-affinely such that the energy remains zero.

A slightly more involved example of a system that can deform non-affinely is given in figure 1.8. Here, one long rod is connected to the left and right side of the box and two small rods are connecting the corners of the box to this long rod. If the stretching stiffness of the rods is small with respect to the bending stiffness, the system will deform such that the long rod does not bend, giving rise to an affine deformation, as shown in figure 1.8b. In the opposite case in which the bending stiffness is much smaller than the stretching stiffness, the long rod will bend in such a way that stretching is avoided, leading to a non-affine deformation, see figure 1.8c. These two examples show the intriguing interplay between the network structure and the filament properties: together, they determine the network response under deformation in a highly nontrivial manner.

These two examples show the importance of non-affinity in networks. One should know the non-affine motion of single filaments during deformation to understand and model the actual behavior of these filaments. Non-affine reorientations can significantly alter the network stiffness under deformation. Also, the amount by which the filaments deform through bending or stretching is strongly related to the amount of non-affine behavior under deformation.

Only in the last couple of years, experimentalist have started to develop methods to measure the non-affinity of the deformation of biopolymer networks [19,20]. They do so by tracking embedded probe particles during deformation. For this technique, small fluorescent beads with a size of $\approx 0.5-1$ μm are embedded in networks. A microscope is used to visualize the position of these particles in the networks. For the displacement of the beads to be larger than the resolution of the system, the applied shears must generally be quite large ($\gamma \approx 2-20\%$).

Different quantities have been identified to relate the displacements of the embedded beads to a non-affinity measure. Since non-affinity can be regarded as additional displacement on top of the affine displacement, perhaps one of the most

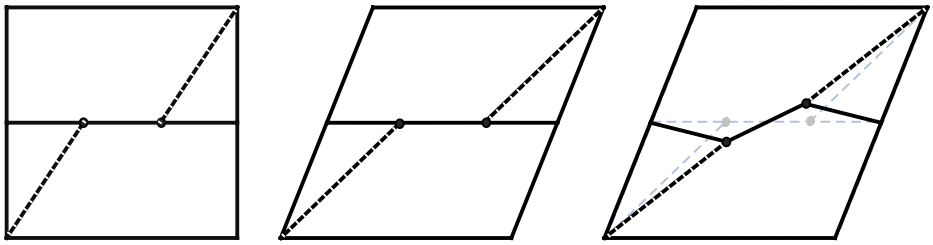


Figure 1.8: System consisting of one long rod connected to the right and left walls of the box. Two shorter rods connect a corner of the box to this long rod. The system is shown at rest (left panel), under shear deformation if the stretching stiffness of the rods is much smaller than the bending stiffness of the rods (middle panel) and under shear deformation if the bending stiffness is much smaller than the stretching stiffness (right panel).

intuitive measures is given by

$$A = \frac{1}{N} \sum_i \frac{| \vec{x}_i - \vec{x}_{i,\text{aff}} |^2}{\gamma^2}, \tag{1.9}$$

where N is the number of particles, $\vec{x}_i$ is the actual position of particle i, $\vec{x}_{i,\text{aff}}$ is the position of particle i if the deformation would have been affine and γ is the applied strain. One of the other measures proposed in literature considers the angles between the displacement vectors of neighboring nodes in the system [21, 22].

The relation between the network properties and the network non-affinity is poorly understood, as is the impact of the non-affinity on the network stiffness [23–26]. In this thesis we show that generally, the non-affinity of a network deformation depends on three parameters, namely the applied deformation, the filament stiffness and the network structure. In chapter 2, the key quantity of the applied deformation that we study is the amount of shear. In chapter 5, we also study the effect of the frequency of the applied shear. The effect of frequency enters because the filaments in a network are embedded in a viscous medium. If a network deforms fast, the filaments might not have enough time to fully relax. First, however, we turn towards the physics of single filaments.

1.4 Models of single filaments

As stated above, one key ingredient in the behavior of networks of filaments is the behavior of the individual filaments. Biopolymers consist of many monomers that are bound together and are surrounded by a liquid. Most biopolymers are soft materials at room temperature, with a typical bending energy scale of $k_B T$. The polymers will therefore show thermal undulations, due to the random motion of particles in the

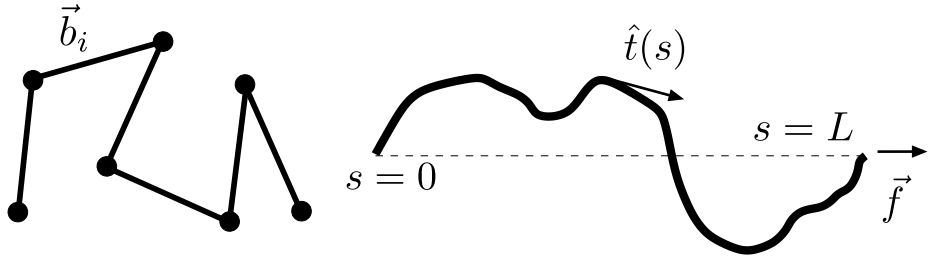


Figure 1.9: Graphical illustration of the freely jointed chain model (left) and the worm-like chain model (right).

liquid in which the polymers are immersed. Hence the average properties of biopolymers can be calculated with methods from statistical physics, such as the average length, the force-extension and the radial distribution. In this section, we start with a description of the *freely jointed chain*, the simplest polymer model that nicely describes the effect of entropy on the properties on the polymer. Next, we turn to the *semiflexible worm-like chain*, a model that describes the physics of a broad range of biopolymers.

1.4.1 Freely jointed chain

One of the simplest polymer models is that of the freely jointed chain. This is a chain consisting of N rigid links, all having equal length b, which are connected in a head-to-tail fashion. The vectors $\vec{b}_1$, $\vec{b}_2$,..., $\vec{b}_N$ are the end-to-end vectors of these links, see figure 1.9. In this model the rigid links are often called the monomers of the polymer. The contour length L is the total length along the filament, here it is equal to Nb. All links can rotate freely with respect to each other, without energy cost, in the situation of no applied force. The system is described by the microcanonical ensemble and all chain configurations are equally likely. If excluded-volume effects of the chain are ignored, the chain displays the characteristics of a random walk and the average end-to-end length is given by $r = b\sqrt{N}$.

If an external force $\vec{f}$ is applied on the ends of the chain, the links prefer to be aligned in the direction parallel to this force. Under ideal behavior, if $T = 0$ or $f \to \infty$, the chain takes a straight configuration, in which $r = L$. This single straight configuration is however vastly outnumbered by the many bent states. Therefore, at non-zero temperature and for finite forces, an entropic force prevents the polymer to be perfectly straight. In the situation of $f = 0$ or $T \to \infty$, the chain displays random walk characteristics again and $r = b\sqrt{N}$.

This phenomenological result can also be deduced from the partition function. The system can be described by the canonical ensemble and the energy of the chain

is given by

$$\frac{E}{k_B T} = -\sum_i \frac{\vec{f}\cdot\vec{b}_i}{k_B T}, \tag{1.10}$$

which is minimal when all links are aligned. The partition function can be calculated by integrating the Boltzmann weight of the energy of a certain configuration, $e^{-\beta E}$, over the space of all possible configurations,

$$Z = \int e^{\beta \sum_i \vec{f}\cdot\vec{b}_i} \mathrm{d}^3 r. \tag{1.11}$$

Here, $\beta = 1/(k_B T)$. The configurational space of each monomer can be described by a sphere with surface area $\sin\theta d\theta d\phi$, which yields the partition function of the whole chain as

$$Z = \left(4\pi k_B T \frac{\sinh(\frac{fb}{k_B T})}{fb}\right)^N. \tag{1.12}$$

Taking the derivative of the logarithm of the partition function with respect to inverse temperature β gives the average free energy of the polymer,

$$\langle F\rangle = \frac{\partial \log Z}{\partial \beta} = -N[k_B T - fb\coth(\frac{fb}{k_B T})]. \tag{1.13}$$

Similarly, the average end-to-end length $\langle r\rangle$ can be related to the derivative of the logarithm of the partition function with respect to f as

$$\frac{\langle r\rangle}{L} = -\frac{1}{\beta}\frac{\partial \log Z}{\partial f} = \frac{k_B T}{fb} - \coth(\frac{fb}{k_B T}), \tag{1.14}$$

a result that can also be obtained from the relation between the average free energy and the average end-to-end length

$$\langle r\rangle = -\frac{\langle E\rangle}{f}. \tag{1.15}$$

1.4.2 Semiflexible worm-like chain

Early experiments on f-actin networks show that the network stiffness is much larger than one would expect based upon the freely jointed chain model [16, 27]. Images of biopolymers show that most biopolymers are rather straight [16, 28]. This indicates that single monomers cannot rotate freely with respect to each other, but that they experience a bending stiffness preventing large bends between consecutive monomers. Because consecutive monomers have nearly the same orientation, we can use a continuum description of the polymer. One model that takes these considerations into account is the worm-like chain model, in which the Hamiltonian of a single polymer under an external force can be written as [29, 30]

$$H_{\mathrm{wlc}} = \int_0^L \left(\frac{\kappa}{2}\left|\frac{d\hat{t}(s)}{ds}\right|^2 - f\hat{t}(s)\right)\mathrm{d}s. \tag{1.16}$$

Here, s is the arc length coordinate running along the filament, $\hat{t}(s)$ is the (unit) tangent vector along the filament, f is the applied force, directed along the end-to-end vector of the polymer, see figure 1.9, and κ is the bending stiffness of the polymer. Implicit in this definition is that the contour length L, which is curvilinear length of the filament, is constant; the filament is locally inextensible.

The three parameters which determine whether or not the filament is highly curved or nearly straight, are the bending stiffness, the temperature and the contour length. A large bending stiffness suppresses bending. The temperature decides the amount of thermal fluctuations in the filament: a high temperature induces large thermal fluctuations while a low temperature gives rise to a nearly straight configuration. Combining these two, $\frac{\kappa}{k_B T}$ gives a measure for the length over which a polymer appears straight in the presence of thermal undulations. This length is generally called the persistence length ℓ_p. The third parameter that decides whether a filament is straight or curved is the contour length L.

In the space spanned by the parameters L and ℓ_p, we can distinguish three regimes. In the case of $L \gg \ell_\mathrm{p}$ the polymer is highly curved. If a force is applied, the extension of the chain is dominated by the stretching out of thermal fluctuations. The force extension is thus entropic in origin, as is the case with the freely jointed chain. If $L \ll \ell_\mathrm{p}$, the filament is almost straight. Since there are hardly any thermal undulations which can be pulled out, the local inextensibility of the chain becomes a global inextensibility. If L is of the same order as ℓ_p, the polymer will be more or less straight with some thermal undulations. Polymers in this regime are the so-called semiflexible worm-like chains. Many biopolymers at body temperature have bending stiffnesses and filament lengths which causes them to fall in this class of polymers.

Deriving an analytic expression for the force-extension relation based upon the energy of worm-like chains as given in equation (1.16) is extremely difficult. For the class of *semiflexible* worm-like chains we can formulate one further assumption that simplifies equation (1.16) such that it becomes solvable. The tangent vector $\hat{t}(s)$ can be decomposed into the component $\hat{t}_{||}(s)$ parallel to the force and the end-to-end vector of the polymer and the component $\hat{t}_\perp(s)$, perpendicular to the direction of the force. For semiflexible filaments, the filament's backbone undulations are small, such that $\hat{t}_{||}(s)$ will be close to unity along the backbone and $\hat{t}_\perp(s)$ will be small. Within this approximation, the Hamiltonian for the semiflexible worm-like chain becomes, to leading order in $\hat{t}_\perp(s)$ [15,27],

$$H_{\text{sf wlc}} = \int_0^L \left(\frac{\kappa}{2} \left| \frac{d\hat{t}_\perp(s)}{ds} \right|^2 - f\left(1 - \frac{1}{2}\left|\hat{t}_\perp(s)\right|^2\right)\right) \mathrm{d}s. \tag{1.17}$$

We can derive an expression for the force-extension relation by Fourier analysis and the equipartition theorem [15,31]. If we define the end-to-end vector of the polymer to be parallel to the z-axis, then $\hat{t}_\perp(s) = \{t_x(s), t_y(s)\}$. This can be written as a single complex quantity, $t(s) = t_x(s) + i\, t_y(s)$. Since both components are zero at $s = 0$

and $s = L$, we can sine transform this into

$$t(s) = \sum_{q=1}^{\infty} t_q \sin(qs), \tag{1.18}$$

where $q = \frac{n\pi}{L}$ and $n = 1, 2, 3, \ldots$. The energy can now be written as

$$H_{\text{sfwlc}} = \frac{L}{4} \sum_{q=1}^{\infty} (\kappa q^2 + f) |t_q|^2. \tag{1.19}$$

Taking into account that all quadratic terms in the energy contribute $k_B T/2$ to the average energy, and that $\vec{t}_q$ is a two-dimensional vector, we sum all modes such that

$$\langle |\hat{t}_\perp|^2 \rangle = \frac{2k_B T}{L} \sum_{q=1}^{\infty} \frac{1}{\kappa q^2 + f} = \left(\frac{k_B T}{fL}\right) \left[\sqrt{fL^2/\kappa} \coth(\sqrt{fL^2/\kappa}) - 1 \right]. \tag{1.20}$$

The length $\langle r(f) \rangle$ of the end-to-end vector as a function of the applied force of semi-flexible filaments can now be expresses as

$$\langle r(f) \rangle = L\left(1 - \frac{1}{2}\langle |\hat{t}_\perp|^2 \rangle\right) = L - \left(\frac{k_B T}{2f}\right) \left[\sqrt{fL^2/\kappa} \coth(\sqrt{fL^2/\kappa}) - 1 \right]. \tag{1.21}$$

This description of the single-filament properties of biopolymers can be used to describe the network properties. In the following section we will discuss network models that have been proposed to describe the network properties of biopolymer networks.

1.5 Models of biopolymer networks

Two main approaches can be distinguished, which model the behavior of biopolymer networks under deformation. The first approach explains the behavior of biopolymer networks under deformation from the force-extension behavior of single filaments alone. In this approach, the network response is entropic in origin, in the sense that the network stiffness under shear originates from the decrease in the number of possible fluctuations of the filaments in the network. The second approach relates the observed stress-strain relations of biopolymer networks to the network structure of these networks, neglecting the entropic behavior of the individual filaments. In these models the network elasticity is enthalpic in origin, since the stiffness is due to bending and stretching of rods. In the following sections both approaches will be discussed.

1.5.1 Single-filament based models

Many biopolymers can be described by semiflexible worm-like chains. For networks in which the persistence length ℓ_p is of the same order of magnitude as the average

distance between crosslinks ℓ_c, equation (1.17) is used to calculate the network response of biopolymer networks. In these calculations the filaments are assumed to be divided into segments by crosslinks between the filaments. Each of these segments behaves according to equation (1.17). The filaments are assumed to be isotropically distributed in the networks. It is difficult to describe the actual displacement field of all segments in the network. To overcome this problem, the assumption is made that all segments follow the global deformation in the networks; i.e. all segments deform *affinely*. This assumption is also made in the modelling of the deformation of flexible networks.

The combination of the assumption of an affine network deformation and the single-segment behavior as described by equation (1.17) allows for the calculation of the elastic modulus, the large strain behavior and the frequency dependence of the network response. The most well-know result from this approach relates the small strain network modulus to the persistence length, the average segment length ℓ_c and the average distance between filaments ξ, which is directly related to the network density and the crosslinker density [27]. The applied force f on a segment is equal to the tension τ in a segment. To linear order in tension τ, equation (1.21) can be approximated by

$$\frac{\tau}{k_B T} \sim \frac{\ell_p^2}{\ell_c^4} \delta \ell_c, \tag{1.22}$$

where $\delta \ell_c$ is the extension of a segment with respect to its equilibrium length. The relative extension of a segment is proportional to the applied shear and the length of the segment,

$$\delta \ell_c \sim \gamma \ell_c. \tag{1.23}$$

Since we consider the shear-stress response on a shear deformation of a whole network, we multiply the tension in each segment by the number of segments per unit area along the plane parallel to the shear, which is $1/\xi^2$. Together, this gives us

$$\frac{G_0}{k_B T} \sim \frac{\ell_p^2}{\xi^2 \ell_c^3}. \tag{1.24}$$

Based upon the large-strain asymptote of the single-segment force-extension curve, the differential modulus is predicted to scale as $K \sim \sigma^{3/2}$. This agrees well with the large-strain scaling found in experiments [18]. Also the strain stiffening and the high-frequency response of the networks predicted from this affine, filamentous theory agree well with experiments [9, 13, 15].

Although this affine model has a broad explanatory power, there does not seem to be any reason why the networks would deform affinely. Moreover, the first couple of experimental results on non-affinity show a significant amount of non-affine reorientations during deformation [19, 20]. There are forces on the microscopic degrees of freedom which are not constrained by the global shear deformation. Reorientations correspond to motion in the direction of these forces, and therefore cause the free energy to be lower. In turn, the resulting modulus will also be lower. In the following

we will discuss models that do allow for non-affine reorientations during deformation. However, these models do not make use of the typical single-filament behavior discussed in the former section.

1.5.2 Network based models in two dimensions

Simulations of rod-like networks have shown to be a fruitful approach to understand the mechanical properties of biopolymer networks. The most widely used simulation tool is the so-called Mikado network, consisting of rigid rods in two dimensions. Mikado networks are generated by placing straight rods in a (periodic) two-dimensional box. The orientation and position of these rods is random. Once two rods cross each other, a crosslink is generated, that connects the two rods at the place where they cross; we will call the piece of rod between two adjacent crosslinks a *segment*. The deposition of rods stops when the desired density of rods is reached. In this method, the densities of crosslinks and rods and the average segment length are directly related: one of these cannot be regulated independent from the others.

The elastic properties of these rods are defined by a bending stiffness κ and a stretching stiffness μ. The Hamiltonian of the semiflexible worm-like chain is discretized [32]. The stretching energy of a specific network configuration is given by

$$H_{\text{stretch}} = \sum \frac{\mu}{2} \left(\frac{\partial \ell}{\ell_0} \right)^2 \ell_0, \tag{1.25}$$

where the summation runs over all segments, ℓ_0 is the equilibrium segment length and $\partial \ell$ is the change in segment length. The bending energy of a network configuration is given by

$$H_{\text{bend}} = \sum \frac{\kappa}{2} \left(\frac{\partial \theta}{\ell'} \right)^2 \ell', \tag{1.26}$$

where the summuation runs over all points that connect two adjacent segments along a rod. $\partial \theta$ is the angle between these two adjacent segments and ℓ' is the mean end-to-end distance between these two adjacent segments.

At low densities of rods, the rods do not form a network with rigidity percolation; the network does not have any resistance to small deformations. With increasing density, a network is formed that is rigid with respect to deformation. Subsequently, these rigid networks are deformed by shear. After each small shear increment, the energy of the network is minimized. The elastic modulus is then obtained from the behavior of the energy as a function of shear. The amount of non-affine deformation can be calculated from the displacement field of the crosslinks.

The network response can be classified as a function of the network parameters. The two parameters that determine the network behavior are the ratio of bending and stretching stiffness μ/κ and the ratio of the rod length and the average distance between crosslinks L/ℓ_c. The latter can also been seen as a measure for the number of crosslinks per rod or the density of the network. These two parameters determine whether the network response is in the bending-dominated regime, or in the

stretching-dominated one. When bending is soft with respect to stretching, the network deforms non-affinely. This is the case when L/ℓ_c is low and when μ/κ is high. In the other regime, stretching dominates and the networks deform more affinely. This regime is realized when L/ℓ_c is large or μ/κ is low [32, 33]. A non-affine deformation implies a large amount of bending in the network, while an affine deformation is almost purely stretching. These two different regimes are illustrated in figure 1.10, which shows a typical example of a low-density and a high-density network. The colors indicate the energies in these networks: clearly, the low-density network is dominated by bending while the high-density network is dominated by stretching.

These results have implications for the applicability of single-filament based models. In the regime where the network response is dominated by affine stretching of the rods, the network response is well described by an affine model of semiflexible filaments. However, a description based on affine deformation does not capture the physics in the regime where the network response is bending dominated. Rough estimates tell that most biopolymer networks are somewhere inbetween the bending and stretching dominated regimes [32, 33].

Another important characteristic of these networks is found by Onck *et al.* [34]. Starting with networks that are bending-dominated at small strain, they perform large-strain deformations. They observe a transition from a bending-dominated response at small strains to a stretching-dominated response at large strains. The non-affinity decreases with increasing strain, as expected from a transition from bending to stretching. These results are confirmed by three-dimensional simulations of biopolymer networks, that again show a transition from a bending-dominated response at small strains to a stretching-dominated response at large strains [35]. This transition from bending to stretching provides an alternative explanation for the observed strain-stiffening found in experiments on biopolymer networks. Figure 1.11 shows a typical example of a network that deforms by bending at small strains and stretching at large strains. This work also reveals the importance of the network geometry for the stiffness of these biopolymer networks. In this thesis we will further elaborate on this topic.

A more refined description of two-dimensional networks is introduced by Heussinger *et al.* [23]. In addition to the enthalpic stretching μ, an extra stretching term that accounts for the entropic origin of the single-segment elasticity is included in the Hamiltonian of the system. In systems where this entropic stretching term dominates, the networks appear to be highly sensitive to polydispersity and structural randomness, effects that are absent in athermal models. Based upon results obtained by numerical simulations, they describe the macroscopic elastic modulus in the non-affine regime by relating the low-energy excitations of the network to the non-affinity in the network [24, 36], the so-called 'floppy mode model'. To the best of our knowledge, this is the only work which finds an analytic relation between the non-affine displacement field and the elastic modulus.

In the models developed thus far, either the nonlinearity of the force extension of the single filaments is combined with a linear (affine) displacement field, or the nonlinearity of the displacement field is combined with a linear filament response

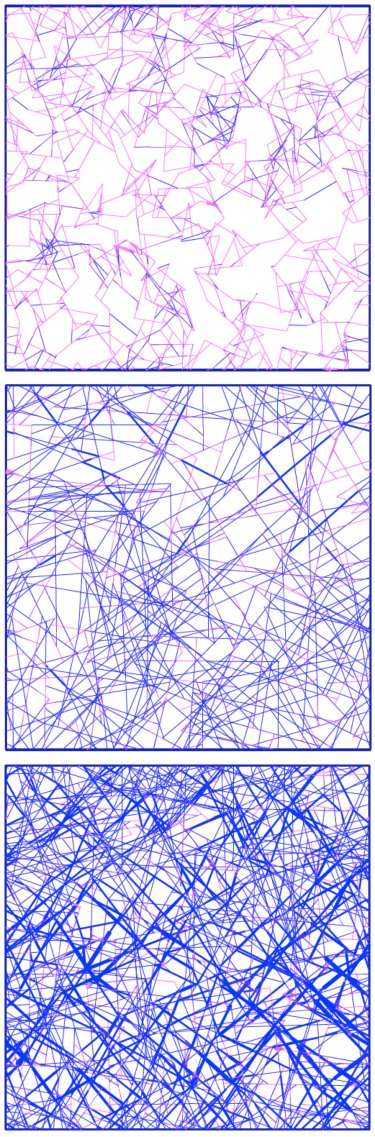


Figure 1.10: Examples of low, medium and high densities two-dimensional networks. Purple segments indicate that the majority of the deformation energy of that segment is stored in bending, in blue segments the deformation energy in that segment is mostly stored in stretching of the segment. Taken from [32].

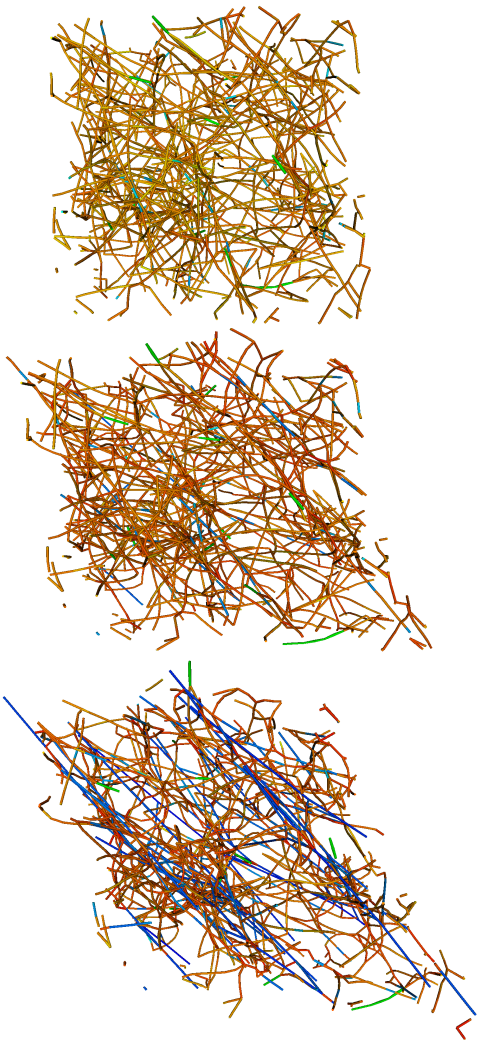


Figure 1.11: A typical simulated network in three dimensions under shear at different strain levels: $\gamma = 0.1$ (upper figure), $\gamma = 0.3$ (middle figure) and $\gamma = 0.5$ (lower figure). The color of each element corresponds to the value of the normalized energy difference $(H_{\text{stretch}} - H_{\text{bend}})/\overline{H}$ (< 0 red; ≈ 0 green; > 0 blue) where H_{stretch} and H_{bend} are the axial stretching energy and bending energy of an element, respectively, and $\overline{H}$ is the total energy of the network at each strain level. Taken from [35].

under deformation. Because of this, it is hard to decide the relative importance of the single filaments and the network structure. In this thesis we will combine both the nonlinearity of the force extension of single filaments with the nonlinearity of the displacement field. This gives us an powerful tool to describe the effect of both the network properties and the single-filament properties on the network response.

In the final section of this introduction we will give some background information about some computational methods used in this thesis.

1.6 Methods used in this thesis

An important aspect of the work presented in this thesis is technical: the methodology to simulate biopolymer networks. We use a number of computational techniques to simulate these networks. For the benefit of the reader who is not familiar with these computational techniques, we provide here some background information on some of these methods. Specifically, we discuss the Monte Carlo technique used to form realistic three-dimensional networks; we also explain the Newtonian relaxation technique which we use to find the energy minimum of a network configuration; and in the last subsection we discuss how to calculate the eigenmodes and eigenfrequencies of our networks with the help of the dynamical matrix.

1.6.1 The Monte Carlo method

Before we can study the properties of three-dimensional biopolymer networks, we should first find an adequate way to generate these networks. As discussed above, in two dimensions this generation is relatively easy. If a sufficient number of filaments are randomly placed in a two-dimensional box, there will be plenty of intersections. By placing a crosslink at these places of intersection, a network is generated. In three-dimensions, however, randomly placed one-dimensional objects do never intersect.

To overcome this problem, various approaches have been used. Firstly, one can assign a certain thickness to the filaments so that they become three-dimensional objects. Once two filaments overlap, a crosslink can be formed. By increasing or decreasing the radius of the beam, the density of crosslinks can be varied.

Another approach makes use of molecular dynamics. Here, filaments are placed in a box with a liquid. Due to the thermal excitations of the liquid, the filaments fluctuate and move around in a box. Occasionally, there will be collisions between the filaments, at which point crosslinks can be formed. In practice, with discrete time steps, one can employ a minimal distance criterion: once the distance between two filaments gets closer than some threshold distance, a crosslink is being formed. The process of crosslinking can be accelerated by placing mutually attracting nodes on the filaments [35].

We develop a new method to generate three-dimensional biopolymer networks, with the use of Monte Carlo moves. We will first give some background information

about Monte Carlo methods, and then explain how these can be applied for the generation of well-relaxed biopolymer network configurations.

Many physical systems of interest consist of a large number of degrees of freedom, making it virtually impossible to sample *all* possible states. The general idea of Monte Carlo methods is to sample a limited but large number of states of a physical system, under the condition that the probability of the realization of a specific state should be equal to the probability of this specific state to occur in nature. Under this condition, sampling only a limited number of states gives a good approximation of the average state of the system.

In most Monte Carlo methods, a series of states S_i with $i = 0, 1 \ldots, M$ of the system is generated, in which state S_{i+1} is constructed from S_i via a small change, usually called a Monte Carlo move. Typical Monte Carlo moves are the flipping of a single spin in Ising model simulations, the displacement of a single atom in many-particle simulations, or the breaking of a bond and generation of a new bond in a network simulations. As we stated before, each state should be sampled with the appropriate probability. In the canonical ensemble, the probability for state S_i is proportional to its Boltzmann weight, which is determined by the energy E_i of this state. The proportionality constant is also known as the inverse partition function, and is determined by the energies of all other states. The Boltzmann probability is given by

$$p(S_i) = \frac{1}{Z}\, e^{-\beta E_i}, \tag{1.27}$$

in which

$$Z = \sum_j e^{-\beta E_j} \tag{1.28}$$

where $\beta = 1/(k_B T)$ and the summation is over all states of the system.

A sequence of random changes in the system is unlikely to sample the states with the appropriate probabilities. It is however possible to obtain the appropriate sampling by either accepting or rejecting the Monte Carlo moves with well-chosen acceptance probabilities.

In nature, the ratio between the probabilities of the states of the system before and after the move depends on the energies E_i and $E_{i'}$ of the system before and after the move. In computer simulations, this ratio can be achieved by enforcing a condition known as *detailed balance*; for discrete systems it can be formally written as [37]

$$\frac{P(S_i \to S_{i'})}{P(S_{i'} \to S_i)} = e^{-\beta(E_{i'} - E_i)}, \tag{1.29}$$

where $P(i \to i')$ is the probability of generating the state $S_{i'}$ starting from state S_i.

Most Monte Carlo moves in use today have the property that transitions between states S_i and $S_{i'}$ are unbiased, i.e. the move from one state to the other is equally likely as its reverse move. One way to introduce the appropriate bias favoring low-energy states is to always accept moves which lower the energy, but to reject a fraction of the moves which increase the energy. In detail, the acceptance probability should be

$$P(S_i \to S_{i'}) = \min\left[1, e^{-\beta(E_{i'} - E_i)}\right]. \tag{1.30}$$

This algorithm to decide the probability of acceptance of a Monte Carlo move is generally known as the *Metropolis algorithm* and ensures detailed balance.

For a continuous space, i becomes a continuous variable and one should take into account the volume change of the volume element in the vicinity of the state before and after the change. This is done by calculating the Jacobian determinant of the transformation $\det J$ when determining the acceptance ratio,

$$\frac{P(S(i) \to S(i'))}{P(S(i') \to S(i))} = e^{-\beta(E(i')-E(i))} \det J. \tag{1.31}$$

The other criterion for the Monte Carlo moves is ergodicity. This means that it should be possible to reach any state in the system starting from any other state, if the system would evolve long enough.

We do not use the Monte Carlo method to calculate average values of our networks, but instead use it to generate networks that are representative, i.e. have a high probability to exist in nature. When forming a network out of a couple of hundred filaments in a box, there are extremely many configurations that the network can take. We cannot and do not want to sample all possible network configurations, but instead create a small number of networks that have a high probability to occur in nature. In our generation method, we start from random networks with an unphysically high energy, and then use a Monte Carlo method to evolve these networks into networks that have a high probability to exist in nature, which coincides with having a low free energy. In our case, the Monte Carlo moves are small changes in the topology of the networks, such as breaking bonds between crosslinks and creating new bonds. We choose our moves such that the condition of ergodicity is satisfied. After each Monte Carlo move, the free energy of the network is minimized under the topological constraints. We then apply the Metropolis accept-reject procedure outlined above, based on the minimized free energies before and after the move.

Strictly speaking, we should calculate the Jacobian determinant at every step. This would however render our generation procedure too slow to generate networks of the desired size. We therefore make the approximation that the phase space around each state with minimized energy has the same volume and thus $\det J$ is 1.

A more detailed description of our method is presented in chapter 2.

1.6.2 Relaxation method

During the construction of well-relaxed networks, as well as during the analysis of the properties of the relaxed networks, we need a method to bring the network to a local energy minimum conformation, i.e. a state in which the force on each individual degree of freedom is zero, and which is stable against small perturbations. A large number of energy minimization methods have been developed. One of the most popular methods is the conjugate gradient method. Our specific problem is strongly related to the generation of continuous random networks, for which a the method of choice is different. We refer to this method as local minimization with damped molecular dynamics.

DUring the minimization, the relevant quantities are the position $\vec{x}_{i,t}$, the velocity $\vec{v}_{i,t}$ and the force $\vec{f}_{i,t}$ of crosslink i at iteration t. Initially, the positions are those of the network to be relaxed, and the velocities are set to zero. At all times, the forces are the gradient of the energy, with a sign such that the force points in the direction of lower energy. Then, iteratively, the forces are used to update the velocities, and the velocities are used to update the positions, according to Newton's equations of motion

$$\vec{v}_{i,t+\mathrm{d}t} = \vec{v}_{i,t} + \frac{\vec{f}_{i,t}}{m_i}\mathrm{d}t \tag{1.32}$$

$$\vec{x}_{i,t+\mathrm{d}t} = \vec{x}_{i,t} + \vec{v}_{i,t+\mathrm{d}t}\mathrm{d}t + \frac{\vec{f}_{i,t}}{m_i}\mathrm{d}t^2, \tag{1.33}$$

where $\mathrm{d}t$ is the time step and m_i is the mass of the crosslinks, which we take to be unity. As Newton's equation of motion conserve total energy, i.e., the sum of potential and kinetic energy, the network would not come to a halt, even if it would reach the local energy minimum. To overcome this problem, we need a damping mechanism which extracts kinetic energy. This is obtained by setting the velocity $\vec{v}_{i,t}$ to zero, as soon as the iteration would result in a configuration with a higher energy. With this simple method, we develop a fast algorithm to relax our networks. Within this method of relaxation, it is easy to enforce global constraints.

1.6.3 Dynamical matrix

Small deformations of a network around a local energy minimum can be expressed as a linear combination of the eigenmodes of the network. The mode structure and frequencies of these eigenmodes contain valuable information about the network. In chapter 4 we analyze the eigenmodes. Here, we give some background information on the dynamical matrix, and explain how the eigenmodes and eigenvalues of our networks can be computed numerically.

But first we will turn towards a simple example that will give some basic understanding of the concept of eigenmodes. Consider a particle in vacuum, connected to a spring, having one degree of freedom. See figure 1.12 for a graphical representation of the one-dimensional energy landscape. For small displacements around the equilibrium position, the energy is quadratic and can be written as

$$E = E_0 + a(x - x_0)^2 \tag{1.34}$$

Here, E_0 is the energy at equilibrium and a is an indication of the stiffness of the spring. A small value of a indicates a flat energy landscape and soft deformation, while a high value of a indicates the opposite. If the particle is placed out of its equilibrium position, the restoring motion of this system can be described by

$$f = m\ddot{x} = -\frac{\partial E}{\partial x} = -2a(x - x_0). \tag{1.35}$$

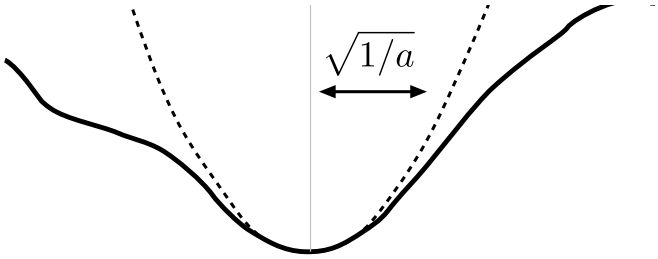


Figure 1.12: Illustration of energy landscape of a particle attached to a spring. The dotted parabola indicates the harmonic approximation, valid for small deviations. The width of the parabola scales with $\sqrt{1/a}$; a is a measure for the stiffness of the spring.

Here, f is the force in the spring, $\ddot{x}$ is the second derivative of the position to time and m is the mass of the particle. According to equation (1.34), $2a = \frac{\partial^2 E}{\partial x^2}$, and thus the equation of motion can be written as

$$\ddot{x} = -\frac{1}{m}\frac{\partial^2 E}{\partial x^2}(x - x_0). \tag{1.36}$$

The solution for this equation of motion is

$$x(t) = A_1 \cos(\omega t) + A_2 \sin(\omega t), \tag{1.37}$$

in which A_1 and A_2 are parameters determined by the initial condition, and

$$\omega^2 = \frac{1}{m}\frac{\partial^2 E}{\partial x^2}. \tag{1.38}$$

The second derivative of the energy thus determines the frequency of oscillation.

Although our networks are systems with $3N$ degrees of freedom, the general picture of the one-dimensional spring is still relevant. In the harmonic approximation, the energy E of the system with $3N$ degrees of freedom at a small deformation can be given by

$$E = E_0 + \sum_{i,j}^{3N} a_{i,j}(x_i - x_{i,0})(x_j - x_{j,0}), \tag{1.39}$$

where $a_{i,j}$ are the elements of a $3N$ by $3N$ matrix and x_i are the coordinates of the crosslinks in the network. Now the equation of motion is given by

$$\ddot{\vec{x}} = \hat{D}(\vec{x} - \vec{x_0}), \tag{1.40}$$

where $\vec{x}$ is the $3N$ dimensional position vector and $\hat{D}$ is the dynamical matrix, defined as:

$$\hat{D}_{i,j} = \frac{1}{\sqrt{m_i m_j}}\frac{\partial^2 E}{\partial x_i \partial x_j}. \tag{1.41}$$

Here, m_i is the mass of the element to which degree of freedom i belongs. The eigenvalues and eigenmodes of the system are the eigenvalues and eigenmodes of the dynamical matrix. All deformations of the network can be expressed as a linear combination of eigenmodes. The eigenvalues indicate the frequency of oscillation of a specific mode, and thus also the speed of relaxation if the network is deformed along this eigenmode. If a network is out of equilibrium but slowly evolves towards it, the eigenmodes with the lowest frequencies are the ones which take longest to relax.

In our networks, we calculate the forces by taking the derivative of the energies. In order to calculate the dynamical matrix, we simply take the numerical derivatives of the forces with respect to the positions. With the help of commercially available routines, the eigenmodes and eigenvalues of the dynamical matrix can be found. These are exactly the eigenmodes and eigenvalues of the whole network, and give insightful information into the deformation of the networks.

We conclude this introduction with an outline of this thesis.

1.7 Overview of this thesis

To describe the physics of biopolymer networks under shear, two main approaches have been proposed in literature. Interestingly, both approaches seem to be complementary. The single-segment affine model assumes an affine deformation and a highly nonlinear force-extension curve of single segments. The network-based models assume a linear force-extension curve of single segments combined with a network relaxation that can be non-affine if that is the state of minimal energy under the constraint of the imposed shear. In this thesis we present a model that combines the typical nonlinear behavior of the single filaments with a network model that allows for non-affine deformation.

In chapter 2 we will introduce this model in more detail. In addition, we give the first results obtained from simulations of this model. These results link both the network stiffness and the non-affinity of the deformation to the filament properties and the network structure. Also, we characterize the amount of order in these networks during deformation and see that the non-affinity enhances the ordering in the networks.

In chapter 3 we use our model to describe composite networks, networks that consist of floppy and stiff filaments. We will see that these networks combine the initial softness of the soft filaments with the large-strain properties of the stiff filaments. Considering the non-affinity and the network modulus gives us insight in the strain partitioning between the soft and stiff filaments. The average forces in the soft and stiff filaments during deformation reveal a self-matching behavior at large strain: the soft filaments stiffen up until they are comparable to the stiffness of the stiff filaments. This example is a great illustration of how the nonlinearity of the single filaments and the nonlinearity of the deformation field enhance each other and give rise to unexpected behavior.

In chapter 4 we look at the network modes and the effect of internal stresses.

We will see that the internal stresses stiffen the networks below the Maxwell rigidity point. Based on a simple mode-counting argument we find an important difference between two-dimensional and three-dimensional filamentous networks. Contrary to 2d networks, in 3d networks the network response is non-affine if the bending of filaments is soft in comparison with stretching of filaments, irrespectively of filament length, unless the network geometry prevents a non-affine deformation. The amount of non-affinity depends upon the relative stiffness of bending versus stretching.

Finally, in chapter 5, we consider network dynamics. We extend our model such that the viscous interaction of the surrounding medium with the polymers is included. We look at the frequency dependence of the network response and find that at high frequencies the network response is affine and dominated by the single-filament behavior. At low frequencies, the network response is non-affine and the network geometry plays an important role in the network response.

CHAPTER 2

GENERATION OF NETWORKS

We present a method to generate realistic, three-dimensional networks of crosslinked semiflexible polymers. The free energy of these networks is obtained from the force-extension characteristics of the individual polymers and their persistent directionality through the crosslinks. A Monte Carlo scheme is employed to obtain isotropic, homogeneous networks that minimize the free energy, and for which all of the relevant parameters can be varied: the persistence length, the contour length as well as the crosslinking length may be chosen at will. We also provide an initial survey of the mechanical properties of our networks subjected to shear strains, showing them to display the expected nonlinear stiffening behavior. Also, a key role for non-affinity and its relation to order in the network is uncovered. There has been some debate whether the origin of stiffening is ultimately entropic or mechanical, but our results suggest that rather, we should focus our attention on the degree of non-affinity which acts to delay and attenuate the stiffening.

2.1 Introduction

Networks of semiflexible polymers have become one of the focal points in current soft matter research. The reason for this interest is twofold: on the one hand, most relevant structural biological materials, both intra- and extracellular, share the common architecture of crosslinked semiflexible polymer networks. In the introductory chapter we presented two archetypical examples, namely the cytoskeleton and the extracellular matrix. At the same time, there is a wide-spread realization that semiflexible networks represent an interesting soft-matter system in their own right, outside of any biological context, resulting in a much more fundamental interest in the microscopic and geometrical origins of their mechanical behavior.

The mechano-elastic characteristics of networks of semiflexible polymers have been studied to analyze and characterize different types of these networks, both in vivo [38], and in vitro [7]. As discussed in chapter 1, the contributions of theory have been many and insightful, but analytical progress has typically only been possible in certain limiting cases where simplifying assumptions may be believed to hold, most notably the assumption of affine deformations [15, 27]. At the same time, computer simulations have been used to study these networks, but they too have had to rely on simplifications - either reducing the system to two dimensions and limiting to the small-strain regime [32, 33] or ignoring the nonlinear nature of the constituent filaments [34, 35].

We believe that the time is right for more realistic numerical modeling of these networks that allows for a detailed microscopic look at the relations between structure, geometry and mechanical properties. To this end, we present a computer model to simulate these semiflexible polymer networks in three dimensions. Networks are considered to consist of filaments, described as semiflexible polymers. These filaments are crosslinked in various locations, which might induce extra bending of filaments, thus increasing the free energy of the system. We start with a homogeneous, isotropic initial random network with a high free energy, and employ a Monte Carlo scheme to relax this network. This approach allows us to generate realistic three-dimensional networks containing hundreds of crosslinks, which are nonetheless well equilibrated and thus represent realistic initial conditions for further mechanical loading in three dimensions. The methodology to generate such networks is the first main result presented in this chapter, and is described in the first part of this chapter.

In the second part of this chapter, we subject these networks to shear, and analyze their behavior as a function of the network parameters, e.g. the stiffness and the length of the filaments. The results of these computer experiments are compared with experiments to validate our model, and yield novel predictions for the mechanical behavior of semiflexible networks.

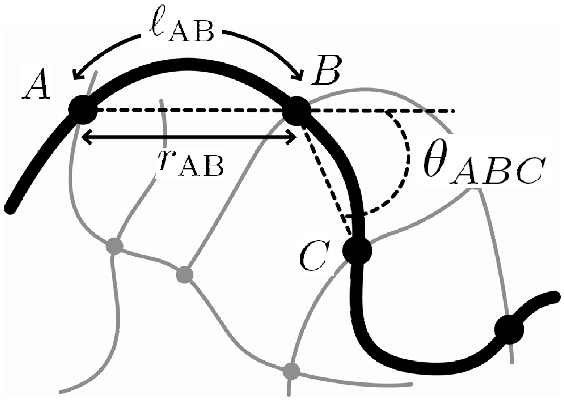


Figure 2.1: Schematic presentation of (part of) a semiflexible network, in which lines indicate the filaments and dots the crosslinks. The section of the filament between crosslinks i and j has length $\ell_{\mathrm{c,ij}}$ and end-to-end distance r_{ij}. θ_{jkl} denotes the angle between two end-to-end vectors of neighboring segments along the same filament.

2.2 Network generation and equilibration

We begin our discussion with a detailed look at the generation of our semiflexible networks based on single polymer energies, and how the Metropolis-Monte Carlo scheme is implemented and adapted for our specific purposes.

2.2.1 Network free energy

The networks considered in this thesis consist of filaments, which are linked by crosslinks $i = 1 \ldots N$. Figure 2.1 shows a schematic representation of a part of the network, indicating important parameters of the network and the notation used. As introduced in the introductory chapter, each filament is an inextensible semiflexible chain, whose energy in the presence of an external force is given by

$$E_{\mathrm{fil}} = \int_0^{\ell_{\mathrm{c}}} \left(\frac{\kappa}{2} \left| \frac{d\hat{t}_\perp(s)}{ds} \right|^2 + \frac{f}{2} \left| \hat{t}_\perp(s) \right|^2 \right) \mathrm{d}s, \tag{2.1}$$

where s is the arc length coordinate running along the filament, κ is the bending stiffness which is related to the persistence length ℓ_{p} as $\kappa = \beta^{-1}\ell_{\mathrm{p}}$, with $\beta = 1/(k_b T)$, $\hat{t}_\perp(s)$ is the transverse component of the (unit) tangent vector along the filament, and f is the applied force, directed along the end-to-end vector of the polymer. The filamentous contribution to the total energy of a network is the sum of the energies of all filaments. In this chapter we consider inextensible filaments, thus ignoring backbone stretching of the filaments, a deformation that is only relevant at high forces for most biopolymers.

A brief note on our nomenclature: our networks consist of (multiply) connected *filaments*. Each of these filaments is partitioned into *segments*, which begin and end in *crosslinks*. A filament can thus consist of many segments, but is always a single mechanical entity, satisfying persistence not just at the segment level but also through crosslinks.

Each crosslink connects segments of two filaments, and our networks are therefore strictly tetrafunctional - albeit with the possibility of dangling ends which are discarded (we do not take steric avoidance into account). Compared to the other scales in the network, crosslinks are assumed to be exceedingly small so that their only action, effectively, is to force a binary bond between two distinct filaments, or remote regions of the same filaments.

In our computer simulations, we store a complete list of all positions $\vec{x}_i$ of the crosslinks, a complete list of the contour lengths $\ell_{\mathrm{c,ij}}$ of the segments between crosslinks i and j, and a connectivity table which lists which segments are linked by each of the crosslinks. We do not keep track of the spatial configuration of a segment between two crosslinks. Instead, we use the exact radial distribution function as computed from equation (2.1) [39] to assign to each segment a contour length drawn from the radial distribution function computed at the segment's end-to-end length and persistence length. In this manner, we can already perform an important part of the full ensemble sampling in a straightforward manner: different assignments of the contour lengths correspond to different realizations of semiflexible networks with a prescribed spatial distribution of crosslinks. The relative likelihood of a given distribution of lengths is computed from the free energy of the resultant network, which we compute as follows.

For a given network realization we partition the free energy in an internal segment part F_2 and an inter-segment part E_3. As stated above, the internal degrees of freedom of the segments are integrated out. Thus, we express the free energy of a segment as a function of the distance between the crosslinks (r_{ij}) and the length of the segment ($\ell_{\mathrm{c,ij}}$). If the applied force f in equation (2.1) is positive (i.e., stretching the filament), F_2 can be computed from equation (2.1) by employing a semiflexible analogue of the Marko-Siggia interpolation formula [40]; an expression for this is given in the next section. The semiflexible WLC force-extension formula is not particularly accurate for negative forces, as the filaments quickly assume configurations with considerable transverse displacements under compressive loading. The crucial feature of compressive loading, however, is that the forces involved are always considerably smaller than those encountered for extensional loads - indeed, this asymmetry in the force-extension curve is responsible for many mechanical features of semiflexible networks. For negative forces, we find that the force-extension is adequately described by an exponential approach to the asymptote set by the classical Euler buckling force. Integrating the force-extension curve yields the following ex-

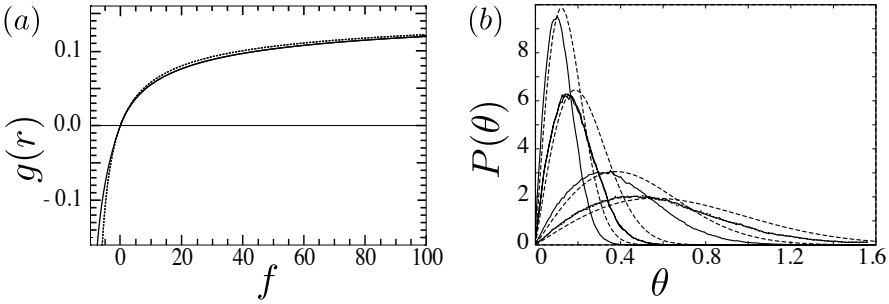


Figure 2.2: Validation of our effective Hamiltonian. a) Analytic force-extension curve (straight line) (see [30]) vs. interpolation formula of force-extension (dotted line), where f is the force on the segments and $g(r)$ the relative extension with respect to the equilibrium configuration. b) The distribution $P(\theta)$ of the angle θ between two segments, for different ratios ℓ_1/ℓ_2 between the lengths of the first (ℓ_1) and the second (ℓ_2) segment and for the persistence length ℓ_p, related to the total length L of the two segments, $L = \ell_1 + \ell_2$. The straight lines are are obtained from Monte Carlo simulations of long polymers, the dotted lines are our approximation (equation (2.4)) using the same values for ℓ_1, ℓ_2 and ℓ_p/L. From top to bottom the figure shows respectively the (simulated and approximated) curves for $\ell_p/L = 33.3$, $\ell_p/L = 14.3$, $\ell_p/L = 3.33$ and $\ell_p/L = 1.43$. For the simulated curves, we used for the upper curve $\ell_1/\ell_2 = 1/2$. The second-upper curve is a double curve, showing both $\ell_1/\ell_2 = 6$ and $\ell_1/\ell_2 = 2/5$, the third-upper curve shows $\ell_1/\ell_2 = 1/2$. The bottom curve is a double curve, showing both $\ell_1/\ell_2 = 1/6$ and $\ell_1/\ell_2 = 2/5$. The figure shows that $\ell_1 + \ell_2$ is the length on which the distribution depends. The shape and the peak of the distributions of our approximation are in decent agreement with the simulated curves.

pression for the energy

$$\beta F_2 = \begin{cases} -\frac{9g(r_{ij})^2(5+6g(r_{ij}))}{-1+6g(r_{ij})} & \text{if } f > 0 \\ |(-\frac{1}{90}(-1+\exp(90g(r_{ij})/\pi^2))\pi^4+\pi^2)| & \text{if } f < 0 \end{cases} \tag{2.2}$$

where $g(r_{ij})$ is the scaled extension given by:

$$g(r_{ij}) = -\ell_p/\ell_{c,ij} + 1/6 + \ell_p r_{ij}/\ell^2_{c,ij}. \tag{2.3}$$

These equations are not only computationally convenient, they also provide an excellent fit to the full, analytical force-extension curves as shown in figure 2.2a, where we plot the force vs. the scaled extension $g(r_{ij})$. In addition to the single-segment force-extension, we also need to keep track of their persistence through crosslinks. There is no analytical formula for this contribution, and we have therefore simulated many individual filaments to obtain a reliable numerical expression

for this contribution. If the applied force f in equation (2.1) is positive (i.e., stretching the filament), it turns out that we can capture the essential behavior by

$$\beta E_3 = \frac{\ell_{\mathrm{p}} \theta_{ijk}^2}{\ell_{\mathrm{c,ij}} + \ell_{\mathrm{c,jk}}}, \tag{2.4}$$

where $\ell_{\mathrm{c,ij}}$ and $\ell_{\mathrm{c,jk}}$ are the contour lengths of the segments and θ_{ijk} is the angle between the two end-to-end vectors of the segments. Note that this contribution to the total energy is not accompanied by an entropic contribution, since it is defined by explicit variables in our network.

To assess the quality of the segment-segment energy function, we compare the distribution function of this energy with simulations. We simulate a single wormlike chain of length L_w, at a fixed temperature and a persistence length ℓ_{p}, and count the probability $P_{\mathrm{wlc}}(\theta)$ of an angle θ between the vectors $\vec{r}_{L_w} - \vec{r}_N$ and $\vec{r}_N - \vec{r}_1$. Here, N is anywhere on the chain. Our approximate expression for this probability is $P_{\mathrm{app}}(\theta) \sim N(\ell_{\mathrm{p}}/(\ell_{\mathrm{c}_1} + \ell_{\mathrm{c}_2}))\theta \exp(-\beta E_3(\theta))$, in which the energy E_3 is given by equation (2.4) and $N(\ell_{\mathrm{p}}/(\ell_{\mathrm{c}_1} + \ell_{\mathrm{c}_2}))$ is a normalization factor. This histogram is plotted in figure 2.2b. Although the correspondence is not perfect, this formula does reflect the essentials of the angle distribution, capturing the broadening and shift of its peaks.

In summary, we attribute to a specific network configuration an energy which is the sum of single-segment energies given by equations (2.2), plus a sum over all segment-pair energies given by equation (2.4), which runs over all pairs of segments belonging to the same filament and meeting in the same crosslinks.

2.2.2 Interpolation formula for the segment free energy

Equation (2.1) enables us to derive an analytic approximation for the semiflexible force-extension relation. To simplify notation, we will pass to dimensionless quantities, rescaling all forces by a factor of $\ell_{\mathrm{c}}^2/\kappa$ and all lengths by $\ell_{\mathrm{p}}/\ell_{\mathrm{c}}^2$. Based upon equation (2.1), we can express the scaled difference between the total rescaled length of the polymer ($\tilde{l}_c$) and the end-to-end length at rescaled force ϕ ($\tilde{l}_\phi$) as [15]:

$$\tilde{\ell}_{\mathrm{c}} - \tilde{\ell}_\phi = \frac{1}{\pi^2} \sum_{n=1}^{\infty} \frac{1}{n^2 + \phi}, \tag{2.5}$$

which gives:

$$\tilde{\ell}_{\mathrm{c}} - \tilde{\ell}_\phi = \frac{-1 + \sqrt{\phi}\coth\sqrt{\phi}}{2\phi}. \tag{2.6}$$

At zero force this gives $\tilde{\ell}_{\mathrm{c}} - \tilde{\ell}_0 = 1/6$. With this, we can define the differential extension at force ϕ (i.e, the incremental extension compared to that at zero force) as $\delta\tilde{\ell} = \tilde{\ell}_\phi - \tilde{\ell}_0$. We use these equations to construct an interpolation formula for $\phi(r, \ell_{\mathrm{c}}, \ell_{\mathrm{p}})$, which is the direct analogue of the Marko-Siggia interpolation for the WLC [40]. Around $\tilde{\ell}_0$ equation (2.6) gives as a first order approximation:

$$\phi = 90\delta\tilde{\ell}. \tag{2.7}$$

In the large force regime we can expand equation (2.5) to yield

$$\phi = \frac{1}{4(1/6 - \delta\tilde{\ell})^2}. \tag{2.8}$$

Tying the two asymptotes together yields

$$\phi = -18\delta\tilde{\ell} + \frac{1}{4(1/6 - \delta\tilde{\ell})^2} - 9, \tag{2.9}$$

which can be integrated once to yield equation (2.2). Figure 2.2a shows the comparison between this formula and the exact solution - the difference between the two does not exceed 6%.

2.2.3 Network generation

The task at hand is obviously to determine network configurations that minimize the free energy thus defined. To this end, we use a Monte Carlo minimization scheme as introduced in section 1.6.1: starting from an isotropic, random network, we propose random changes in topology, each of which is either accepted or rejected according to the Metropolis criterion.

The initial network is constructed by placing m nodes with random coordinates in a cubic periodic cell. To connect these nodes into a four-fold coordinated network, we proceed iteratively: we begin by identifying three nodes which are close to each other and connect these with a loop of three bonds. This loop is then extended one bond at a time: we identify a node A which is not fully connected and which is closest to an existing bond BC, and then replace this existing bond by two bonds AB and AC. This process is repeated until all nodes are four-fold connected.

In the resulting fully fourfold-coordinated network, each bond is considered to be a segment of a single, long filament. This network as a whole can therefore be considered a single, circular filament which is crosslinked to itself at various places. We then proceed to minimize the free energy - computed as detailed before - of this initial network, using the standard local minimization method of damped molecular dynamics, see section 1.6.2.

The initial network will be highly stressed, and in general far removed from a realistic equilibrium configuration. Chiefly, this is due to considerable filament bending, with intra-filament bends at crosslinks often exceeding 90 degrees. As initial large strides towards an optimal configuration will proceed along downhill directions related to the release of precisely these dominant bending stresses, we first focus on rearranging the topology of the network, analogous to the continuous random network approach, pioneered by Wooten, Winer, Weaire [41] and further extended and optimized as detailed in [42]. This is realized by a series of Monte Carlo moves that alter the topology; these are moves (a) and (b) in figure 2.3. To the initial configuration with a topology L' with minimized coordinates $\vec{x}'$, we assign a free energy F' as obtained from equation (2.4) plus a quadratic function around the average bond

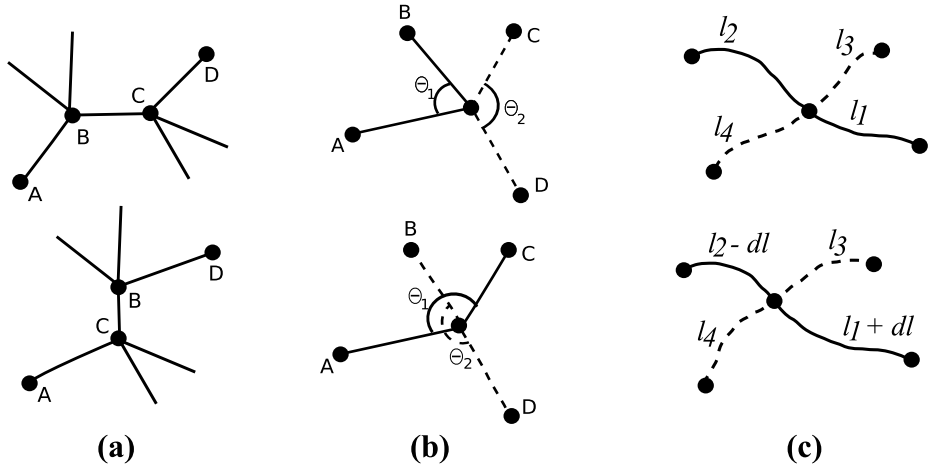


Figure 2.3: Schematic representation of the three Monte Carlo moves. a) Four crosslinks that are connected as shown in the above figure, are randomly selected in the network. Bonds AB and CD are broken and bonds AC and BD are created, such that the configuration of the lower figure is formed after energy relaxation. b) A crosslink is randomly chosen at which crosslinks A and B are part of the same filament, as are crosslinks C and D (above figure). Now A and C become part of the same filament as do B and D. This alters the three-crosslink free energy, E_3. c) A randomly chosen length ($d\ell$) is removed from the length of one segment of a filament and transferred to a neighboring segment of the same filament, such that the configuration of the lower figure is formed after relaxation.

distance, to prevent crosslinks from clustering and to tune the final network topology. The average bond distance determines whether the final network will be densely or loosely crosslinked. We then change the topology to L'' by one of the moves, and relax the network with this new topology, resulting in the new coordinates $\vec{x}''$ and a new free energy F''. Depending on the change in free energy $\Delta F = F'' - F'$, the topological change is accepted or rejected, using the Metropolis algorithm. Note that in this stage, we assume that the free energy of a network with minimized crosslinks coordinates is representative for the free energy of all networks with the same topology, up to some additive constant that is topology-independent.

Once such topology altering moves no longer significantly affect the overall energy - this typically happens in configurations where the bending angle of the filament in each node is on average around 20 degrees - contour lengths are attributed to the segments. As explained, for a segment AB with end-to-end distance r_{AB}, the length $\ell_{\mathrm{c,AB}}$ is drawn from the corresponding distribution for the WLC with the desired persistence length ℓ_{p}. Next, we chop up the single continuous filament into many smaller ones, by random deletion of segments under the constraint that all crosslinks stay connected, up to the point where the desired number of filaments (or, alternatively, mean filament length) is reached. This network is then further equilibrated with the Monte Carlo moves (b) and (c) shown in figure 2.3, each of which is now accepted to a comparable degree. To avoid computational instabilities for floppy filaments we add a short-range repulsive force between crosslinks. A typical network generated with this approach is shown in figure 2.4.

2.3 Mechanical response of the network

The ultimate goal is to understand the relationship between the structure of a network and its mechanical properties. In the following sections, we explore some of the basic mechanical properties of our system in an attempt to check whether well-known behavior is correctly reproduced, and simultaneously to offer a glimpse of the relevant microscopic processes that we are now able to study in detail and their role in the overall mechanics.

The behavior of biopolymer networks under strain depends on many experimental parameters, such as the concentration of biopolymer, the amount of capping proteins and the concentration and characteristics of binding proteins. In our simulations, we can reproduce such changes by varying the crosslinking length, the persistence length and the average number of crosslinks per filament. In this chapter we consider networks that consist of thousand crosslinks and two thousand segments, of which some are the floppy ends of filaments, which are not taken into account in our simulations during deformation. Our networks are densely crosslinked, which implies that the average distance between crosslinks along filaments is about the same as the average distance between crosslinks. This allows us to ignore the steric interactions due to entanglements, since it hardly happens that two filaments are nearby but not connected. Since we do not take into account excluded volume effects, our

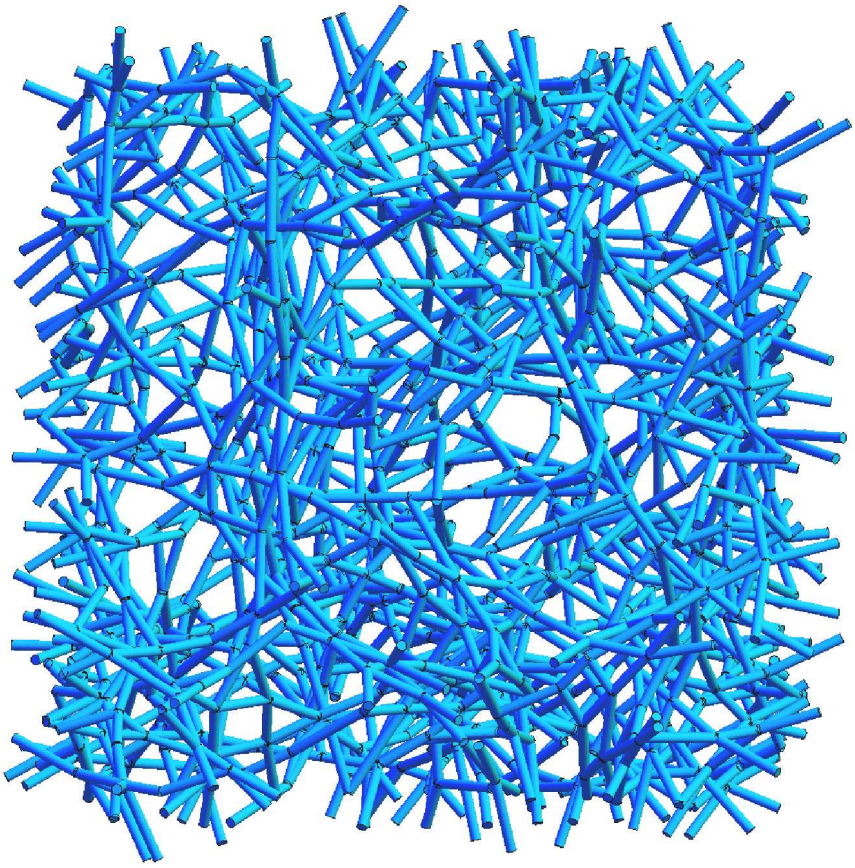


Figure 2.4: Representation of a generated network. This network consists of 333 filaments, each on average crosslinked six times. Note that the undulations of the segments are not represented. The network has periodic boundary conditions: a filament leaving the periodic cell on one side, enters it on the opposite side.

data are only representative for networks of relative low densities, as they are usually found in nature. The persistence length in the networks we use ranges from $\ell_p/\ell_c = 1$ to $\ell_p/\ell_c = 16$ and the average length of filaments from $L/\ell_c = 3$ to $L/\ell_c = 20$. All data presented in this chapter comes from simulations of single networks that are as large as feasible, rather than averaging over multiple small networks, to minimize finite-size effects.

The experimental techniques used to probe the mechanical response are essentially twofold: on the one hand, in vitro networks are often subjected to global shears in commercial rheometric setups to characterize their macroscopic viscoelastic properties [16, 43]. On the other hand, many experiments focus rather on the microscopic processes involved by injecting small particles ($\sim 1\mu m$) in the network to monitor the behavior at the filament scale of the network [19, 20]. Our computational method allows us to work at both levels by direct and simultaneous measurement of the overall stiffness as well as all individual displacements and forces in the system, to high accuracy.

We model shearing by virtually displacing all crosslinks positions affinely by small shear-increments of 0.2 %. After each shear-increment we allow for non-affine relaxation of all individual crosslinks in order to minimize the free energy of the network, as explained in section 1.6.2. During this procedure the forces and displacements are recorded and can be used for further analysis of the network response. It's important to note that we allow for full relaxation after each strain increment - this would be appropriate for adiabatically slow shears and should therefore be compared to the zero-frequency limit in oscillatory rheology, as indeed we shall do.

2.3.1 Strain stiffening

To characterize our networks, we first consider the differential stiffness, $K = \partial\sigma/\partial\gamma$ during shear. An important and characteristic feature of these networks is their highly nonlinear stiffening behavior under relatively small shear stresses [16]. As argued in Ref. [15], all experimental curves of the modulus of networks of semiflexible polymers collapse for small shears on a master curve by scaling the stiffness by the initial stiffness (K/K_0) and scaling the shear by its value at which the stiffness is four times the initial stiffness (γ/γ_4). Figure 2.5a shows the scaled strain-stiffness curves of our networks under shear, where we plotted the differential modulus K, as a function of shear for different ratio's between ℓ_p and ℓ_c (the average contour length of the segments). We observe the same universal scaled stiffening behavior as observed in experiments, of which some examples are given in figure 1.6. For comparison, we plotted the theoretical curve that incorporates the typical force-extension curve of single filaments combined with the assumption that the filaments deform affinely, that has shown to represent this same master curve. Note that we do not account for rupture and backbone stretching of the filaments, which becomes relevant at larger shears. Figure 2.5b shows the original curves, where one clearly sees an increase in the initial stiffness as well as a small decrease in the strain at which the networks start to stiffen by increasing the stiffness of individual filaments. In our simulations,

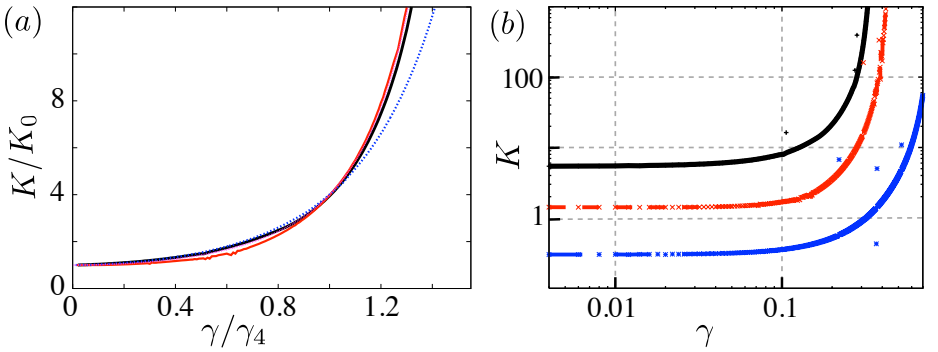


Figure 2.5: a) Master curve of scaled differential modulus as a function of scaled shear-strain γ/γ_4, where γ_4 is the strain at which the modulus is four times the initial modulus G_0. For the curves shown the average number of crosslinks per filament is $L/\ell_c = 6$. The values for the scaled persistence length ℓ_p/ℓ_c used are 15.7, 3.81 and 0.77, of which only the latter is distinguishable at large strains (dotted blue line). Besides, we plotted the scaling from affine theory, which overlaps with the other curves. b) The original strain-stiffness curves with the following values for the scaled persistence length (from top to bottom): 15.7, 3.81 and 0.77. Note that we plot all data points and draw a curve through them. However, a couple of the data points lies well outside the curve (see section 2.3.3).

$\ell_p/\ell_c \approx 16$ is more or less comparable with an actin network with an average distance between crosslinks of 1 μm and an average filament length of 6 μm. Smaller values of ℓ_p/ℓ_c represent networks of filaments with a lower persistence length like fibrin or networks that are less dense.

Another way to compare our results with experiments is to look at the scaling in the large strain limit. By superposition of a small oscillatory stress on a prestress, the differential modulus can be experimentally measured. From these measurements it is known that $K \sim \sigma^{1.5}$ for large stresses σ [18]. We plotted K/K_0 vs. σ/σ_c, where σ_c is the critical stress, defined as the intersection between the horizontal low-stress regime and the high-stress asymptote. As shown in figure 2.6, all our networks show the same characteristic scaling behavior at large shears. Combined with the observed stiffening, this indicates that we capture the essential physics in our model, both at small and large shears.

Equation (2.7) indicates that the initial stiffness of individual filaments scales as $K_{0,fil} \sim \ell_p^2/\ell_c^4$. We expect this scaling behavior to change when the filaments are placed in a network that allows non-affine reorientations, as is the case in our simulations. Since all filament properties scale with ℓ_p/ℓ_c^2, we plot K vs ℓ_p/ℓ_c^2, see figure 2.7a. The figure shows that $K_0 \sim (\ell_p/\ell_c^2)^1$ which emphasizes that for non-affine deformations the persistence length of the constituent filaments is less important for the overall network behavior, as filament reorientations allow for an alternative route

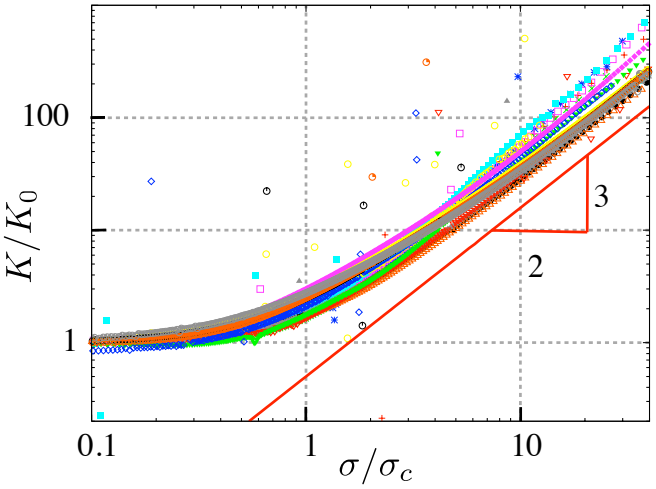


Figure 2.6: Differential modulus of the networks as a function of the scaled shear stress σ for 18 networks with varying ℓ_p/ℓ_c and L/ℓ_c.

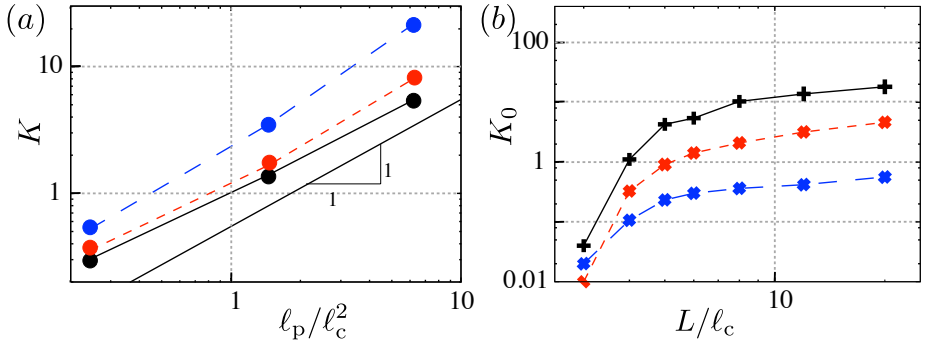


Figure 2.7: a) Differential modulus K as a function of ℓ_p/ℓ_c^2. The three curves show the values at different strains γ (from bottom to top): 0.02, 0.10 and 0.20. For all curves shown $L/\ell_c = 6$. b) K at $\gamma = 0$ as a function of L/ℓ_c for various ℓ_p/ℓ_c (upper line: $\ell_p/\ell_c = 15.7$, middle line: $\ell_p/\ell_c = 3.81$, bottom line: $\ell_p/\ell_c = 0.77$).

to comply with the imposed strains. For increasing γ, the steepness of the slope increases, which strongly correlates with the stiffening of the networks.

From experiments [19] and simulations [23, 35] it is known that the average filament length influences the network response. In cells many capping proteins are active that can control the length of the filaments, thus changing the mechanical properties. We measured the initial stiffness K_0 as a function of the average filament length L and ℓ_p. L/ℓ_c can be considered as the average number of crosslinks on a filament, which we can vary while keeping ℓ_c constant. As expected, figure 2.7b shows a decrease in K_0 if the average filament length decreases. Segments of the same filament influence each others displacements, thus restricting the freedom to adapt to stresses. Besides, when crosslinks connect two or three segments instead of four, these crosslinks are more flexible to reorient when sheared. Therefore, networks with short filaments are softer during shearing.

Figure 2.7b also shows that the stiffness becomes nearly zero for short filaments, a behavior independent of ℓ_p. This decrease is related to the percolation of the network. When the filaments become too short, no real network will be formed. In that case, shearing will shear the liquid in which the filaments are immersed, but the filaments will not be constrained in their movement and thus the stiffness will vanish. Please note that we employ a specific procedure to remove material from the network to generate increasingly sparse networks, which implies that the filament length at which the modulus vanishes cannot be directly related to experiments. The overall trend, however, is representative of real networks. In chapter 4 we discuss the percolation transition in biopolymer networks in more detail.

2.3.2 Non-affine behavior and ordering

While the system deforms in our simulations we allow for non-affine reorientations of the segments. It has been suggested that such non-affine deformations greatly alter the mechanical response [34], and indeed we find that this is true. In section 1.3 we gave a phenomenological description of non-affinity based upon a couple of examples. Here we give a formal definition and a couple of measures of non-affinity. In general, an applied macroscopic strain maps any material point $\boldsymbol{x}$ in the reference space in the network onto a new point $\boldsymbol{x}'$ in the target space. The location of the point in the target space may be thought of as arising from a combination of an affine deformation and a non-affine contribution:

$$\boldsymbol{x}' = \Lambda(\gamma)\boldsymbol{x} + \boldsymbol{\Delta}(\boldsymbol{x}, \gamma) \quad , \tag{2.10}$$

where $\Lambda(\gamma)$ is the deformation gradient tensor, which for the case we consider - three-dimensional simple shear in the $\hat{x}_1$-direction - is given by

$$\Lambda(\gamma) = \begin{pmatrix} 1 & \gamma & 0 \\ 0 & 1 & 0 \\ 0 & 0 & 1 \end{pmatrix}. \tag{2.11}$$

The observation that the non-affine contribution $\boldsymbol{\Delta}(\boldsymbol{x},\gamma)$ depends both on the applied strain and the (original) location of the point under consideration immediately raises the question of what, precisely, it means for a system to be affine. In the strictest sense, an affine system may be defined as one obeying $\boldsymbol{\Delta}(\boldsymbol{x},\gamma)=0$ for all $\boldsymbol{x},\gamma$. This definition, however, is highly restrictive as it does not allow for *any* non-affine motion at any point. For systems that do behave non-affinely to some extent, the most general measure of the extent of this non-affinity was shown in [26] to be the non-affinity correlation function

$$A_{ij}(\boldsymbol{x},\boldsymbol{x}';\gamma,\gamma') = \langle \Delta_i(\boldsymbol{x},\gamma)\Delta_j(\boldsymbol{x}',\gamma')\rangle, \tag{2.12}$$

where the average $\langle\ldots\rangle$ is over all crosslinking points in the network. Both its spatial dependence and the strain dependence are of interest - in a moment we will investigate the strain dependent aspects by focusing on the trajectory that single points trace out during a deformation. Following [26], we shall measure to this end the equal argument limit of the trace of $A_{ij}(\boldsymbol{x},\boldsymbol{x}';\gamma,\gamma')$ which we shall call simply $A(\gamma)$:

$$A(\gamma) = \frac{1}{\gamma^2}\langle|\boldsymbol{\Delta}(\boldsymbol{x},\gamma)^2|\rangle. \tag{2.13}$$

Note that this measure need not approach zero at large strains, even though one may expect all segments to become aligned with the direction of maximal strain in this limit and experience, in effect, a purely extensional strain. The reason $A(\gamma)$ does not tend to zero lies in the fact that even though the deformation becomes *differentially* affine, it does not become affine in the absolute sense. To focus on this differential affinity, which we feel is a more appropriate measure of (asymptotic) affinity, we introduce a second measure by considering the differential displacement from the initial point $\boldsymbol{x}_i$ to the final point $\boldsymbol{x}_f$ before and after a small strain increment $\mathrm{d}\gamma$:

$$\boldsymbol{x}_f = \Lambda(\mathrm{d}\gamma)\boldsymbol{x}_i + \tilde{\boldsymbol{\Delta}}(\boldsymbol{x}_i,\gamma+\mathrm{d}\gamma). \tag{2.14}$$

We use this to define the differential non-affinity measure

$$\delta A(\gamma) = \frac{1}{(\mathrm{d}\gamma)^2}\langle|\tilde{\boldsymbol{\Delta}}(\boldsymbol{x},\gamma)^2|\rangle. \tag{2.15}$$

This measure *does* go to zero as γ becomes very large. Later, our simulations will show that we do not expect this limit to be attained in experiments as, for realistic parameter values, the system will have failed long before. A and δA may be expressed in terms of each other, and the latter tending to zero implies that asymptotically, A should become constant with the magnitude of this constant reflecting the overall strength of the past non-affinity.

Ultimately, we are interested to see to what extent non-affinity affects the mechanical response. To monitor this influence, we perform a shear without relaxation after each strain increment, thus obtaining K_{aff}. Figure 2.8a shows both K_{aff}, which is independent of L/ℓ_c, and K for networks with different filament length, all having

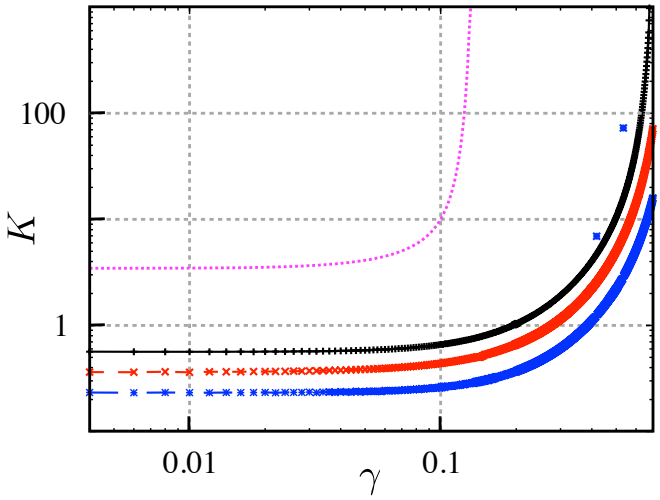


Figure 2.8: Non-affine behavior of the networks during shearing. The differential modulus K measured during affine deformation (upper, dotted line) and during non-affine deformation (from bottom to top: $L/\ell_c = 5.0$, $L/\ell_c = 8.0$, $L/\ell_c = 20.0$). For all networks $\ell_p/\ell_c = 0.77$.

$\ell_p/\ell_c = 1$. As can be seen, even for long filaments, the difference between affine deformation and non-affine deformation is striking, both for he initial modulus K_0 and for the onset of stiffening. This puts the so-called linear (*i.e.*, small-strain) regime of network elasticity in a new perspective: even though the strains are small, there is always a finite amount of non-affinity which greatly affects the overall small strain response. It is thus crucial to understand the role of non-affinity, even at small strains, to predict the network modulus.

Even though the Hamiltonian of the network remains the same, the difference between the strain-stiffness curves is striking. These differences can only be due to non-affine behavior of the network, as all other determinants - topology, filament length, density and persistence length, are identical. There has been some debate whether the origin of stiffening is ultimately entropic or mechanical, but our results suggest that rather, we should focus our attention on the degree of non-affinity which acts to delay and attenuate the stiffening.

To see whether our systems tend to affinity at the largest strains, we measure the differential non-affinity δA as a function of the applied macroscopic strain. To relate δA to other length scales in the system, we plot $\delta A/r_c^2$, where r_c is the average distance between crosslinks. Figure 2.9a shows a strong increase in δA with increasing strain. Figure 2.9b reveals a strong correlation between the stiffening of the networks and the amount of non-affine displacements. Apparently, to prevent the extreme extension that filaments would experience at high strains in an affine setting, the net-

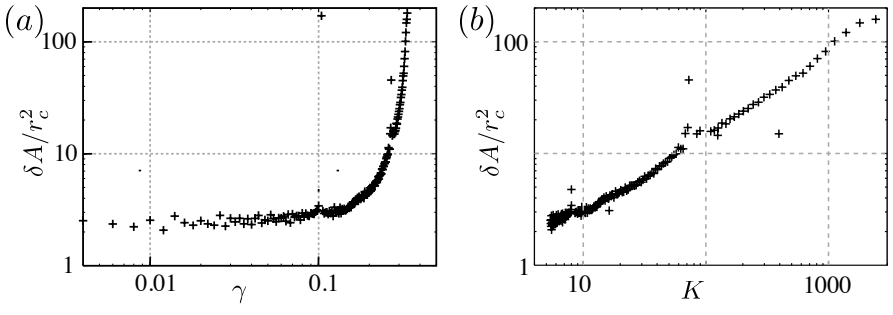


Figure 2.9: a) Differential non-affinity δA as a function of strain for different ℓ_p/ℓ_c. For all curves, $L/\ell_c = 6$. To relate δA to other length scales in the system, we plot $\delta A/r_c^2$, where r_c is the average distance between cross-links. A value of 1.0 implies that the average non-affine displacement is equal to r_c if γ would be 1.0. b) The stiffness vs. the differential non-affinity during deformation.

work shows a strong non-affine reorientation. As indicated before, we expect that for high shear all filaments will be aligned in the direction of shear and deform purely by stretching. Since stretching is an affine deformation, we expect δA to ultimately tend to zero at large strain. This figure and the inset make it clear that this asymptotically (differentially) affine regime is never actually attained, and non-affinity will continue to feature prominently all the way up to the point of failure.

Shorter filaments, or filaments that are less densely crosslinked, are less constrained in their motions which should, in principle, allow for greater non-affine motions. To verify whether indeed this is the case, we evaluate the non-affinity as a function of filament length. To better compare to existing experiments, we shall use A, the overall non-affinity parameter, instead of the differential measure δA. Figure 2.10a indeed shows a pronounced increase in non-affinity as the length decreases. This is in agreement with experiments on f-actin, which also show an increase in $A(0)$ for decreasing filament length [19]. Translating $A(0)$ to real distances gives for actin with an average $\ell_c = 1\mu m$ values between $2-6\mu m^2$, which is close to the values between $2-10\mu m^2$ reported for experiments [19]. Besides the length dependence, we also observe a dependency of ℓ_p on the non-affinity: networks of stiffer filaments behave more non-affinely. This suggests that asymptotically, we recover the classical picture of rubber elasticity (which does very well for long, flexible polymers but rather poorly for semiflexible systems): as the persistence length decreases, the polymer configurations become increasingly random (i.e., Gaussian) which is accompanied by a decrease in the non-affinity. This is precisely the rubber limit: Gaussian polymers deforming affinely. Note that these non-affine deformations are the sole possible origin of the large difference in stiffness between affine and non-affine deformations shown above. Thus, even though the magnitude of the non-affine deformations is small, they do have an important effect on the network response. This is a striking exam-

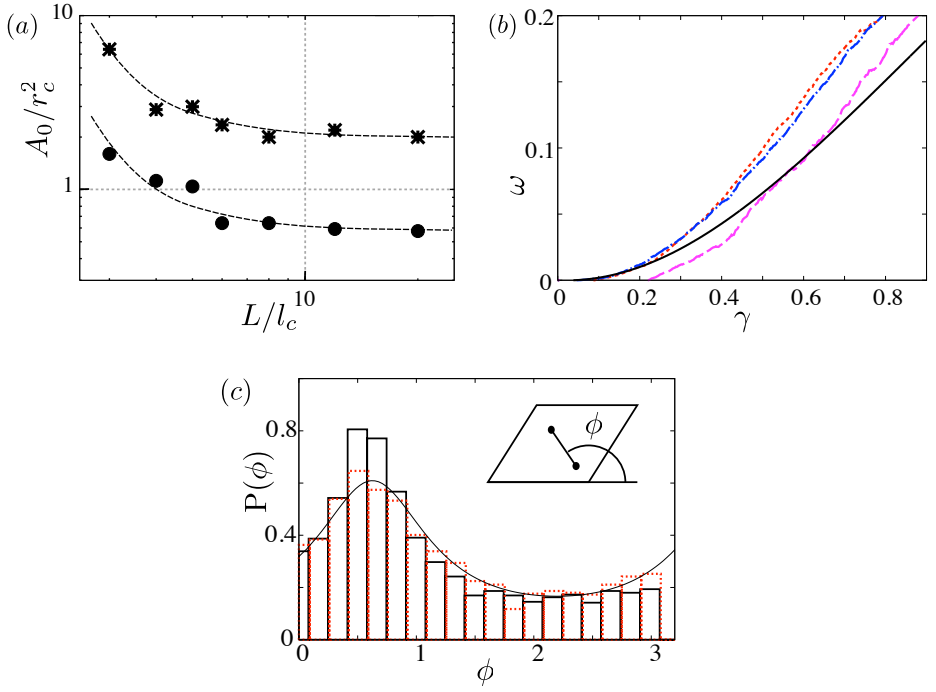


Figure 2.10: Non-affine behavior of the networks during shearing. a) The scaled overall non-affinity A/r_c^2 at $\gamma = 0$ as a function of L/ℓ_c for different persistence lengths: $\ell_p/\ell_c = 0.77$ (•) and $\ell_p/\ell_c = 15.7$ (∗). Curves are drawn as a guide to the eye. b) Ordering during shearing. Due to the limited number of segments and correlated ordering of segments along filaments, the initial values for ω differ slightly from zero. However, for comparison, we set $\omega_0 = 0.0$. The straight line indicates the ordering due to affine shearing. The dotted lines indicate the ordering during shearing in networks with (from bottom to top) $L/\ell_c = 4.0$, $L/\ell_c = 6.0$ and $L/\ell_c = 12.0$. c) Distribution of angles with respect to the x-axis, both for an affine deformation (dotted bars) and a non-affine deformation (straight bars) at $\gamma = 0.7$. The curve is the analytic expression for the angular distribution of an initially isotropic material at shear $\gamma = 0.7$. Inset shows the sheared box, in which two crosslinks that are connected are indicated by dots. Their end-to-end vector makes an angle ϕ with the $\hat{x}$-axis.

ple of the value of simulations in this field: microscopic structure and motion are of crucial importance to properly understand the macroscopic behavior.

Apparently, the macroscopic result of the microscopic non-affinity is to lower the overall stiffness of the system. This suggests an interesting question: if the filaments do not go to their affine positions, where *do* they go? To begin to answer this, we consider the orientational order of our networks and compute the nematic order parameter ω, defined as

$$\omega = \langle 3\cos^2\theta - 1\rangle/2. \tag{2.16}$$

Here the average is taken over all vectors connecting crosslinks that are connected by segments of filaments and θ is the angle between such a vector and the average orientation. An isotropic network has $\omega = 0$, while a fully ordered network has $\omega = 1$. Even when we shear a network affinely, the order will increase from zero to one. To appreciate the effect non-affinity has, we should therefore compare to the affine ordering. This affine ordering is represented by the solid line in figure 2.10b. The dotted lines show the effect of non-affine reorientations on the ordering of the network, for different filament lengths. Interestingly, non-affine reorientations tend to increase the order in the network, a behavior independent of ℓ_{p}.

To get insight in the direction of the ordering, we plot the distribution of the angle ϕ of the end-to-end vectors of segments with respect to the x-axis at $\gamma = 0.7$, as shown in figure 2.10c. By comparing the distribution in a non-affine network deformation (straight bars) with the distribution of an affine network deformation (dotted bars) we see that the non-affinity increases the number of segments oriented at a small angle. To appreciate the differences in the two distributions, we plot the analytic expression for the distribution of an initial isotropic medium that is sheared affinely. Interestingly, the maximum of $P(\phi)$ coincides with the maximal extensional strain experienced as a function of angle. As the figure clearly shows, the additional ordering is in the direction of maximal extensional strain. This might seem counterintuitive - the order appears to be increasing in the direction of increasing filament extensional strain, which would be highly unfavorable from an energetic point of view. However, one should keep in mind that non-affine motions are not purely rotational: they may encompass additional and simultaneous overall shifts and extensional/compressional components. When taking a closer look at figures 1.7 and 1.8 we see that this increased ordering in the direction of maximal shear is also present in these small networks. It would be most interesting to see if this increased order is also observed in experiments. Our simulations suggest that systems containing long filaments are the best place to look for this effect, even though these tend to display lower overall non-affinity.

So far, we have considered only the non-affine motion of single points. The non-affinity correlation function is not only a function of strain, it may also be evaluated for spatially separated points $\boldsymbol{x}$ and $\boldsymbol{x}'$. To this end, we consider

$$\delta N(r) = \langle(\vec{r} - \vec{r}_{\mathrm{aff}})^2\rangle_r/\delta\gamma^2, \tag{2.17}$$

where $\vec{r}$ is the actual vector between two crosslinks and $\vec{r}_{\mathrm{aff}}$ is the vector between the

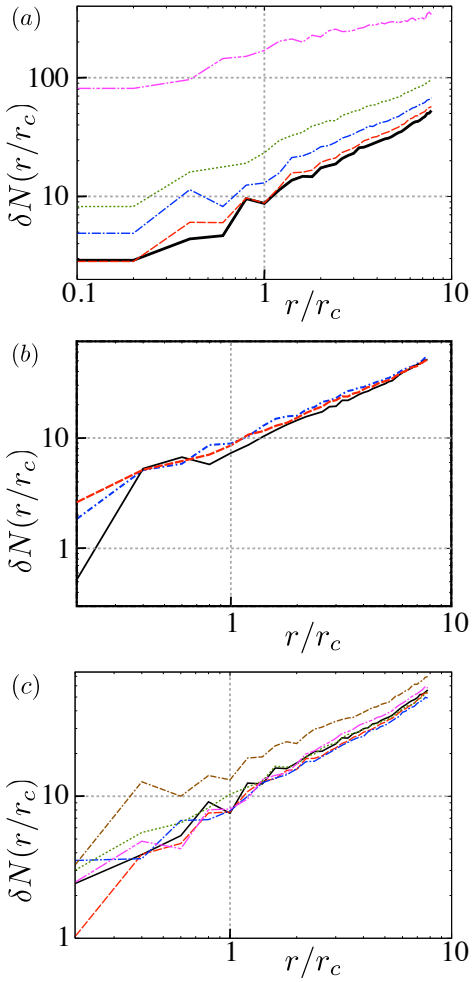


Figure 2.11: The correlation in non-affine behavior. a) Correlation of non-affine behavior of points at distance r, i.e. $\delta N(r/r_c)$ vs. r/r_c at different strains γ. The curves show respectively (from bottom to top): $\gamma = 0.0$ ($K = K_0$), $\gamma = 0.2$ ($K = 4.0K_0$), $\gamma = 0.25$ ($K = 7.6K_0$), $\gamma = 0.29$ ($K = 25K_0$) and $\gamma = 0.33$ ($K = 260K_0$). Here r_c is the average distance between crosslinks. b) $\delta N(r)$ for networks with different ℓ_p/ℓ_c (straight line: $\ell_p/\ell_c = 0.77$, stripe-dot-stripe line: $\ell_p/\ell_c = 3.81$ and striped line: $\ell_p/\ell_c = 15.7$). For all networks, $L/\ell_c = 6$. c) $\delta N(r)$ for networks with different L/ℓ_c, ranging from 20 to 4. All curves collapse except the curve for $L/\ell_c = 4$ (stripe-dot-stripe line in brown). For all networks, $\ell_p/\ell_c = 15.7$.

crosslinks if they would have moved affine during $\delta\gamma$. The average, now, runs over all pairs of crosslinks whose separation is r.

As explained in reference [19], there are two limiting cases in the behavior of $\delta N(r)$. If filaments would be stiff rods, the only way to adapt to strain would be by rotating the whole filament. In that case, doubling r would double $\vec{r} - \vec{r}_{\text{aff}}$ and thus $\delta N(r) \sim r^2$. In the other limiting case, segments along a filament behave totally uncorrelated, leading to $\delta N(r) \sim r^0$. The latter is also the limit for $r \to \infty$. However, the net effect of correlated motion of segments along a filament will be highly sensitive to the actual network configuration.

Figure 2.11a shows $\delta N(r)$ of a network at different strains. Note that the larger scatter for small values of r is due to the smaller number of pairs of crosslinks. As can be seen, $\delta N(r)$ varies with strain: low strains give a low initial value of $\delta N(r)$ and a steep increase while high strains show just the opposite. This behavior is strongly correlated to the stiffening behavior shown in figure 2.5a (upper line). The observed strain-dependence of $\delta N(r)$ is indiscernible when normalizing with respect to γ rather than of $\delta\gamma$, which might explain why experiments report no strain-dependence [19].

We observe a small but systematic dependence on ℓ_{p}, as shown in figure 2.11b. Interestingly, thus far we hardly observe any length dependence of the correlation in non-affine behavior, which is shown in figure 2.11c for networks with $\ell_{\text{p}}/\ell_{\text{c}} = 15.7$. For filaments with $\ell_{\text{p}} > \ell_{\text{c}}$, one would naively expect that the behavior of segments along a filament will be much more correlated than the behavior of segments belonging to different filaments. Thus, one might expect to find increasing spatial correlations for systems composed of larger filaments. That we do not see this behavior suggests that it is approximately balanced by another effect: larger filaments have more links to the rest of the system and are therefore more constrained. While the individual segments along a single filament would like to line up, they become increasingly unable to do so. Interestingly, the first experiments to measure $\delta N(r)$ do show a length dependence [19]. We cannot rule out that we will see this behavior at larger system sizes, but for now are unable to reproduce it.

2.3.3 Collective rearrangements

A closer look at figure 2.5b reveals some outliers in the K vs. γ curve. These discontinuities in K are accompanied by an increase in A. This is not a glitch, but rather reflects an interesting microscopic aspect of our networks. To understand this behavior we look at the displacements of individual segments during shearing. Figure 2.12 shows a network in which the thickness of the segments indicates their displacement during a strain increment of 0.2%. Here we see what happens: during such a strain increment, a significant fraction of the segments has a relatively large incremental displacement in comparison with the average displacement of segments during shear increments.

The noteworthy feature is not so much that there are large displacements, but rather that these displacements are localized and occur in correlated fashion. This is

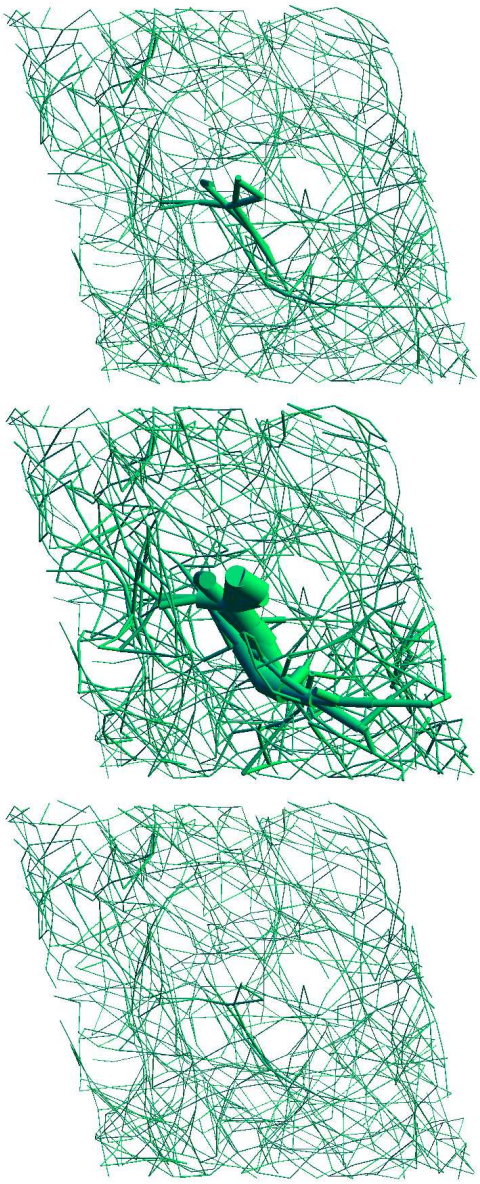


Figure 2.12: Illustration of the collective reorientations in one of our networks with $\ell_p/\ell_c = 15.7$ and $L/\ell_c = 6$ during deformation at respectively (from top to bottom) $\gamma = 0.268$, $\gamma = 0.270$ and $\gamma = 0.272$. The thickness of the segments indicates the size of their displacement. The modulus K belonging to the deformation of this network is shown as the upper curve in the inset in figure 2.5a.

reminiscent of the behavior of so-called collectively rearranging regions, observed in simulation and experiment in glassy systems and colloidal suspensions. These events are rare over the time courses that we have simulated, but may turn out to play an important role in the long-time behavior of these materials. It would be most interesting to check whether these events are also seen in experiments - while these may not be able to resolve the blip in K they might be able to register the accompanying peaks in A. The weight in determining A of a reorientation of a certain size decreases with increasing γ, since A measures the total non-affinity relative to the total shear. This implies that for small shears, reorientations might induce huge peaks in A, while these peaks are absent for larger shears even though the reorientations are still present.

2.4 Conclusions

We have presented a new method to generate and deform 3D networks of biopolymer filaments. By an adequate choice of energies both the entropic stiffness of individual segments as well as the persistence of filaments through crosslinks can be taken into account. By a Monte Carlo thermalization the networks find a local minimum, without further interference from our side.

This method enables us to relate the macroscopic network response to microscopic behavior of individual segments and crosslinks, both at small and large strains. Although a quantitative comparison between experiments and our simulations is hard to obtain, the first results from these simulations agree well with experiments. Both the stiffening during shearing and the length-dependency of the non-affinity are as expected and fit well into the general framework of the behavior of semiflexible polymers. Besides, the stress-dependence of the stiffness for large shears is the same as experiments have shown. This confirms that our model captures the right features that decide the network behavior.

Our model proves and excellent tool to compare affine deformations with deformations that allow for non-affine displacements. We have shown that non-affine displacements have a large influence on the stiffness of a network and the onset of stiffening. This accounts for the important role of filament length. Besides, the accuracy of analysis of the behavior of the filaments during deformation reveals some surprising results that are hard to obtain by experimental analysis. Thus far unobserved, the non-affinity increases the order in the networks.

Thus far we have only considered networks of a single type of filaments. Both in cells and in the extracellular matrix, the important load-bearing biopolymer networks are made up of different kinds of filaments: vessel walls are composed of collagen and elastin, and the cytoskeleton too is a composite system containing f-actin, intermediate filaments and microtubules. This method is a promising tool to explore the behavior of such composite networks under strain, as we will show in the following chapter.

CHAPTER 3

DEFORMATION OF COMPOSITE NETWORKS

Inspired by the ubiquity of composite filamentous networks in nature we investigate models of biopolymer networks that consist of interconnected floppy and stiff filaments. Numerical simulations carried out in three dimensions allow us to explore the microscopic partitioning of stresses and strains between the stiff and floppy fractions c_s and c_f, and reveal a non-trivial relationship between the mechanical behavior and the relative fraction of stiff polymer: when there are few stiff polymers, non-percolated stiff "inclusions" are protected from large deformations by an encompassing floppy matrix, while at higher fractions of stiff material the stiff network is independently percolated and dominates the mechanical response.

3.1 Introduction

The basic design of most structural biological materials is that of a crosslinked meshwork of semiflexible protein polymers. As discussed in chapter 1, the mechanical properties of these biomaterials are biologically highly significant [44, 45]. Understanding these properties at the bulk or continuous level is not sufficient: biological entities like cells, motor- and sensing proteins experience, manipulate and interact with these polymer networks at single-filament lengthscales and are therefore intimately aware of the discrete nature of these materials. Another complication arises when considering that most structural biomaterials are in fact composites: bi- or polydisperse mixtures of different protein polymers. The extracellular matrix (ECM) consists of a mixture of stiff collagen and flexible elastin filament (bundles), and the relative abundance of these two greatly affects mechanical properties [46]. A more specific example that derives much of its biological function from the side-by-side deployment of mechanically vastly different filaments is articular cartilage - a complex, partially orded composite containing type-II collagen and proteoglycans as its main structural components [47]. Composite physics may be at play in single-component networks: coexistent and interlinked single fibers and fiber bundles determine the mechanical properties of actin gels and actin-filamin networks [48, 49]. The interplay between stiff and floppy elements goes far beyond simple property mixing: The network of relatively floppy f-actin and intermediate filaments is believed to be nonlinearly stiffened by the rigid microtubules, and experiments have hinted at significant tensional forces in the cellular actin [50, 51]. The cell cytoskeleton, that is built up from microtubules, actin filaments and intermediate filaments, is yet another striking example of a composite network.

Significant effort has been devoted to model systems of homogeneous and isotropic *single-component* networks of biopolymers, such as f-actin and collagen [15, 16, 27, 34–36, 52–54]. We explained in the introductory chapter that the single filaments that constitute these networks can be described by the semiflexible wormlike chain force-extension curve, where extension requires that thermal fluctuations of the filaments be suppressed leading to a steep and nonlinear increase in the force. Compression requires considerably smaller forces that become constant in the Euler buckling limit [15, 27]. Networks of such filaments show highly nonlinear strain-stiffening and negative normal forces under shear [16,52,55]. Recent theoretical studies and simulations have also underlined the importance of non-affine bending deformations in these networks [34–36, 54], see also chapter 2. Models applying a similar method to composite biomaterials have only recently begun to emerge [56, 57] and have focused on bulk behavior.

In this chapter, we report the results of a series of numerical experiments of *two-component* networks of biopolymers to determine the relationship between composition and mechanical properties, both on the single-filament as well as on the bulk level. Furthermore, we compare our results to a theoretical model.

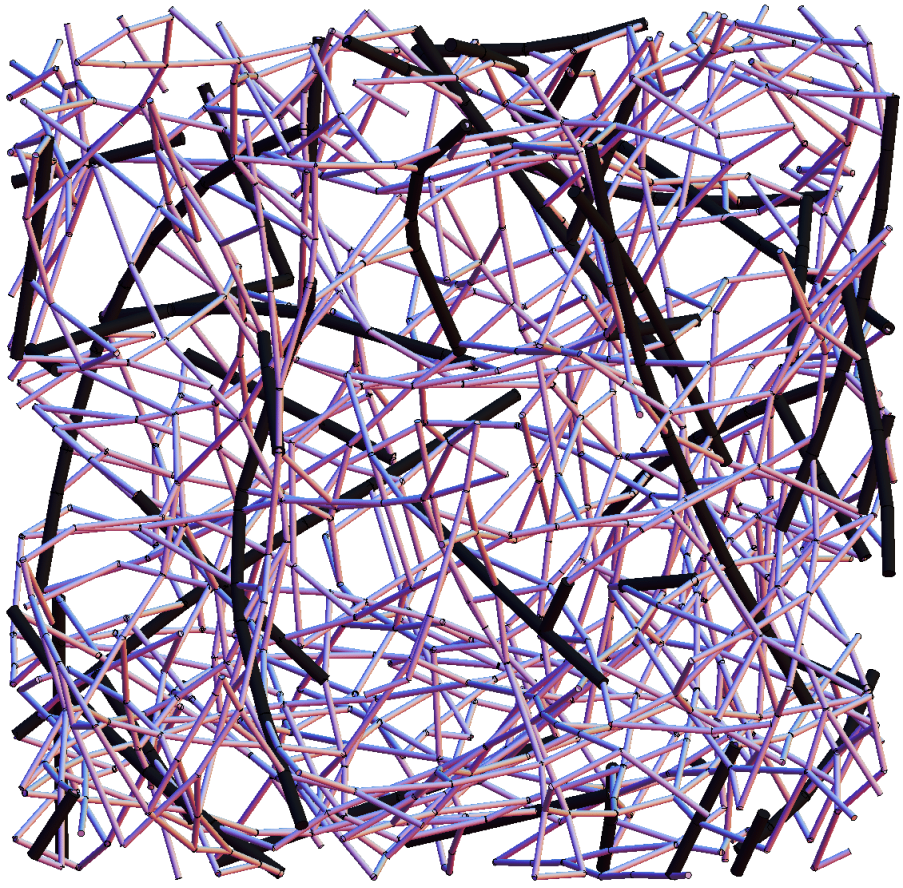


Figure 3.1: Illustration of a composite networks with a fraction $c_s = 0.23$ of stiff filaments. The dark, thick beams indicate stiff filaments, the purply, thin beams are floppy filaments. All filaments are connected and form one network.

3.2 Setup of the numerical simulations

We slightly alter the generation method presented in chapter 2 to generate composite networks. Our networks consist of long filaments that are permanently crosslinked. These crosslinks force a binary bond between two filaments, without angular preferences. The filaments are described by the semiflexible wormlike chain model [15,27]. Starting from a random, isotropic network consisting of crosslinks and segments, we apply a large number of Monte Carlo moves which alter the network topology such that filaments with a persistent directionality along segments are formed. At this point, we designate filaments to be either stiff or floppy by assigning to each segment a persistence length and an equilibrium backbone length. We then further relax the configuration by applying new Monte Carlo moves. All our networks have periodic boundary conditions and contain 1,000 crosslinks. Their lateral sizes are determined by the condition of zero pressure. Our networks are characterized by the following set of parameters: the persistence length ℓ_{p} of the stiff filaments, the stiffness ratio $R_p = \ell_{\mathrm{p}}/\ell_{\mathrm{p,floppy}}$, the average filament length L, the average distance between crosslinks along a polymer's backbone ℓ_{c} and finally the relative fraction of stiff filaments c_{s}. In this chapter, we examine the c_{s}-dependence of the mechanical behavior. We restrict ourselves to a biologically relevant region of parameter space: the persistence length $\ell_{\mathrm{p,floppy}}$ of the floppy filaments and the crosslink distance ℓ_{c} are of comparable magnitude. On average, each filament is crosslinked six times ($L = 6\ell_{\mathrm{c}}$). The ratio of the persistence lengths of stiff and floppy filaments R_p is chosen to be 16 or 64. While this ratio is smaller than that for collagen/elastin ($R_p \approx 100$) [46] or microtubules/f-actin ($R_p > 200$) [58], it is large enough to capture the qualitative behavior of such composite networks. Unless otherwise stated, all data shown represent the averages of nine network realizations.

3.3 Results

Our key findings are summarized in Figs. 3.2 and 3.3. In figure 3.2 we plot a 50/50 composite: rather than averaged, the mechanical behavior is bimodal – approaching the fully floppy system at low strains but, at finite strains, resembling the fully stiff network. We stress that this type of response can only be achieved in a composite. Even the linear behavior does not interpolate simply between stiff and floppy: figure 3.3a shows that at low to intermediate c_{s}, the modulus is quite insensitive to c_{s}, but rises very quickly at higher c_{s}. Figure 3.3b, finally, reinforces the point of figure 3.2: although the effects of adding stiff polymer are hardly noticeable in the linear elastic behavior, their effect on the nonlinear behavior is felt much earlier. The critical strain (γ_c) for the onset of the nonlinear regime reacts immediately to the addition of stiff material, but saturates at a point roughly coincident with the rise of the linear modulus.

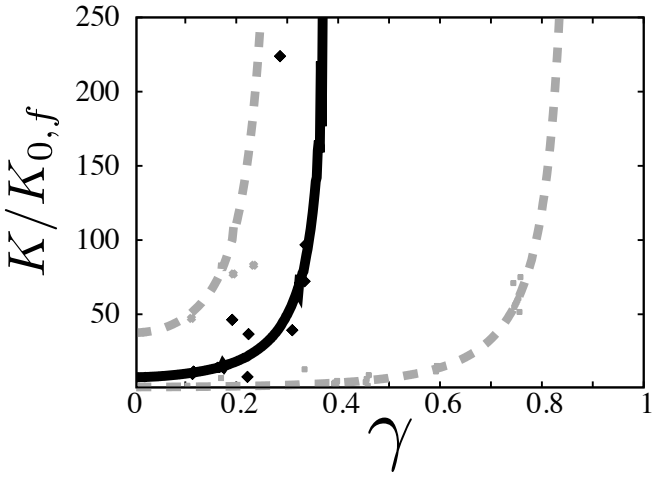


Figure 3.2: Macroscopic properties of the networks as a function of the fraction c_s of stiff filaments in a network. Shear modulus K as a function of shear γ, normalized by the initial shear modulus $K_{0,f}$ of single-component networks of floppy filaments. The different curves represent the stiffness of networks with $c_s = 0.0, 0.56, 1.0$ (from bottom to top), at a fixed persistence length ratio $R_p = 16$. Some data points (< 1%) lie well outside the curve; these are indicated by the symbols. These outliers occur due to local reorientations, see section 2.3.3.

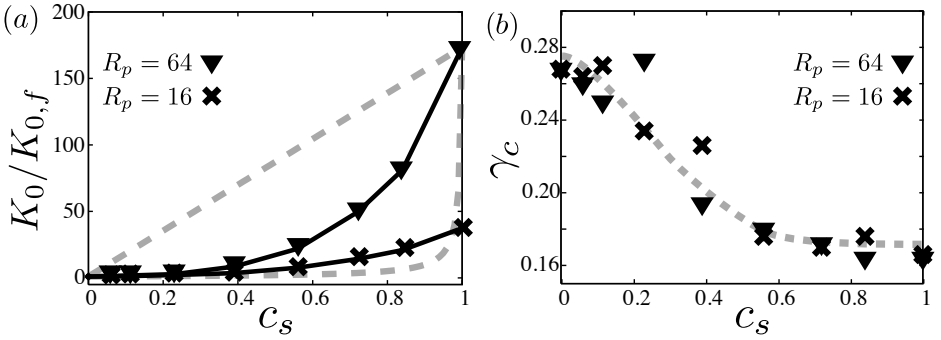


Figure 3.3: Macroscopic properties of the networks as a function of the fraction c_s of stiff filaments in a network. (a) The normalized initial shear modulus as a function of c_s, for networks with $R_p = 64$ and 16. For comparison, we also plot curves corresponding to a linear scaling of the shear modulus with c_s, given by $K_0(c_s) = c_s K_{0,s} + (1 - c_s)K_{0,f}$, and a linear scaling of the compliance with c_s, given by $1/K_0(c_s) = c_s/K_{0,s} + (1-c_s)/K_{0,f}$. (b) Critical shear γ_c, defined as the shear at which the shear modulus is twice the initial shear modulus, as a function of c_s. The curve is drawn as a guide to the eye.

3.3.1 Composites at low fraction of stiff filaments

The qualitative picture that emerges at small c_s is one of a floppy matrix encompassing isolated stiff filaments, or non-percolated clusters. Intuitively, the initial insensitivity of the linear modulus K_0 to the addition of stiff material makes sense: deforming the stiff filaments requires higher energies than deforming the softer elements, and therefore the low-energy modes of the system favor straining the floppy elements over the stiff ones. As long as stiff filaments do not form an independently load-bearing subnetwork, these low-energy modes exist and are compatible with the bulk deformation.

This interpretation is confirmed by an examination of the microscopic deformation field, characterized by the non-affinity parameter $A = \langle|\mathbf{x}_{\text{aff}} - \mathbf{x}|^2\rangle/\gamma^2$ (figure 3.4a). This parameter quantifies the deviation of the local deformations, $\mathbf{x}$, from a homogeneous affine deformation field, $\mathbf{x}_{\text{aff}}$. As shown in chapter 2 and in experiments [20], the non-affinity generally increases with increased stiffness of the filaments, as bending deformations are more important for the network response of stiffer filaments. Indeed we find that the non-affinity is minimal for purely floppy networks and rises roughly linearly with the addition of stiff material. Such a linear increase represents the generic behavior of low-density (stiff) inclusions that independently perturb the deformation field of their surrounding (floppy) matrix [59]. These additional non-affine deformations bring the floppy filaments closer to the nonlinear part of their force-extension relation, giving rise to the decrease of the critical strain γ_c as dis-

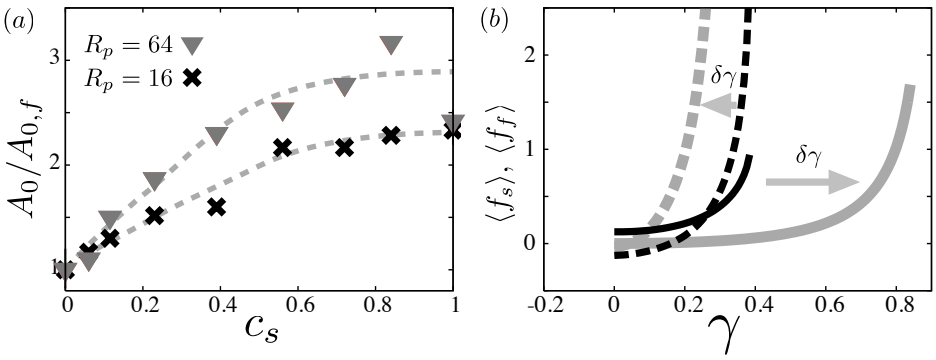


Figure 3.4: (a) The non-affinity at zero shear, divided by the initial non-affinity of a network with $c_s = 0$. The curves are drawn as guides to the eye. (b) Average forces in the floppy and stiff filaments during deformation, shown by the solid and dotted curves, respectively. The black curves represent the average force of a network with $c_s = 0.56$ during shear. For comparison, we plot the average forces in single-component networks, $c_s = 1.0$ and $c_s = 0.0$ (grey curves). As indicated by the arrows, the curves for the average forces in the composite networks are shifted along γ with respect to the curves for the single-component network.

played in figure 3.3b.

In the nonlinear regime the inherent stiffening of a single semiflexible polymer makes the distinction between floppy and stiff fractions highly strain-dependent, with the ratio of their nonlinear moduli tending to unity in the high strain limit. This suggests a self-matching behavior at finite strain: the floppy network stiffens up to the point where its modulus matches that of the stiff network. Beyond this point, the entire meshwork behaves as a nearly monodisperse system of stiff filaments. This effect is the origin of the behavior in figure 3.2: at high strains, the entire system is ultimately forced to couple to the stiffer deformation modes.

This mechanism of stiffness matching is illustrated in figure 3.4b which shows the average forces in the stiff and floppy filaments during deformation. By comparing with the one-component networks (grey lines) we can define a strain shift $\delta\gamma$: For given network strain γ, the filaments in the composite behave as if they were strained up to $\gamma + \delta\gamma$. Apparently, the effective strain on the floppy filaments is much larger than that on the stiff filaments. Equivalently, high forces in stiff filaments are suppressed, at the cost of increased forces in floppy filaments.

Interestingly, this load-partitioning persists even at *zero strain*, where stiff filaments are, on average, compressed while floppy filaments are stretched out. This stretched/compressed ground state is tantalizingly reminiscent of tensegrity states [50, 60]. Apparently, dense crosslinking restricts relaxation of the network, and the absolute minimum of mechanical energy cannot be attained. There is, there-

fore, always a finite amount of residual elastic energy. This suggests that such force distributions may not be a deliberate design principle but rather are the necessary byproduct of polydispersity in filamentous composites.

3.3.2 Percolation

The picture of a floppy matrix embedding stiffer inclusions breaks down when the stiff filaments become independently rigidity percolated: the point where deformation of the stiff elements becomes inevitable. We may estimate the percolation threshold by a counting argument [61]. Equating the number of degrees of freedom of the stiff filaments to the number of constraints due to crosslinks between stiff filaments gives (for $L/\ell_c = 6$) a threshold $c_s = 0.56$. This marks the transition from the low to the high c_s regime and coincides roughly with the rise in the linear modulus K_0 (figure 3.3a). Two separate obervations confirm the onset of stiff dominance: Firstly, $c_s = 0.56$ is the point at which the non-affinity, which we attribute to the floppy matrix attempting to work around the stiff fraction, begins to plateau at the level of the bending dominated response of a purely stiff network. Secondly, the critical strain γ_c levels off around this same value of c_s. In the range of stiffness ratios (R_p) accessible to the simulations the percolation is rather "soft" and represents a smooth crossover phenomenon. The approach towards the singular percolation limit, $R_p = \infty$, has for example been studied in simulations of mixed random resistor networks [62]. To address the analogous problem we compare our results with theoretical considerations, in which the parameter R_p can be tuned to arbitrarily large values. The "floppy-mode" theory [36] has recently been shown to capture quite well the elasticity in one-component isotropic [24, 63, 64] as well as anisotropic networks [65]. Within this theoretical framework the calculation of the network elastic modulus is reduced to the description of a "test" filament in an array of pinning sites. The coupling strength to these sites, k, represents the elastic modulus of the network and has to be calculated self-consistently. To generalize this model to the case of composite networks we use two different test chains with coupling parameters k_f and k_s, representing floppy and stiff filaments, respectively, see [66] for details of the calculation. The use of two different coupling strengths quite naturally takes into account the load partitioning encountered in the simulations. The network modulus, $k = c_s k_s + (1 - c_s) k_f$, is obtained by solving the two equations

$$k_{f/s} \simeq \left\langle \min_y \left(W_b^{f/s}\left[y(s)\right] + \frac{1}{2}\sum_{i=1}^{n} k_{\alpha_i}\left(y(s_i) - \bar{y}_i\right)^2 \right) \right\rangle , \tag{3.1}$$

where $k_{\alpha_i} = k_s, k_f$ with probability c_s and $1 - c_s$, respectively. The two energy contributions on the rhs of equation (3.1) reflect the competition between the bending energy of the (floppy or stiff) filament, $W_b^{f/s}$, and the energy due to deformation of the surrounding medium by displacing the pinning sites (located at arclength position s_i along the filament). The nonlinear entropic stretching elasticity is not included in these equations. The minimization is to be performed over the contour of

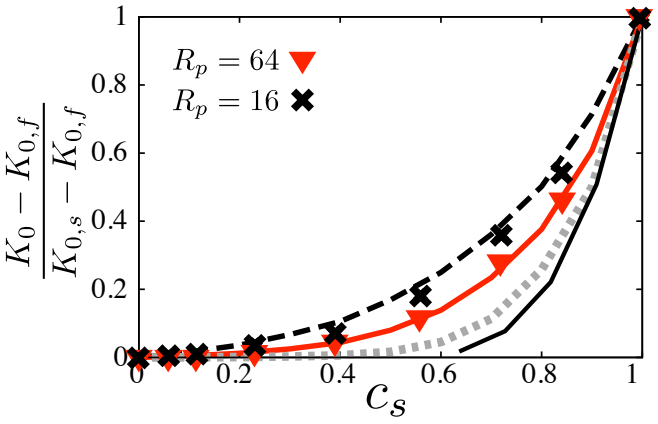


Figure 3.5: The scaled initial stiffness as a function of c_s, obtained by the floppy-mode model for $R_p = 16, 64, 1000, \infty$ (from top to bottom). For comparison, the data from simulations are given by the symbols.

the filament, $y(s)$, the angular brackets specify the disorder average over the network structure.

Figure 3.5 displays the results from this calculation for various stiffness ratios R_p, showing a sharp percolation transition in the limit $R_p \to \infty$. The model compares well with the simulation data, even though the entropic stretching elasticity is not accounted for. This indicates that bending is likely the dominant factor in determining the rise of the linear elastic modulus, in agreement with the proposed mechanism of load-partitioning and the observed increase of the non-affinity.

3.4 Conclusions

In conclusion, our results demonstrate that the mechanical behavior of filamentous composites is considerably richer than the simple proportional mixing of properties. The fact that the floppy and stiff networks are physically linked causes a strongly nonlinear coupling between the strain fields which deeply affects composite mechanics. This may explain the ubiquity of composites in structural biological applications: slight variations in composition cause large changes in mechanical behavior. This high susceptibility makes the composite architecture an attractive motif for biological regulation. Likewise, the "best of both worlds" aspect may be exploited by Nature: composites combine the initial softness of their most compliant components with the ultimate toughness of the stiffest elements. This greatly enhances the stiffness range of nonlinearly elastic materials. Moreover, composites do so in a manner that could never be attained in monodisperse materials, since linear and nonlinear prop-

erties of composites are determined by two physically different materials and therefore may be independently varied. This possibility of independently tuning the linear and nonlinear behavior also has considerable potential for the design of biomimetic or bio-inspired synthetic materials and deserves further exploration.

While exploring the physics of composite networks, we are faced with the fact that internal stresses, percolation and floppy modes are important for the characterization of our networks. This raises questions on the presence and impact of internal stresses in networks, the ridigly percolation transition and the occurence and characteristics of floppy modes. In the next chapter we will therefore return to single-component networks and adress these issues.

Chapter 4

Internal stresses, normal modes and non-affinity of networks

We numerically investigate deformations and normal modes of three-dimensional networks of semiflexible biopolymers as a function of average crosslink coordination number z and relative strength of bending and stretching energies. Our networks consist of filaments that in equilibrium are in a state of internal stress, and they exhibit shear rigidity below the Maxwell isostatic point. In contrast to two-dimensional networks, ours exhibit nonaffine bending-dominated response in all rigid states, including those approaching the maximum of $z = 4$ as long as bending energies are smaller than stretching ones.

4.1 Introduction

As discussed in introductory chapter, networks of semiflexible biopolymers [4, 7, 16, 67] are important for determining and controlling the mechanical properties of eukaryotic cells. Understanding their properties, in particular the relation between mechanical response and network architecture, has been a major goal of biophysics research. Networks of semiflexible biopolymers consist of long filaments of average length L linked two at a time by crosslinks so that each is connected to at most four others [15, 27, 32, 35, 68]. The crosslinks we consider, which we will refer to as nodes, allow free rotations of filaments relative to each other. They divide the filaments into a series of segments, of average length ℓ_c, that give rise to a central force between nodes determined by the force-extension curve of a semiflexible polymer. In addition, bending forces favor parallel alignment of contiguous segments on the same filament meeting at a common node. As shown in chapter 2, the mechanical properties of networks of semiflexible biopolymers depend on their connectivity, parameterized by the average coordination number z of their nodes or by the ratio L/ℓ_c, on their interaction parameters, and on their architecture.

Networks of semiflexible polymers have much in common with those that occur in network glasses [69–71]. They are both continuous random networks [72]; they both have nodes with maximum coordination number 4; and they are both stabilized below the central-force rigidity threshold by bending forces, between all bonds in the latter but only between segments in the same filament in the former. Careful mode counting and study of the mode structure of network glasses [69–71] and other random systems such as hard spheres near the jamming transition [73–75] have provided fundamental insight into the physics of these systems. They have also been used in the study of two dimensional networks of semiflexible biopolymers [23, 36]. In this chapter, we undertake a similar study of simulated three-dimensional networks of semiflexible biopolymers [54] as a function of their connectivity and interaction parameters, and we analyze the zero-frequency shear modulus and the mode structure as a function of these parameters.

4.2 Maxwell counting

A system of nodes and links in d dimensions has a trivial set of zero-frequency modes of rigid translations and rotations. If the system has additional internal zero-frequency “floppy" modes [70], it is mechanically unstable, though it is often stable with respect to macroscopic stress. As Maxwell [76] first showed, in an unstressed system a global estimate of the number of floppy modes N_0 can be calculated by subtracting the number of constraints N_c from the number of degrees of freedom, $N_0 = dN - N_c$ (neglecting the sub-extensive trivial zero modes), where N is the number of nodes. In the following we consider the forces as constraints. We define N_k as the number of nodes on filament k and N_F as the number of filaments, and in our simulations we explicitly remove all disconnected clusters and all filaments with

$N_k = 0$ and $N_k = 1$. Each node is shared by exactly two filaments, and $N = \frac{1}{2}\sum N_k$. In our system, each of the $N_k - 1$ segments on a filament provides one constraint for a total of $N_s = \sum_{k>1}(N_k - 1) = 2N - N_F$ compressional constraints. Because segments on a single filament that meet at a common node are not parallel in our system, each of the $N_k - 2$ nodes on filament k not connected to a dangling end contributes a single constraint for a total of $N_b = \sum_{k>1}(N_k - 2) = 2N - 2N_F$ bending constraints. Thus, $N_0 = dN - N_s - N_b = 3N_F - (4-d)N$. We define the average coordination $z \equiv 2N_s/N$. Then $N_F/N = 2 - (z/2)$, $N_0 = N[2 + d - (3/2)z]$, and the critical coordination number below which floppy modes first appears is $z_c = (2/3)(2+d)$. In $2d$ $z_c = 8/3$, and in $3d$, $z_c = 10/3$, a value that, as expected, is greater than the value $12/5$ in $3d$ network glasses [70]. It is common practice to characterize networks of semiflexible biopolymers by L/ℓ_c rather than by z. In our case, dangling ends each contribute an average of $\ell_c/2$ to the length of a segment. Thus L/ℓ_c is equal to the number of nodes per polymer, $\sum_k N_k/N_F = 2N/N_F = (1 - \frac{1}{4}z)^{-1}$, and $(L/\ell_c)_c = 6$ in $3d$.

4.3 Network model

As explained in the former chapters, we do not represent all monomers explicitly but rather integrate out all degrees of freedom of the polymers between nodes. Since we consider the small-strain behavior of the filaments, we use the linear approximation to the nonlinear force-extension curve of semiflexible polymers, instead of the full nonlinear force-extension curve presented in chapter 2. Our Hamiltonian is thus a sum over all segment free energies and over all bending energies of pairs of segments that are connected along a filament, resulting in:

$$\frac{E}{k_B T} = \sum_i \frac{\ell_p^2}{\ell_{c,i}^4}(r_i - r_{0,i})^2 + \beta \sum_{i,j} \frac{\ell_p}{\ell_{c,i} + \ell_{c,j}} \theta_{i,j}^2, \tag{4.1}$$

where ℓ_p is the persistence length of the filaments, $\ell_{c,i}$, r_i and $r_{0,i}$ are respectively the polymer length, the end-to-end length and the equilibrium end-to-end length of segment i, and $\theta_{i,j}$ is the angle between segment i and j.

We construct our networks via a Monte Carlo relaxation process. We start with a random, isotropic network that can be considered as a single filament that crosses itself one thousand times [54]. After a large number of Monte Carlo moves that alter the topology of the network, we cut segments of this filament, until we obtain an average filament length L. In the work presented in chapter 2 we designate a polymer lengths to each segment that is drawn from the corresponding distribution for the WLC with the desired persistence length. Here, we assign a polymer length ℓ_c^s to each segment such that the equilibrium end-to-end length of each segment is equal to the actual distance between the nodes they connect, and we do not apply length-changing Monte Carlo moves as illustrated in figure 2.3c. After generation, the network is in equilibrium, but the filaments are slightly bent - $\theta_{i,j} \neq 0$ - and, as a result, there are internal stresses in the system. For all networks, during generation we keep

$l_c = \sum_s l_c^s / N_s$, l_p and β fixed, such that $l_p/l_c \approx 16$ and $\beta = 1.0$. l_p is a measure for the relative stiffness of bending versus stretching. In order to isolate the effects of bending and stretching without altering the network structure and contour lengths, we vary β. We could, however, vary l_p at constant l_c to produce the same effect. Letting $l_p \to \beta^{-1} l_p^0$, where l_p^0 is the value of l_p at $\beta = 1$ reproduces Eq. (4.1) with energy measured in unit of $\beta^2 k_B T$. Thus with $l_p^0/l_c = 16$, $\beta = 10.0$ coincides with $l_p/l_c = 1.6$ and $\beta = 0.1$ with $l_p/l_c = 160$. In addition we vary L - and thus the average number of nodes per filament L/l_c - by changing the number of segments we cut. Finally we focus on an experimentally relevant parameter space, with networks with on average 4, 5, 6, 8, 12 and 20 nodes per filament or equivalently with coordination number $z = 3.0$, 3.2, 3.33, 3.5, 3.66 and 3.8. In real-life networks, typical ratios between l_p and l_c coincide with values of β ranging from 0.05 (e.g. cortical actin networks [77]) to 10 (e.g. fibrin networks [15]); here we take values of β ranging from 0.0001 to 10. All data shown are averages over nine network realizations.

We calculate the dynamical matrix from the harmonic expansion of the energy about its force-free equilibrium state and use commercially available routines to find the eigenvalues and eigenmodes of the system, neglecting any damping effects arising in particular from interactions with a surrounding fluid, see also section 1.6.3. Figure 4.1 graphically represents some localized and delocalized eigenmodes.

4.4 Maxwell counting in our networks

To investigate the Maxwell mode counting in our networks, we remove the internal stresses by subtracting the zero strain angle, $\theta_{i,j,0}$, between two segments from the actual angle $\theta_{i,j}$ in our Hamiltonian. We then count the number of zero modes by calculating the dimension of the null space of the dynamical matrix, and we verify the relation $N_0 = N[5 - \frac{3}{2}z]$. We verify the stretching relation, $N_s = \sum(N_k - 1)$, by explicitly counting the number of finite-frequency modes for networks with $\beta = 0$, and thus no bending constraints. We also verify that $N_b = \sum_k (N_k - 2)$ by varying the number of nodes with non-zero bending modulus β. When internal stresses are turned back on, the floppy modes are tightened, and there are only finite-frequency modes for all z ($\geq$ 3.0) and all $\beta > 0$. Also the lengthening of a single segment in the unstressed samples generates stress in a finite fraction of the segments and elevates floppy modes to finite frequency a full 10% below the Maxwell threshold. This is comparable to the rigid "stressed" state of network glasses, that exists for z just below the Maxwell threshold of 2.4 [71].

4.5 Shear response

We calculate the relaxed shear modulus G' for networks with and without internal stresses and for a range of z and β by deforming the network by a small shear increment and minimizing the elastic energy after each shear increment. Figure 4.2

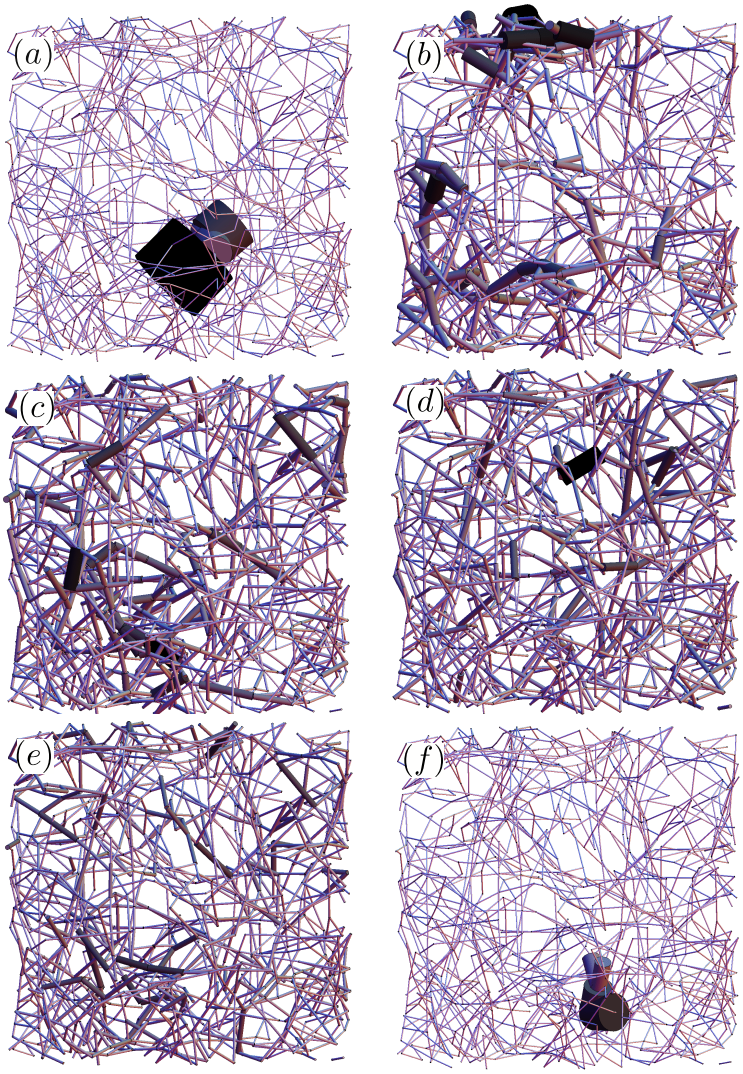


Figure 4.1: Graphical representations of some of the eigenmodes of one our network. The eigenmodes for (a) $\omega = 27$, $P^{-1} = 0.51$, (b) $\omega = 4.6$, $P^{-1} = 0.02$, (c) $\omega = 2.9$, $P^{-1} = 0.0057$, (d) $\omega = 1.4$, $P^{-1} = 0.0029$, (e) $\omega = 0.5$, $P^{-1} = 0.0053$ and (f) $\omega = 0.07$, $P^{-1} = 0.67$ are respectively shown. Here, ω is the eigenfrequency and P^{-1} is the inverse participation ratio (see the discussion of figure 4.3). All filaments in the networks are shown. Large deformations are indicated by the thick and dark beams.

summarizes our results. For all values of β, $G'(z)$ is a monotonic increasing function of z, reaching its lowest but non-zero value at $z = 3.0$, the smallest values in our simulations. As shown by the dotted curve in the inset of figure 4.2, in the unstressed networks, G' is zero to within the accuracy of our simulations for $z < z_c$ and develops a nonzero value in the vicinity of the Maxwell value of $z = z_c$, growing approximately as a power law for $z > z_c$, though we cannot rule out a first-order transition. In the stressed state our data is consistent with a second-order rigidity threshold at $z = z_p \approx 2.7 < 3.0$, though again, we cannot rule out a first-order transition. For all β, $\log(G'/\beta)$ grows linearly with $\log(z - z_p)$, where the slope is around 2.7 for $\beta = 10^{-4}$, 10^{-2} and 10^{-1} and then decreases with β to a value around 1.1 at $\beta = 10$. The fact that the slope depends upon β is not surprising, since for large β, we expect the deformation to be dominated by (affine) stretching of the segments, the number of which linearly increases with z, leading to a slope of 1. At small β, response to shear occurs preferentially through bending rather than stretching modes, and G' is more sensitive to changes in z , as reflected in the larger value of the slope. For the smallest values of β, G' becomes approximately linear in β for all values of z, which again demonstrates that bending dominates the deformation, as is the case in glasses [78].

There are many examples of structures in which external stresses can remove floppy modes. Here we show that internal stresses can have a similar effect, reminiscent of tensegrity structures, in which rigidity can be achieved below the Maxwell threshold by stressed cables and compressed struts in carefully designed configurations [79, 80]. In contrast to these configurations, our networks are *random*, and rigidity is a consequence of competition between stretching and bending rather than between stretching and compression. If the network has a structure in which filaments can support self-stress, a modified Maxwell rule $N_0 = dN - N_c + S$, where S is the number of states of self-stress [81] or, equivalently, the number of redundant bonds [82, 83], applies to the stressless state. Thus, even though global Maxwell counting would indicate the contrary, biopolymer networks with internal stresses may not have floppy modes and may support shear below the stressless Maxwell rigidity threshold.

Network geometry, co-ordination number, and spatial dimension are all important to the determination of macroscopic elastic response. Two-dimensional lattices with $z = 4$, such as the kagome lattice and the $L/\ell_c \to \infty$ limit of the Mikado lattice formed by the randomly depositing rods on a plane, are isostatic with respect to stretch, and they both exhibit affine response with non-zero shear and bulk moduli that are independent of β. The transition from non-affine bending-dominated to nearly affine stretching-dominated response observed in diluted Mikado lattices in references [32, 68, 84] is thus not surprising. Three-dimensional systems with $z = 4$ are sub-isostatic with respect to stretch, and one might expect that bending forces are required for stabilization against shear. This is indeed the case for the $z = 4$ diamond lattice, none of whose bond-angles are zero (i.e., all filaments are straight), whose shear modulus vanishes linearly with β [78]. On the other hand, a recently constructed $3d$ generalization of the kagome lattice consisting of infinitely long straight filaments with crosslink coordination of exactly four provides a counter example to

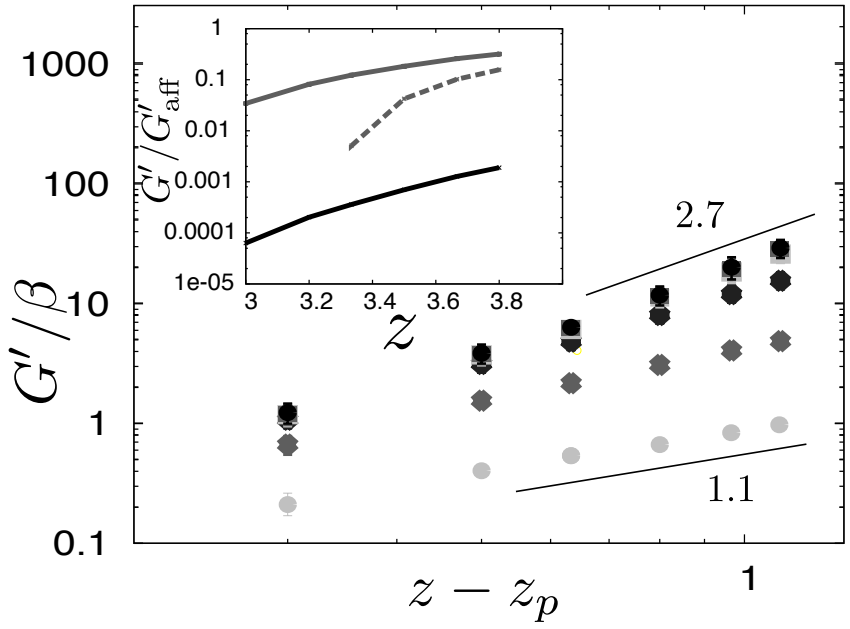


Figure 4.2: Double logorithmic plot of G'/β in networks with prestress as a function of $z - z_p$ for different values of β. Datapoints are from simulation, most errorbars are smaller than the size of the symbols. The slope of the datapoints ranges from 2.7 upper, overlapping datapoints for $\beta = 0.0001$ and $\beta = 0.001$, 2.6 ($\beta = 0.01$), 2.1 ($\beta = 0.1$), 1.5 ($\beta = 1.0$) and 1.1 ($\beta = 10.0$, lower points). A value of $G' = 1$ corresponds to an elastic modulus of ≈ 10 mPa for an actin network with a concentration f-actin of ≈ 0.05 mg/ml. Inset shows G'/G'_{aff} as a function of z, for $\beta = 1.0$ (upper curve) and $\beta = 0.001$ (lower curve). Dotted curve shows data from unstressed network, for $\beta = 1.0$.

his behavior [85]. Because all its filaments are straight it has a persistent triangular motif, all of it elastic moduli are nonzero when $\beta = 0$. As is the case in most biopolymer networks and in the diamond lattice, the filaments in our network are not straight, so we expect behavior closer to that of the diamond lattice than the to that of the straight-filament $3d$ lattice with nonaffine bending dominated response and a shear modulus that vanishes with β even in the limit $z \to 4$. Though our simulations do not reach sufficiently close to $z = 4$ to unambiguously determine behavior at $z = 4$, they provide strong evidence that this expectation is fulfilled. As the inset in figure 4.2 shows, it is highly improbable that the affine limit, $G'/G'_{\text{aff}} = 1$, is reached for small β. Instead, we find that $G' \propto \beta$ for the smallest values of β in figure 4.2, implying that G'/G'_{aff} vanishes with vanishing β.

4.6 Mode analysis

To deepen our understanding of the network response of the stressed networks, we now turn to the mode structure of these networks. The density of states $D(\omega)$ and the inverse participation ratio [75],

$$P^{-1}(\omega) = \frac{\sum_{i=1}^{N} |e_{i_\omega} \cdot e_{i_\omega}|^2}{|\sum_{i=1}^{N} e_{i_\omega} \cdot e_{i_\omega}|^2}, \tag{4.2}$$

which provides a measure of the the degree of localization of the eigenmodes, are plotted in figure 4.3. In equation (4.2), e_{i_ω} is the polarization vector of node i in the mode ω. The value for $P^{-1}(\omega)$ will be 1.0 if the mode displaces one node, 0.5 if the mode displaces two nodes, and it will be $1/N$ for the translational zero modes that are linear transformations of the whole network. The data in figure 4.3 are averaged over narrow bins of frequency. The reduced frequency ω corresponds to physical frequencies $\tilde{\omega} \approx 10^6 \omega\ s^{-1}$ for actin ($\ell_p = 16\mu m$ and $\ell_c = 1\mu m$) and $\tilde{\omega} \approx 10^5 \omega\ s^{-1}$ for fibrin bundles ($\ell_p = 33\mu m$ and $\ell_c = 2\mu m$, as analyzed in [86]). These frequencies will decrease if the viscosity of the surrounding fluid is included.

Figure 4.3a shows the density of states, $D(\omega)$ as a function of $\log\omega$ with logarithmic binning for $\beta = 0.0001, 0.01$, and 1.0 at $z = 3.33$. For $\beta = 0.01$ and $\beta = 0.0001$, there is a peak in $D(\omega)$ at $\omega \approx 2$ that corresponds to stretching modes. Its total area for $\beta = 0.0001$ is equal to the number of stretching constraints, $2N - N_F$ or equivalently to the number of non-vanishing modes at $\beta = 0$. With increasing z, the area under the right peak increases, as we would expect from the increase in the number of stretching constraints (data not shown). There is a second peak at smaller ω that moves to the left as β decreases. We verified that the total area under this peak is $N'_b = N_0 + N_b$, where N_0 is the number of zero modes of the unstressed network, and N_b is the number of bending constraints. Where possible, shear deformation will take place via these soft bending modes. As we have seen, $G \sim \beta$ for small β, which implies that this is indeed the case. Again, we average over narrow bins of frequency with fixed logarithmic width to obtain $P^{-1}(\log\ \omega)$, which is plotted in figure 4.3b for

$\beta = 0.0001$. Interestingly, both bending and stretching modes can be localized and delocalized.

Figures 4.3c and 4.3d plot $D(\omega)$ and $P^{-1}(\omega)$ for different values of z and $\beta = 1.0$. The broad distribution in P^{-1} reflects the randomness in our system. Clearly the number of soft, low-frequency modes increases with decreasing z, and these modes are less extended. At low z, the filaments are less constrained in the networks, leading to an increase in soft deformation modes in the networks; in this limit, movement of a single segment will lead to a less extended deformation field. This is reflected in the increase of P^{-1} when decreasing z. We verified that the Debye scaling is approached and the frequency at which this scaling starts decreases for decreasing z. For $z = 3.0$ and $z = 3.2$ we do not find a peak in $D(\omega)$ at $\omega = 0$, which is consistent with the given analysis that internal stresses can remove floppy modes for $z < z_c$.

4.7 Conclusions

Our results show that networks with internal stress violate stressless Maxwell counting and exhibit rigidity and no floppy modes below the Maxwell isostatic threshold. This can be relevant for in vivo biopolymer networks, that might have large internal stresses which increase the stiffnesses of the cells [7]. As $\beta \to 0$, there is a clean separation between low-frequency bending modes and high-frequency stretching modes. As is the case in most *real life* biopolymer networks but contrary to that of most biopolymer networks studied analytically and in simulations, our networks consist of bent filaments. Our simulations show that it is highly improbable for this class of networks that the affine limit is reached for z approaching 4 at small β. Instead, the networks deform via low-frequency bending modes. Further investigation of this model, including a more thorough comparison with network glasses and a pebble-game analysis [82] to locate the critical point and to determine its order, would clearly be interesting.

As mentioned in section 4.3, thus far we neglect any damping effects arising in particular from interactions with a surrounding fluid. Real life biopolymer networks are always surrounded by a fluid. In the following chapter we expand our model and incorporate the thermal motion and the viscous drag experienced by the filaments in the networks. This method allows us to calculate the frequency-dependence of the network response.

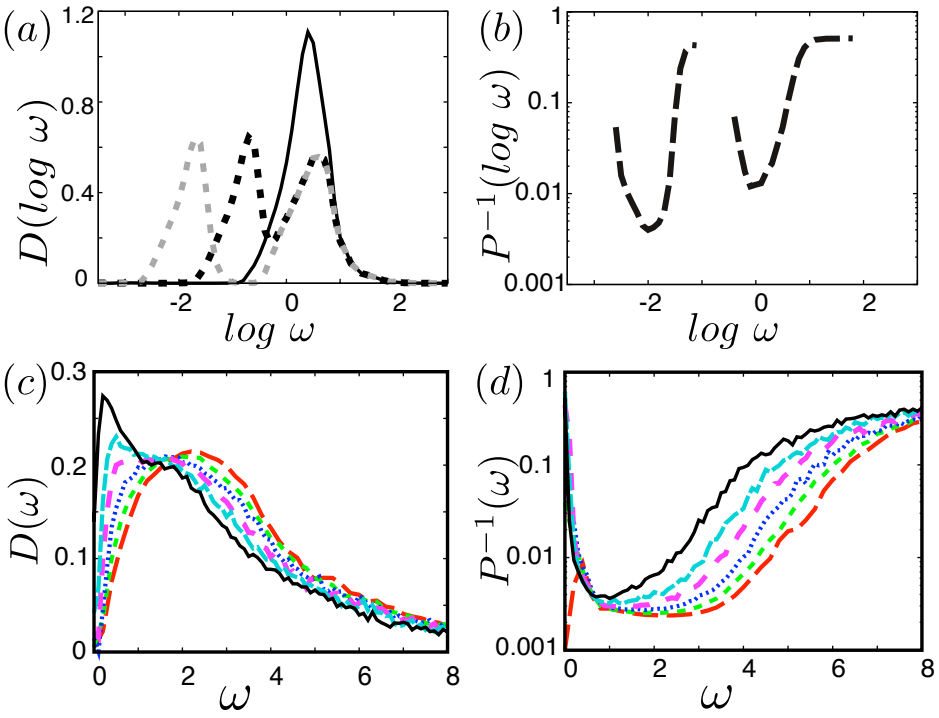


Figure 4.3: a) The logarithm of the density of states, for $\beta = 1.0$ (solid curve), $\beta = 0.01$ (black dotted) and $\beta = 0.0001$ (grey dotted) for networks with $z = 3.33$. Note that the right peak of the latter two curves overlaps, and the left peak is shifted. b) The inverse participation ratio for $\beta = 0.0001$, again for $z = 3.33$. c) The density of states and d) the inverse participation ratio as a function of z. All data shown are for networks with $\beta = 1.0$ and (starting from the solid line) $z = 3.0$, $z = 3.2$, $z = 3.33$, $z = 3.5$,$z = 3.66$ and $z = 3.8$. Data shown are averaged over narrow bins of (the logarithm of) frequency.

CHAPTER 5

FREQUENCY-DEPENDENT RESPONSE OF NETWORKS

By combining the force-extension relation of single semiflexible polymers with a Langevin equation to capture the dissipative dynamics of chains moving through a viscous medium we study the dynamical response of crosslinked biopolymer materials. We find that at low frequencies the network deformations are highly non-affine, and show a low plateau in the modulus. At higher frequencies, this non-affinity decreases while the elastic modulus increases. With increasing frequency, more and more non-affine network relaxation modes are suppressed, resulting in a stiffening. This effect is fundamentally different from the high-frequency stiffening due to the single filament relaxation modes [13], not only in terms of its mechanism but also in its resultant scaling: $G'(\omega) \sim \omega^{\alpha}$ with $\alpha > 3/4$. This may determine nonlinear material properties at low, physiologically relevant frequencies.

5.1 Introduction

Tissues and cells alike owe many of their key mechanical properties to crosslinked architectures of supramolecular protein polymers [4, 5]. These biomaterials display remarkably rich viscoelastic characteristics, and moreover physiological stresses, strains and strain rates are such that they readily enter nonlinear regimes [7, 8, 11, 16, 87]. Indeed, many of these nonlinear properties are presumably employed to enhance and optimize tissue functionality. In the frequency domain, previous work has established the existence of various regimes as we discussed in section 1.2: at the lowest frequencies, crosslinking proteins reversibly bind and unbind, leading to viscous behavior [11]. At very high frequencies, on the other hand, the single filament relaxation dynamics become dominant and lead to a characteristic $\omega^{3/4}$ scaling of the stiffness with frequency [9, 13], similar to the high-frequency behavior found in entangled networks [14, 87–89]. In this chapter, we explore the behavior of rigidly crosslinked networks at intermediate timescales - those on which the crosslinking proteins may be assumed to be fixed, but the frequencies are still in the regime where all single-filament modes can relax completely. In this regime, a third, fundamentally different spectrum of relaxation modes dominates: those collective modes that effect non-affine deformations to globally minimize the elastic energy. Prior work has established that in the low-frequency limit, networks with fixed crosslinks deform in a manner that suppresses single filament stretching by such non-affine reorientations [32, 33, 35]. These modes, however, require that polymers move relative to the embedding medium, and while they may help minimize the elastic energy they are simultaneously *dynamically* impeded by hydrodynamic friction. At relatively high frequencies, therefore, we expect these non-affine modes to be dynamically suppressed. In this chapter we focus on the transition regime - the regime where the network crosses over from non-affine to affine. Our results for $G'(\omega)$ agree qualitatively with those reported in very recent numerical investigations [90], but expand on these in two ways: we report the first results on the *nonlinear* elastic properties and we correlate the mechanical behavior in this regime to the extent of the non-affinity. This non-affinity is, for the first time, studied as a function of applied external frequency and shows a convincing downward trend with increasing frequency that confirms our interpretation.

This chapter is organized as follows: starting from computer generated three dimensional semiflexible meshworks we begin by explaining the the Langevin method for implementing the relevant dynamical effects. We measure dynamical moduli for typical parameter values, and then relate it to the dynamical non-affinity. We identify different mechanical/dynamical regimes and probe the nonlinear response at large amplitude oscillatory shear.

We generate our networks as discussed in chapter 2. The primary biomaterial of our interest is crosslinked actin. Due to the time consuming method used to model the network response we restrict ourselves to averages over four individual and distinct networks with a representative set of parameters, that are chosen to reflect typical networks in experiments and cells. Our networks have a protein density of 0.65

mg/ml, a persistence lenght ℓ_p of 16 μm and an average contour length $\langle \ell_c \rangle = 1.0$ μm between crosslinks. The average length of filaments is $\langle L \rangle = 6.0$ μm and the diameter of the filaments is $b = 7$nm. Although the parameters in our simulation are chosen to reflect actin, the non-affine-to-affine transition we identify is completely generic and qualitatively independent of parameter choices. We therefore believe our results to carry over to a wider range of biopolymer networks.

5.2 Network dynamics

We model the dynamics of these networks by connected segments that are dragged through a viscous medium and experience random thermal forces due to collisions with solvent molecules. We neglect the spatial and temporal correlations of these collisions, and effectively impose Rouse dynamics. At the intermediate timescales that we are interested in, the crosslinkers do not move along the filaments and we do not take into account the binding and unbinding of linker proteins. The elasticity of individual segments is taken to obey the semiflexible wormlike chain (WLC) model, which takes into account the thermal fluctuations of the internal degrees of freedom of the individual segments. Note that we do not keep track of these internal degrees of freedom, but replace the actual thermal semiflexible WLC by a nonlinear spring with an identical force-extension relation. Again, we are allowed to do so because of the intermediate frequency regime we explore: we make sure that frequencies do not significantly exceed the slowest single filament mode. The dynamics of a segment in a viscous medium at finite temperature may be described by the Langevin equation:

$$\zeta \cdot \vec{v} = \vec{F} + \vec{f}_{\text{th}}, \tag{5.1}$$

where ζ is the drag tensor of the segment and $\vec{v}$, $\vec{F}$ and $\vec{f}_{\text{th}}$ are 3-dimensional vectors representing respectively the velocity of the segment, the elastic force on the segment and the random thermal force on the segment. To calculate the drag on the segments, we assume the segments to be slender rods with diameter b. The drag tensor encodes the dependence of the drag coefficient on the orientation of a rod and, in addition, depends on the length ℓ_c of the rod and the viscosity of the medium, which we take to be water with $\eta = 10^{-3}$ Pa·s. The axial drag coefficient $\zeta_{||}$, the perpendicular drag coefficient $\zeta_\perp$ and the rotational drag coefficient $\zeta_\top$ are then respectively given by [91]:

$$\zeta_{||} = \frac{2\pi\eta\ell_c}{\ln(\ell_c/b)},\ \zeta_\perp = \frac{4\pi\eta\ell_c}{\ln(\ell_c/b)},\ \zeta_\top = \frac{\pi\eta\ell_c^3}{3\ln(\ell_c/b)}. \tag{5.2}$$

In our simulations, we discretize (5.1) for small steps Δt as:

$$\begin{aligned} \vec{x}_i(t+\Delta t) &= \left\langle \frac{F_{||}}{\zeta_{||}} + \frac{F_\perp}{\zeta_\perp} + \frac{(\vec{r}_i \times F_\top) \times \vec{r}_i}{\zeta_\top} + \frac{2F_s}{\zeta_{||}} \right\rangle \Delta t \\ &+ g_{||} + g_\perp + g_\top + g_s + \vec{x}_i(t) \end{aligned} \tag{5.3}$$

where $\vec{x}_i(t)$ is a 3-dimensional vector representing the coordinates of the center of mass of the segment in the network at time t. The computer program keeps track of

the crosslinker positions; the position x_i of segment i is simply the average of the positions of the two crosslinkers at the ends of this segment, and the end-to-end vector $\vec{r}_i$ of segment i is the difference in these crosslinker positions. $F_{||}$ is the force along the filament, $F_{\perp}$ the force perpendicular to the segment, $F_{\top}$ the force that rotates the filament and F_s the force that stretches/compresses the filament. Note that the drag coefficient of this compressional force is half of the axial drag coefficient. The thermal random force f_{th} is represented by $\vec{g}$, a Gaussian fluctuation with standard deviation s. To ensure proper statistical sampling, we choose $s_i = \sqrt{\frac{2k_{\text{B}}T\Delta t}{\zeta_i}}$ which ensures that detailed balance is obeyed in the limit of small time steps.

The size of the time step Δt is determined by the stiffest mode and depends on the length of the segments. In our networks we typically take $\Delta t = 0.1$ ns. After generation we thermalize our networks during 0.1 s - we assume that all relevant length scales are relaxed in that time.

Inherent to this simulation approach is the assumption that the internal degrees of freedom of individual segments are equilibrated at all times. Based upon the behavior of a single WLC, the dispersion relation may be computed to be [13]:

$$\omega(q_n) = \frac{\kappa}{\zeta} q_n^4 = \frac{\kappa}{\zeta}\left(\frac{n\pi}{\ell_c}\right)^4. \tag{5.4}$$

Here, κ is the bending stiffness, from which the persistence length may be extracted as $\ell_p = \kappa/(k_{\text{B}}T)$, and ℓ_c is the segment length. At frequencies $\omega \gg \omega(q_1)$, clearly, the assumption of fully relaxed internal degrees of freedom would break down. In this regime the viscous modulus is expected to scale as $G' \sim \omega^{3/4}$ [13]. We avoid the regime where $\omega \gg \omega(q_1)$, by subdividing the segments in our networks into a finer mesh at high frequencies. Effectively, this brings the slowest internal segment modes into play - these are now explicitely tracked in our simulations. In this manner, we continue to add interpolating nodes until the relaxation times of all segments do not exceed the deformation times of the networks significantly. Typically, the number of added nodes is 5% of the total number of nodes for $f = \omega/2\pi = 400$ Hz and 80% of the total number of nodes for $f = 40$ kHz. As a result of the added nodes, the simulation timestep must be reduced while at the same time, the number of degrees of freedom increases. This renders the simulations computationally considerably more demanding, even though obviously the time per oscillation decreases linearly with frequency.

The end result is a computational model in which the single segments are purely elastic, and the network as a whole is a viscoelastic solid. In the following we analyze the dynamic viscoelastic response of these networks. We do this in a regime that precedes, but must connect up to the frequency range over which the effects of single-filament dynamics were studied in prior work [9, 13].

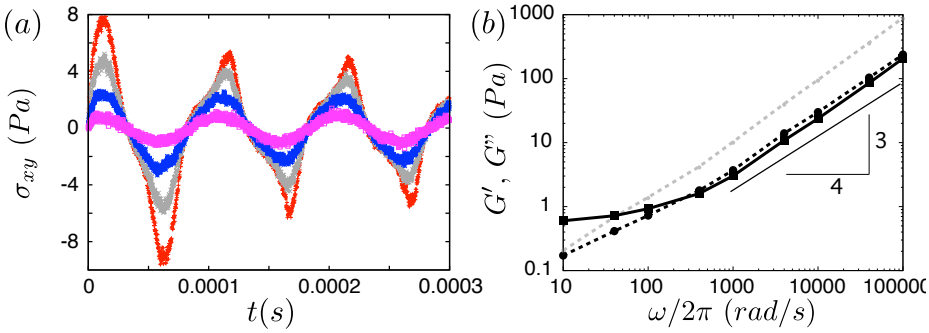


Figure 5.1: The dynamical network response. a) The shear stress σ_{xy} during oscillatory network shear with frequency $\omega = 2\pi 10^4$ rad/s, for shear amplitudes of γ_0=0.02, 0.06, 0.10 and 0.14. b) Elastic modulus (solid black curve) and viscous modulus (dotted black curve) as a function of frequency. The dotted grey curve indicates the viscous modulus when the dynamical viscosity of the liquid is included. Data shown are averages over four networks realizations. Black line depicts an exponent of 3/4.

5.3 Dynamic moduli in shear

In linear viscoelastic response, materials are characterized - among other equivalent representations - in terms of their dynamic moduli, the elastic modulus $G'(\omega)$ and the viscous modulus $G''(\omega)$. To measure these quantities in our simulations we apply an oscillatory shear deformation $\gamma = \gamma_0 \sin(\omega t)$ with shear amplitude γ_0, during which we monitor the motion of the segments. We also measure the shear stress in the network, defined as

$$\sigma_{xy} = \frac{1}{V}\frac{\partial E}{\partial \gamma}, \tag{5.5}$$

as well as the normal stress, given by

$$\sigma_{zz} = \frac{1}{V}\frac{\partial E}{\partial \alpha}, \tag{5.6}$$

where V is the volume of the box, E is the network energy and α is a superimposed, virtual uniaxial strain in the z-direction - the direction perpendicular to the shear. In detail, each step consists of an affine displacement of all segments in the network to accommodate for the global shear, as well as evolution over the time increment Δt as specified in equation (5.3). Thus we simulate the network response under the assumption that in the limit of high frequencies the local shear deformation at any place in the network is equal to the global shear. In experiments, there might be shear banding or similar effects that lead to a non-uniform distribution of the bulk strain over the cross section of the sample - we do not capture such effects.

5.4 Measurements of G' and G''

Figure 5.1a presents some typical curves of the shear-stress response on shearing, for different values of the shear amplitude γ_0 and a fixed frequency. In each simulation, we evolve the network over three full oscillations. As shown in this figure, small shear amplitudes give rise to a sinusoidal stress-response, while with increasing shear amplitude the stress response becomes increasingly nonlinear (but less noisy), confirming experimental observations [18]. We compute the network moduli at shear amplitudes ranging from 0.02 for high frequencies up to 0.2 at low frequencies, each time making sure that we are still in the linear regime.

We fit the time-dependent stress with $\sigma_{xy}(t) = \sigma_0 \sin(\omega t + \delta)$ and obtain the elastic and viscous moduli respectively from $G' = \sigma_0/\gamma_0 \cos(\delta)$ and $G'' = \sigma_0/\gamma_0 \sin(\delta)$. Figure 5.1b shows the network moduli as a function of frequency. We see that the elastic modulus plateaus at low frequencies, and steeply increases for high frequencies. This is similar to what was reported both for experiments and similar simulations [9, 90]. For the higher frequencies investigated, we find $G' \sim \omega^{\alpha}$, where α is larger than 3/4 as expected for the high frequency limit [13]. Our data are more consistent with $\alpha \approx 1$. Even for the smallest strain amplitudes, which was used to calculate the network moduli, the stress response shows a slight decreasing trend with increasing number of oscillations; we verified, in longer simulations over nine oscillations for the higher frequencies, that this influences our measurements in figure 5.1b by at most 6%. Thus far, the shear viscosity due to the solvent is not included; it would simply contribute an extra stress term $\sigma^{\eta}_{xy} = \eta\dot{\gamma}$. This shear viscosity of the liquid affects only G'' and not G'. It does, however, trivially affect the crossover frequency where G'' and G' are equally large, as shown in figure 5.1b. At high frequencies, as expected, the shear viscosity due to the solvent becomes the dominant contribution in G''.

5.5 Dynamical suppression of non-affinity

Another aspect of the network response on oscillatory shear deformation is the non-affine motion of components of the network. The non-affinity is measured by

$$\tilde{A}(t) = \left\langle (x(t) - x(0))^2 \right\rangle, \tag{5.7}$$

evaluated at a given strain γ. This non-affinity is plotted as a function of time in figure 5.2a. We observe a global increase in the non-affinity, accompanied by an oscillatory trend with a frequency directly related to the applied shear. We may in this case distinguish a thermal and a deformational component of the non-affinity. Without shear, $\tilde{A}(t)$ simply measures the mean square displacement of a crosslinker, which at finite temperature will by itself produce a non-affinity that increases with time. On top of that there is an oscillatory component tracking the externally imposed deformation. Thus far, the non-affinity of a network has been tied uniquely to the bending dominated response of the filaments to a global shear deformation [32, 33, 35, 54]. The figure, however, shows also a steadily increasing background non-affinity on top

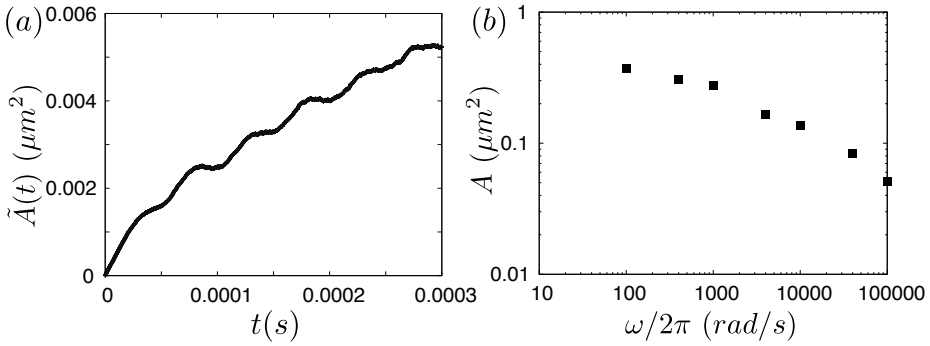


Figure 5.2: The non-affinity of the networks during oscillatory shear. a) The non-affine deformation $\tilde{A}(t)$, as defined in equation (5.7), for network oscillation with frequency $\omega = 2\pi 10^4$ rad/s. b) The shear non-affinity A, as defined in the text, as a function of frequency. Data shown are averages over four networks realizations.

of this contribution, caused by thermal fluctuations of the segments in the viscous medium. The contribution of these non-affine motions can be large in comparison with the shear component of the non-affinity. To the best of our knowledge, there is no general way to separate out the thermal component of the non-affinity such that one measures only the non-affinity due to shear; in simulations with thermal motion the filaments explore a large phase-space, and the average position of the filaments depends largely on the time-window of the simulations. It is important to realize that these thermal non-affine fluctuations are not just an artefact of our method but a genuine phenomenon that will also be present in experiments. To characterize the frequency dependence of the shear component of the non-affinity we calculate the average amplitude of the oscillations on top of the thermal non-affinity, since these oscillations are a direct consequence of the oscillatory shear. To facilitate a comparison of the results for different frequencies, we divide this amplitude by the squared shear amplitude γ_0^2. This results in the shear non-affinity measure A, similar to the one used in previous simulations and experiments [9, 35, 54]. A value of $A = 1$ μm^2 means that the average non-affine displacement at a shear of 1 equals 1 μm; note that this is not a special point. Figure 5.2b shows the shear non-affinity as a function of frequency. As does the stress response, also the shear non-affinity decreases slightly after the first couple of oscillations, by at most 25%. The data points at the lowest frequencies are omitted: for such low frequencies it becomes impossible to separate the oscillations from the thermal background non-affinity.

Interestingly, we observe a decreasing shear non-affinity with increasing frequency. Apparently, with increasing frequency the non-affine relaxation of the network is increasingly prohibited. Prior simulations have revealed the relation between non-affine reorientations and the network stiffness: non-affine reorientations allow

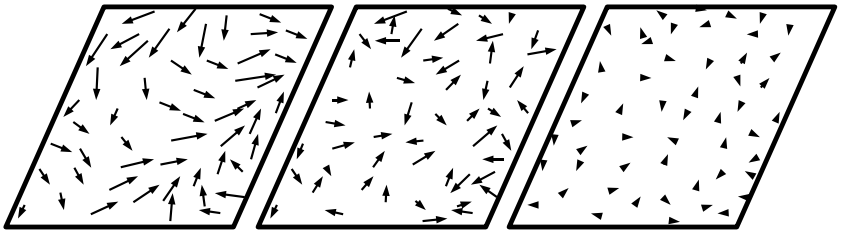


Figure 5.3: An illustration of the network response in a (two-dimensional) network during shear. The arrows show the deviation from affine displacements of the crosslinks. a) At frequencies below ω_n, all network modes can fully relax. The deviation from affine displacement is large and spatially correlated. b) At frequencies larger than ω_n the slowest (extended) network modes cannot relax but the localized (fast) network modes can, as well as the single filament modes. The non-affine displacements are smaller and no longer spatially correlated. c) At frequencies above ω_s, both the localized network modes and the single segment modes cannot relax and the network deforms more and more affinely.

the networks to minimize their energy and, therefore, systems that can access all non-affine modes are mechanically soft [54]. We conclude from figure 5.2b that with increasing frequencies the networks have less time to relax in this manner, which explains both the decreasing non-affinity (figure 5.2b) and the increasing stiffness (figure 5.1b) with increasing frequency. In the following section we will put this relation between network stiffness and the non-affinity in a broader perspective.

5.6 Classification of regimes

The current view presented in literature [9, 13, 14] is that there is a characteristic frequency ω_s, determined by the typical relaxation time of the single segments (see equation 5.4); above this frequency, the segments have no time to fully relax during the oscillatory shear, and the network is microscopically out of equilibrium. Assuming affine motion of the solvent, as is appropriate for small typical inter-plate distances, we assume that the network, too, will deform affinely in this regime. The lack of single-segment relaxation results in a stiffening of the network modulus, which is both computed and measured to scale as $\omega^{3/4}$. Below this frequency, the single segments can relax, the network is assumed to deform affinely, and this yields a plateau in G'.

Our results show a richer picture, which also has some important differences. In agreement with the literature view, above ω_s the single segments are out of equilibrium and the network response is dominated by their behavior. We distinguish a second characteristic frequency $\omega_n < \omega_s$, set by the long wavelength modes of network

deformation - those with the longest relaxation times. Between ω_n and ω_s, the single segments have time to relax, but the slowest network modes do not. Upon lowering the driving frequency, starting from ω_s, more and more network modes are able to relax during the oscillatory shear, and the elastic modulus G' will therefore slowly converge to its plateau value, but only reach this at ω_n when *all* modes are fully equilibrated. Because of the polydispersity of the segment lengths, there is no clean definition of ω_s; however, since the average segment length is 1 μm, typically the segments do no longer fully relax above $\omega_s \approx 50$ kHz (see also [13]). Similarly, because of the large distribution of the eigenfrequencies of the network, see chapter 4, there is no clean definition of ω_n either. However, our guess for our networks would be around $\omega_n \approx 10$ Hz, since both G' in figure 5.1b and A in figure 5.2b start to saturate around this value. We find that for high frequencies $G \sim \omega^\alpha$ with $\alpha > 3/4$, whereas a response dominated by the single segment relaxation would have $\alpha = 3/4$. Intuitively, it makes sense that with decreasing frequency the elasic modulus drops faster than expected purely on single filament response: on top of the single segment relaxation also the network relaxes more and more.

The non-affinity follows an opposite trend. Starting from affine behavior at frequencies above ω_s, as more and more modes are able to relax from the affine deformation induced by the oscillatory shear, the non-affinity will increase to its plateau value at slow shear. We know that the slow, low frequency modes are highly delocalized, while the fast, high frequency modes are localized [92]. Therefore, both the amplitude and the spatial correlation of the non-affine displacements will increase with decreasing frequency. Figure 5.3. illustrates this scenario of the three distinct regimes, by showing the non-affine displacements during deformation of a two-dimensional network in each regime.

5.7 Large shear amplitudes

Sofar, we studied the network response to oscillatory shear, in the regime of linear response. We now turn to a unidirectional constant shear rate up to a much larger shear amplitude of 0.5. We simulate the shear response for three different shear rates, namely $\dot{\gamma} = 10^2$ s^{-1}, 10^3 s^{-1} and 10^4 s^{-1}, averaged over four different network realizations. In these calculations we leave out the dynamical viscosity of the liquid. Figure 5.4a shows the shear stress response as a function of shear for these different shear rates. As can be seen, all networks show shear-stiffening. With increasing shear rates the initial stiffness increases, as expected from the increasing elastic modulus with frequency in figure 5.1b, and the onset of stiffening occurs at smaller strains γ. These results fit well to our picture for the small-strain regime. For low shear rates, the networks have a lot of time to accomodate the deformation, thus leading to a soft network response. Stretching of single segments can be postponed till large shears, which causes a late onset of stiffening. For large shear rates the times are too short to relax, leading to a stiff network response. The small strain at which the networks starts to stiffen indicates that the filaments get stretched already at small shears.

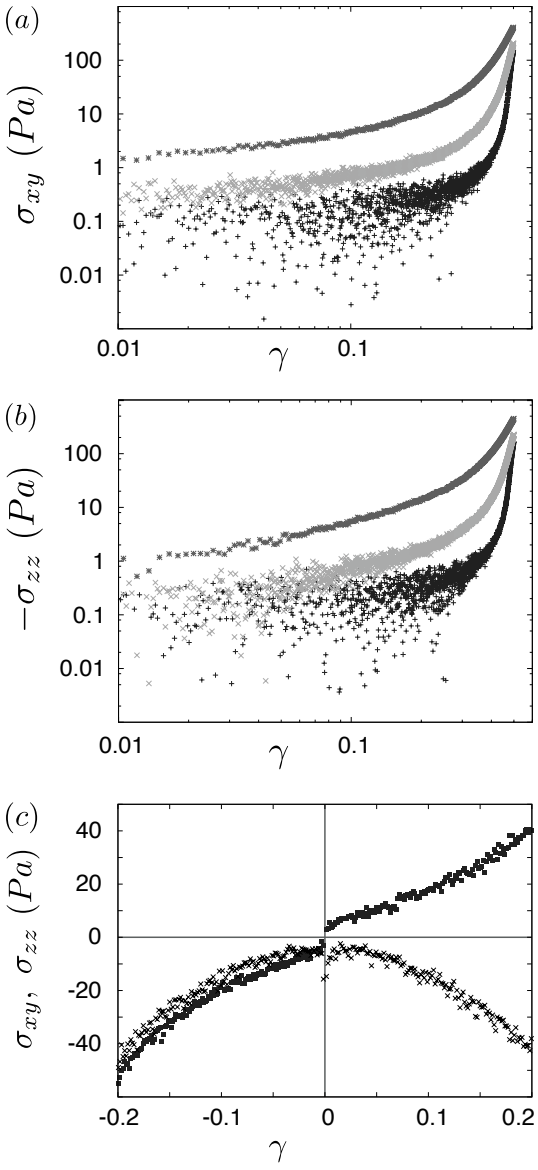


Figure 5.4: The network response for large shear. a) The shear stress σ_{xy} as a function of shear, for three different (non-oscillatory) shear rates $\dot{\gamma} = 10^2$ s^{-1} (lower), 10^3 s^{-1} (middle) and 10^4 s^{-1} (top curve). b) The normal stress σ_{zz} as a funtion of shear, for the same three shear rates. c) The shear stress (odd function of strain) and normal stress (even function of strain) for a network which is initially well-relaxed at zero strain, and then subsequently sheared in the direction of positive as well as negative strain, at a shear rate of $\dot{\gamma} = 10^4 \mathrm{s}^{-1}$.

We also calculate the normal stress σ_{zz} during deformation as a function of shear. A negative normal stress is one of the hallmark features of nonlinear mechanical response in biopolymer networks [52]. We find that σ_{zz} is indeed negative and shows the same shear-rate dependence as the shear stress, see figure 5.4b.

Because of symmetry, the shear stress and normal stress should be odd and even functions of the shear strain, respectively; figure 5.4c shows that this is the case in our simulations.

Our results may be relevant for the appropriate interpretation of nonlinear rheological data. Two methods have been developed to measure the differential stiffness at large strains and there has been some debate whether they will give the same results. One method measures the stiffness by superposing a small amplitude oscillatory shear $\partial\gamma$ for a constant applied shear γ [18]. This method allows for a relaxation of all network modes at the constant shear γ, after which the small amplitude oscillatory shear is applied. The alternative for measuring the large strain response is to apply a shear with constant shear rate [93]. Here, the shear rate determines whether the networks modes can or cannot relax. Although for slow deformation these two methods might give similar results, our results suggest that for fast deformation they will certainly not.

5.8 Relation to prior work

In the last decades, many simulational, modeling and experimental efforts have focused on understanding the zero-frequency response of networks with fixed crosslinks. These studies revealed that both the non-affinity and the network stiffness depend strongly on the network geometry: increasing the number of crosslinks per filament strongly decreases the floppiness of the structure and thus decreases the non-affinity and increases the modulus. Another important parameter is the relative filament stiffness, captured well by the ratio between the persistence length and the segment length. Increasing this ratio increases the relative importance of the non-affinity on the network response, and a low ratio implies floppy segments and thus a response that is dominated by an (affine) stretching of single segments [19, 23, 32, 35, 54, 92]. Complementary to these dependencies on filament stiffness and network structure, in this chapter we presented the *frequency* dependence of the network modulus and the non-affinity. This frequency dependence response related to the non-affinity is mostly relevant for networks deforming highly non-affinely in the zero-frequency limit. Clearly, networks deforming close to affinely in the zero-frequency limit will not show this characteristic non-affine to affine transition for increasing frequencies. Note that the theory of the frequency dependent deformation by MacKintosh *et al* [13] assumes affine behavior in the zero frequency limit, and thus does not fully describe the frequency dependence of materials in which the zero-frequency behavior is non-affine.

On the other side of the frequency spectrum, the work presented in this chapter is bounded from below by the work of Lieleg *et al.* [11], who consider the dynamical re-

sponse of a network with crosslinkers that may bind and unbind. We do not consider this effect, as the timescale for such processes (typically $\omega < 1$ Hz) is generally larger than the characteristic timescales of the non-affine reorientations.

A similar simulation method has recently been proposed and implemented by Kim and coworkers [90] to study the viscoelastic response of actin networks. The work presented in this chapter differs from theirs in several important respects: we distinguish different components of the drag coefficient, take into account the full force extension curve of individual segments and measure the dynamic non-affinity. Interestingly, they observe a similar increase in the network modulus with increasing frequency in networks with zero prestrain. In the highly prestrained networks they proceed to consider, the frequency dependence of the elastic modulus vanishes. This is exactly the behavior we expect for a network that loses the configurational freedom to relax by non-affine reorientations due to the high prestresses in the filaments.

5.9 Conclusions

In summary, we have developed a simulation approach to study the response of crosslinked networks of biopolymers to dynamical shear. Our main finding is that at low frequencies, all network modes and single filament modes are free to relax and consequently the network will deform non-affinely such that the networks are soft. With increasing frequencies the externally imposed strain outruns the internal relaxation modes, the non-affinity decreases and consequently the network stiffens. At even higher frequencies, beyond those studied here, even the single segments modes can no longer relax fully, and the network response is dominated by the single segment relaxation. While the transition itself is generic, its exact location in frequency space is not - we find that this is highly sensitive to filament and network parameters such as the persistence length, the density and average length of filaments, and the viscosity of the medium.

Bibliography

[1] A. Carlsson, Annu. Rev. Biophys. **39**, 91 (2010).

[2] N. Watanabe and T. Mitchison, Science **295**, 1083 (2002).

[3] P. Vallotton, G. Danuser, S. Bohnet, J. Meister, and A. Verkhovsky, Mol. Biol. Cell **16**, 1223 (2005).

[4] B. Alberts, A. Johnson, J. Lewis, M. Raff, K. Roberts, and P. Walter, *Molecular biology of the cell* (Garland Science, New York, NY U.S.A., 2008).

[5] H. Lodish, A. Berk, S. Zipursky, P. Matsudaire, D. Baltimore, and J. Darnell, *Molecular cell biology* (W.H. Freemand and Company, New York, 2000).

[6] Y. Fung, *Biomechanics: Mechanical Properties Of Living Tissues* (Springer-Verlag, New York Heidelberg Berlin, 1981).

[7] K. Kasza, A. Rowat, J. Liu, T. Angelini, C. Brangwynne, G. Koenderink, and D. Weitz, Curr. Opin. Cell Biol. **19**, 101 (2007).

[8] L. Deng, X. Trepat, J. Butler, E. Millet, K. Morgan, D. Weitz, and J. Fredberg, Nat. Mater. **5**, 636 (2006).

[9] G. Koenderink, M. Atakhorrami, F. MacKintosh, and C. Schmidt, Phys. Rev. Lett. **96**, 138307 (2006).

[10] Y. Luan, O. Lieleg, B. Wagner, and A. Bausch, Biophys. J. **94**, 688 (2008).

[11] O. Lieleg, M. Claessens, Y. Luan, and A. Bausch, Phys. Rev. Lett. **101**, 108101 (2008).

[12] C. P. Broedersz, M. Depken, N. Y. Yao, M. R. Pollak, D. A. Weitz, and F. C. MacKintosh, Phys. Rev. Lett. **105**, 238101 (2010).

[13] F. Gittes and F. MacKintosh, Phys. Rev. E **58**, R1241 (1998).

[14] D. Morse, Phys. Rev. E **58**, 1237 (1998).

[15] C. Storm, J. Pastore, F. MacKintosh, T. Lubensky, and P. Jamney, Nature **435**, 191 (2005).

[16] P. Janmey, S. Hvidt, J. Lamb, and T. Stossel, Nature **345**, 89 (1990).

[17] H. Sim, K. Ahn, and S. Lee, J. Non-Newt. Fluid. Mech. **112**, 237 (2003).

[18] M. Gardel, J. Shin, F. MacKintosh, L. Mahadevan, P. Matsudaira, and D. Weitz, Science **304**, 28 May (2004).

[19] J. Liu, G. Koenderink, K. Kasza, F. MacKintosh, and D. Weitz, Phys. Rev. Lett. **98**, 198304 (2007).

[20] Q. Wen, A. Basu, J. Winer, A. Yodh, and P. Janmey, New. J. Phys. **9**, 428 (2007).

[21] W. Ellenbroek, E. Somfai, M. van Hecke, and W. van Saarloos, Phys. Rev. Lett. **97**, 258001 (2006).

[22] M. van Hecke, J. Phys. Cond. Matt. **22**, 033101 (2010).

[23] C. Heussinger and E. Frey, Phys. Rev. E **75**, 011917 (2007).

[24] C. Heussinger and E. Frey, Phys. Rev. Lett. **97**, 105501 (2006).

[25] A. Levine, D. Head, and F. MacKintosh, J. Phys. Cond. Matt. **16**, S3079 (2004).

[26] B.A.DiDonna and T. Lubensky, Phys. Rev. E **72**, 066619 (2005).

[27] F. MacKintosh, J. K as, and P. Janmey, Phys. Rev. Lett. **75**, 4425 (1995).

[28] J. Kas, H. Strey, M. Barmann, and E. Sackmann, Eur. Phys. Lett. **21**, 865 (1993).

[29] O. Kratky and G. Porod, Recl. Trav. Chim. Pays-Bas **68**, 1106 (1949).

[30] C. Storm and P. Nelson, Phys. Rev. E **67**, 051906 (2003).

[31] H. Amuasi and C. Storm, Proc. 5th Inter. Conf. on Multiscale Mat. Modeling (2010).

[32] D. Head, A. Levine, and F. MacKintosh, Phys. Rev. E **68**, 061907 (2003).

[33] J. Wilhelm and E. Frey, Phys. Rev. Lett. **91**, 108103 (2003).

[34] P. Onck, T. Koeman, T. van Dillen, and E. van der Giessen, Phys. Rev. Lett. **95**, 178102 (2005).

[35] E. Huisman, T. van Dillen, P. Onck, and E. van der Giessen, Phys. Rev. Lett. **99**, 208103 (2007).

[36] C. Heussinger, B. Schaefer, and E. Frey, Phys. Rev. E **96**, 031906 (2007).

[37] M. Newman and G. Barkema, *Monte Carlo methods in Statistical Physics* (Oxford University Press, Oxford New York, 1999).

[38] D. Sokolis, E. Kefaloyannis, M. Kouloukoussa, E. Marinos, H. Boudoulas, and P. Karayannacos, J. of Biomech. **39**, 1651 (2006).

[39] J. Wilhelm and E. Frey, Phys. Rev. Lett. **77**, 2581 (1996).

[40] J. Marko and E. Siggia, Macromolecules **28**, 8759 (1995).

[41] F. Wooten, K. Winer, and D. Weaire, Phys. Rev. Lett. **54**, 1392 (1985).

[42] G. Barkema and N. Mousseau, Phys. Rev. B **62**, 4985 (2000).

[43] X. Liu and G. Pollack, Biophys. J. **83**, 2705 (2002).

[44] A. Bausch and K. Kroy, Nat. Phys. **2**, 231 (2006).

[45] P. Janmey and D. Weitz, Trends Biochem. Sci. **29**, 7 (2004).

[46] L. Black, P. Allen, S. Morris, P. Stone, and B. Suki, Biophys. J. **94**, 1916 (2008).

[47] P. Bullough and J. Goodfellow, J. Bone Jt. Surg. **50**, 852 (1968).

[48] K. Schmoller, O. Lieleg, and A. Bausch, Phys. Rev. Lett. **101**, 118102 (2008).

[49] K. Schmoller, O. Lieleg, and A. Bausch, Soft Matter **4**, 2365 (2008).

[50] D. Ingber, J. Cell Sci. **116**, 1157 (2003).

[51] J. Mizushima-Sugano, T. Maeda, and T. Miki-Noumur, Biochimica and biophysica acta **755**, 257 (1983).

[52] P. Janmey, M. McCormick, S. Rammensee, J. Leight, P. Georges, and F. MacKintosh, Nat. Mater. **6**, 48 (2007).

[53] J. Astrom, J. Makinen, M. Alava, and J. Timonen, Phys. Rev. E **61**, 5550 (2000).

[54] E. Huisman, C. Storm, and G. Barkema, Phys. Rev. E **78**, 051801 (2008).

[55] J. Xu, Y. Tseng, and D. Wirtz, J. Biol. Chem **275**, 35886 (2000).

[56] C. Broedersz, C. Storm, and F. MacKintosh, Phys. Rev. Lett. **101**, 118103 (2008).

[57] H. Wada and Y. Tanaka, Eur. Phys. Lett. **87**, 58001 (2009).

[58] F. Gittes, B. Mickey, J. Nettleton, and J. Howard, J. Cell Biol. **120**, 923 (1993).

[59] S. Torquato, *Random Heterogeneous Materials* (Springer, ADDRESS, 2002).

[60] D. Ingber, J. Cell Sci. **104**, 613 (1993).

[61] J. C. Maxwell, Philos. Mag. **27**, 27 (1864).

[62] J. Straley, Phys. Rev. B **15**, 5733 (1977).

[63] C. Heussinger and E. Frey, Eur. Phys. J E **24**, 47 (2007).

[64] O. Lieleg, M. Claessens, C. Heussinger, E. Frey, and A. Bausch, Phys. Rev. Lett. **99**, 088102 (2007).

[65] A. Missel, M. Bai, W. Klug, and A. Levine, Phys. Rev. E **82**, 041907 (2010).

[66] C. Heussinger, (To be published).

[67] E. Elson, Annu. Rev. Biophys. Biophys. Chem. **17**, 397 (1988).

[68] J. Wilhelm and E. Frey, Phys. Rev. Lett. **91**, 108103 (2003).

[69] J. Phillips, J. of Non-Cryst. Solids **43**, 37 (1981).

[70] M. F. Thorpe, J. of Non-Cryst. Solids **57**, 355 (1983).

[71] M. F. Thorpe, D. Jacobs, M. Chubynsky, and J. Phillips, J. of Non-Cryst. Solids **266-260**, 859 (2000).

[72] W. Zachariasen, J. Am. Chem. Soc. **54**, 3842 (1932).

[73] A. Liu and S. Nagel, Nature **396**, 21 (1998).

[74] L. Silbert, A. J. Liu, and S. Nagel, Phys. Rev. Lett. **95**, 098301 (2005).

[75] L. Silbert, A. J. Liu, and S. Nagel, Phys. Rev. E **79**, 021308 (2009).

[76] J. C. Maxwell, Philosophical Magazine **27**, 294 (1865).

[77] N. Morone, T. Fujiwara, K. Murase, R. Kasai, H. Ike, S. Yuasa, J. Usukura, and A. Kusumi, J. Cell. Biol. **174**, 851 (2006).

[78] H. He and M. Thorpe, Phys. Rev. Lett. **54**, 2107 (1985).

[79] D. E. Ingber, Sci. Am. Jan. **278**, 48 (1998).

[80] D. Stamenovic and D. E. Ingber, Soft. Matt. **5**, 1137 (2009).

[81] C. R. Calladine, Int. J. Solids Structures **14**, 161 (1977).

[82] D. J. Jacobs and M. F. Thorpe, Phys. Rev. E **53**, 3682 (1996).

[83] M. V. Chubynsky and M. F. Thorpe, Phys. Rev. E **76**, 041135 (2007).

[84] D. Head, F. MacKintosh, and A. Levine, Phys. Rev. E **68**, 025101 (2003).

[85] O. Stenull and T. Lubensky, (To be published).

[86] I. Piechocka, M. Bacabac, M. Potters, F. MacKintosh, and G. Koenderink, Biophys. J. **98**, 10 (2010).

[87] S. Yamada, D. Wirtz, and S. Kuo, Biophys. J. **78**, 1736 (2000).

[88] F. Gittes, B. Schnurr, P. Olmsted, F. MacKintosh, and C. Schmidt, Phys. Rev. Lett. **79**, 3286 (1997).

[89] F. Amblard, A. Maggs, B. Yurke, A. Pargellis, and S. Leibler, Phys. Rev. Lett. **77**, 4470 (1996).

[90] T. Kim, W. Hwang, H. Lee, and R. Kamm, PLoS comput. biol. **5**, 7 (2009).

[91] M. Doi and S. Edwards, *The Theory of Polymer Dynamics* (Oxford University Press, Oxford, 1986).

[92] E. Huisman and T. C. Lubensky, Phys. Rev. Lett. **106**, 088301 (2011).

[93] R. Tharmann, M. Claessens, and A. Bausch, Phys. Rev. Lett. **98**, 088103 (2007).

SAMENVATTING

De biofysica kan worden beschouwd als het grensgebied tussen de natuurkunde en de biologie. In dit vakgebied worden natuurkundige methoden gebruikt om biologische systemen te analyseren en doorgronden. Enkele voorbeelden van biologische systemen waar biofysici zich mee bezig houden zijn het doorgeven van signalen tussen cellen, de structuur van cellen, de structuur van weefsels en de manieren waarop DNA is opgevouwen in de celkern. In dit proefschrift richten we onze aandacht op de structurele eigenschappen van cellen en weefsels. Deze structurele eigenschappen worden grotendeels bepaald door netwerken van biopolymeren, en het zijn deze systemen die we in dit proefschrift analyseren.

Cellen bestaan uit een celwand en een celkern. Tussen de celwand en de celkern zit een ruimte die onder andere gevuld is met een vloeistof. Naast deze vloeistof bevinden zich in deze ruimte ook veel polymeren. Polymeren zijn lange moleculen die bestaan uit een reeks van soortgelijke delen, die aan elkaar vast zitten. Deze polymeren kunnen een netwerk vormen door verbindingen te maken met elkaar. In cellen bevinden zich speciale moleculen, een bepaald type eiwitten, die verbindingen tussen de polymeren kunnen vormen. Door het vormen van netwerken krijgt de cel een zekere stijfheid. Deze netwerken zijn dynamisch en kunnen continu van vorm veranderen, onder invloed van chemische reacties in de cel. De polymeren kunnen groeien en krimpen, de verbindingen tussen polymeren kunnen worden gevormd of juist weer los gaan en de verbindingen tussen de polymeren kunnen heel stijf zijn of juist heel erg slap. Ook kunnen verschillende soorten polymeren worden gevormd in de cel. Doordat deze netwerken zo dynamisch zijn en er veel verschillende ingrediënten zijn, kan een cel zich continu aanpassen aan de omgeving en functie die de cel op dat moment heeft. Zo kan een cel stijf zijn als dat nodig is, maar juist ook heel zacht, kan een cel bewegen of stilstaan, kan de vorm van een cel uitgerekt zijn of juist heel compact.

Behalve in cellen zijn er ook veel structuren buiten cellen waarbij dit soort netwerken een belangrijke rol spelen. Vaak zijn deze structuren groter dan enkele cellen en hebben cellen ook een plaats in deze structuren. Een bekend voorbeeld is de huid, die bestaat uit cellen en lange polymeren die met elkaar verbonden zijn, zoals collageen en elastine. Door het collageen en elastine is de huid elastisch en vervormbaar, een eigenschap die we continu gebruiken bijvoorbeeld bij het vormen van een glimlach of het aanraken van een object. Hoewel het weinig moeite kost om de huid enigszins

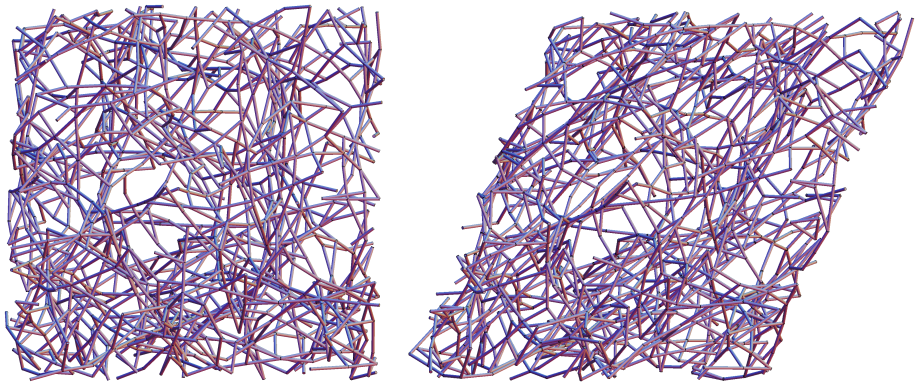
te vervormen, wordt de huid bijzonder stijf bij grotere vervormingen. Uit onderzoek is gebleken dat deze eigenschap deels toe te schrijven is aan de eigenschappen van de biopolymeren en de structuren die deze biopolymeren vormen.

Veel onderzoek is gedaan om de eigenschappen van individuele biopolymeren in kaart te brengen. In levende netwerken worden de biopolymeren omringt door een vloeistof. Op lichaamstemperatuur bewegen de moleculen in de vloeistof continu, waarbij ze ook regelmatig tegen de biopolymeren aanstoten. Daardoor krijgen de biopolymeren steeds kleine duwtjes, die de vorm van het biopolymeer steeds een beetje veranderen. Doordat het biopolymeer steeds een beetje van vorm verandert, is het bijna nooit perfect recht. Immers, er zijn heel veel mogelijke vormen die het polymeer kan aannemen, en de rechte vorm is daar slechts één van. Naast de temperatuur van de vloeistof bepaalt ook de stijfheid van het polymeer de vorm van het polymeer. Als een polymeer erg stijf is, dan hebben de thermische bewegingen van de vloeistofmoleculen minder effect op de vorm van het polymeer dan wanneer het polymeer zacht is. Als een polymeer wordt uitgerekt, dan worden de vervormingen door de duwtjes van de moleculen uit het polymeer getrokken. Omdat er continu moleculen tegenaan blijven botsen, zal het polymeer de neiging hebben weer te vervormen. Om deze vervorming tegen te gaan, is een kracht nodig.

Om de eigenschappen van de biopolymeer netwerken in cellen en buitencellulaire structuren beter te begrijpen, worden veel experimenten gedaan aan deze netwerken. Zo worden bijvoorbeeld hele cellen in een meetapparaat geplaatst, waarmee het effect van het uitoefenen van een kracht of vervorming op de cel wordt bekeken. Omdat de netwerkstructuren in biologische materialen en cellen erg complex zijn, is het vaak lastig een direct verband te leggen tussen de lokale structuur van het netwerk en het gedrag van het netwerk bij vervorming. Om beter inzicht te krijgen in deze relaties, worden in experimenten ook vaak speciaal geprepareerde netwerken gebruikt, waarbij de experimentator bepaalt welke polymeren en welke verbindingen tussen de polymeren worden gebruikt. Doordat deze netwerken vaak veel simpeler zijn, is het makkelijker om een verband te leggen tussen netwerk structuur en netwerk gedrag. Maar ook hier blijken de experimentele technieken vaak nog niet voldoende om de microstructuur precies in kaart te brengen, en een causaal verband te leggen tussen structuur, polymeer eigenschappen en het gedrag van het gehele netwerk.

In dit proefschrift worden de resultaten gepresenteerd van numeriek onderzoek naar het gedrag van netwerken van biopolymeren als ze vervormd worden. Computersimulaties worden ook wel omschreven als experimenten op de computer. In de computersimulaties genereren we netwerken waarvan de microstructuur volledig bekend is. Ook schrijven we het gedrag van de individuele polymeren in deze netwerken precies zo voor als we ze kennen uit de biologie. Deze netwerken kunnen worden vervormd, waarbij we de stijfheid van het hele netwerk berekenen, maar ook precies volgen wat er gebeurt met alle individuele filamenten en wat hun bijdrage is aan het gedrag van het netwerk als geheel. Op die manier helpen computersimulaties bij het interpreteren van experimentele gegevens en vergroten zo het inzicht in het gedrag van biopolymeernetwerken.

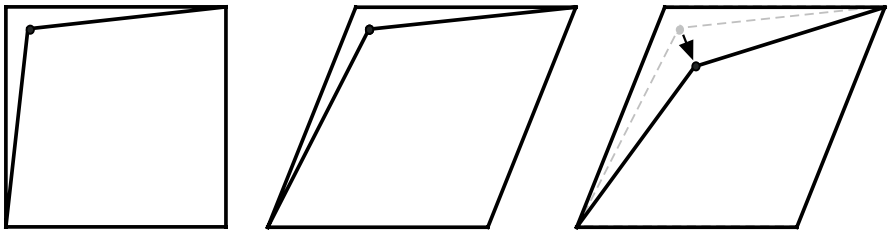
Volgens een specifieke procedure genereren we netwerken die bestaan uit lange



Figuur 6.1: Afbeelding van één van onze netwerken. (a) De netwerken zitten in een driedimensionale box. Als een filament door de rand van een box gaat, dan gaat hij aan de andere kant van de box verder. Dit noemen we periodieke randvoorwaarden. Door deze constructie hebben we geen last van de randen. Onze netwerken bestaan uit ongeveer 1000 crosslinks tussen filamenten. We kunnen de relatieve lengte van de filamenten variëren, evenals de relatieve stijfheid van de filamenten. (b) Hetzelfde netwerk terwijl het een schuifvervorming van 0.4 heeft ondergaan. De posities van alle crosslinks zijn zodanig dat de energie minimaal is in het netwerk.

polymeren die op verschillende plaatsen met elkaar verbonden zijn. Deze verbindingen noemen we crosslinks. We gebruiken de modellen die zijn ontwikkeld om het gedrag van losse biopolymeren te beschrijven, om het gedrag van de stukken polymeer tussen de crosslinks te beschrijven. Daarnaast houden we rekening in ons model met het feit dat twee stukjes van een filament die naast elkaar liggen maar van elkaar gescheiden zijn door een crosslink, toch de neiging hebben om rechtdoor te lopen en geen grote hoeken ten opzichte van elkaar te maken. Figuur 6.1a laat een voorbeeld zien van een netwerk zoals het eruit ziet na generatie.

Deze netwerken kunnen we vervormen. In experimenten wordt de bovenkant van de netwerken verschoven ten opzichte van de onderkant. Deze manier van vervormen wordt ook wel een schuifvervorming genoemd, figuur 6.1b geeft hiervan een illustratie. Tijdens de vervorming kunnen we de energie in het netwerk berekenen. De mate waarin de energie toeneemt met toenemende vervorming is een maat voor de stijfheid van het netwerk. Ook kunnen we de verplaatsingen van alle crosslinks in het netwerk volgen. Dit geeft aan hoeveel beweging er is in het netwerk. We vergelijken de verplaatsingen van de crosslinks met de verplaatsing van de crosslinks als alle crosslinks precies de opgelegde vervorming in het netwerk zouden volgen. Dit laatste noemen we de affiene vervorming. Het verschil tussen de affiene verplaatsing en de werkelijke verplaatsing van de crosslinks noemen we de niet-affiniteit van het netwerk. Figuur 6.2 geeft met behulp van een illustratie uitleg over het begrip niet-



Figuur 6.2: De niet-affiniteit in een simpel netwerk. (links) Simpel netwerk bestaande uit twee veren, die elk aan een hoek van een vierkant vastzitten, en aan elkaar vastzitten. Het vierkant wordt vervormd door de bovenkant te verschuiven ten opzichte van de onderkant. Als alle punten in het vierkant de opgelegde vervorming volgen, dan noemen we dat een affiene vervorming. Deze situatie is geïllustreerd in het middelste figuur. In deze situatie wordt de ene veer uitgerekt en de andere veer samengedrukt. Dat betekend dat de energie in het vierkant hoger wordt dan in de rusttoestand. Als alle punten in het vierkant een dusdanige positie mogen kiezen zodanig dat de totale energie van het systeem zo laag mogelijk is, dan zal de positie van de crosslink zodanig zijn dat beide veren uitgerekt noch samengedrukt worden (situatie in rechter figuur). Nu volgt de crosslink niet meer de opgelegde vervorming, maar wijkt daar van af. Het verschil tussen de affiene vervorming (middelste figuur) en de werkelijke vervorming (rechter figuur) is aangegeven met de pijl. De grootte van deze pijl is een maat voor de hoeveelheid niet-affiniteit in het netwerk.

affiniteit.

Uit onze simulaties blijkt dat de netwerken veel zachter worden, als we ze toestaan om niet-affien te vervormen. De niet-affiene beweging verlaagt de energie van het netwerk. Hierdoor kost het minder energie om de netwerken te vervormen, en worden ze dus zachter. De mate van niet-affiniteit in een netwerk hangt sterk af van de netwerkstructuur. Netwerken met lange filamenten met veel crosslinks per filament zullen over het algemeen minder niet-affien bewegen, dan netwerken met korte filamenten en weinig crosslinks per filament. In het laatste geval zitten de individuele filamenten minder vastgebonden in het netwerk, waardoor ze meer ruimte hebben om te bewegen. Daarnaast zien we ook dat netwerken bestaande uit filamenten met een lage buigstijfheid, meer affien bewegen dan netwerken met een hoge buigstijfheid.

Veel biologische netwerken bestaan uit zowel stijve als slappe polymeren. Om beter te begrijpen waarom deze netwerken uit verschillende soorten polymeren bestaan, hebben we simulaties uitgevoerd van netwerken die bestaan uit twee soorten filamenten, namelijk filamenten met een hoge buigstijfheid en filamenten met een lage buigstijfheid. Onze simulaties laten zien dat deze filamenten samenwerken binnen een netwerk. Bij kleine vervormingen vangen de slappe polymeren een groot gedeelte van de totale vervorming op, waardoor de stijve polymeren bijna niet ver-

vormen. Bij grote vervormingen is dit niet langer mogelijk, en bepalen de stijve polymeren de uiteindelijke stijfheid van het netwerk. Door dit bijzondere samenspel tussen de stijve en slappe polymeren zijn de netwerken relatief zacht bij lage vervormingen en stijf bij hoge vervormingen.

Voor de stijfheid van een netwerk is ook bepalend hoe snel het netwerk wordt vervormd. De filamenten in het netwerk zijn omringt met een vloeistof. Net zoals het tijd kost om een touwtje door een bak water te trekken, zo kost het ook tijd om de netwerken in een vloeistof te vervormen. De relevante tijdschaal van een vervorming wordt onder andere bepaald door de viscositeit van de vloeistof, een fysische term die ook wel wordt vertaald als de stroperigheid. Om het effect van de snelheid van de vervorming op de gedrag van het netwerk onder deze vervorming goed te simuleren, voegen we in ons programma de viskeuze interactie tussen de polymeren en de vloeistof toe. Als we de netwerken nu met een hoge frequentie vervormen, dan zijn ze erg stijf. Als we ze heel traag vervormen, dan zijn de netwerken relatief zacht. Dit verschil tussen een stijve en trage vervorming zien we weerspiegeld in de niet-affiniteit. Bij hoog-frequente vervorming bewegen de netwerken bijna affien, terwijl bij laagfrequente vervorming de netwerken sterk niet-affien bewegen. Deze niet-affiniteit legt een link tussen de snelheid van de vervorming en de stijfheid van het netwerk. Bij lage frequenties heeft het netwerk veel tijd om zich aan te passen aan de opgelegde vervorming. Anders gezegd, het netwerk heeft veel tijd om een toestand met een lage energie te vinden. Hierdoor is het netwerk zacht en de niet-affiniteit hoog. Bij snelle frequenties heeft het netwerk nauwelijks tijd om zich aan te passen, en is het netwerk dus stijf en de niet-affiniteit laag.

De resultaten van onze netwerksimulaties laten het belang van de microstructuur en de niet-affiniteit zien voor de stijfheid van de netwerken. Deze nieuwe inzichten zijn belangrijk voor het juist interpreteren van experimentele resultaten. Onze resultaten geven meer inzicht op welke wijze cellen en weefsels hun elasticiteit regelen. Deze inzichten zijn niet alleen belangrijk voor het beter begrijpen van cellen en weefsels, maar kunnen ook worden gebruikt om cellen en weefsels te manipuleren of om biomimetische weefsels met de juiste eigenschappen te maken.

PUBLICATIONS

1. E.M. Huisman, T. van Dillen, P.R. Onck and E. van der Giessen *Three-dimensional cross-linked F-actin networks: Relation between network architecture and mechanical behavior*, Phys. Rev. Lett. **99**, 208103 (2007)

2. E.M. Huisman, A.L. Biance, A. Madouri, G. Patriarche, E. Bourhis, G. Oukhaled, L. Auvray and J. Gierak, *A new way to integrate solid state nanopores for translocation experiments*, Microelectronic Engeneering **85**, 1311 (2008)

3. E.M. Huisman, C. Storm and G.T. Barkema *Monte Carlo study of multiply crosslinked semiflexible polymer networks*, Phys. Rev. E. **78**, 051801 (2008) [Chapter 2].

4. E.M. Huisman, C. Heussinger, C. Storm and G.T. Barkema *Semiflexible Filamentous Composites*, Phys. Rev. Lett. **105**, 118101 (2010) [Chapter 3].

5. E.M. Huisman, C. Storm and G.T. Barkema *Frequency-dependent stiffening of semiflexible networks: A dynamical nonaffine to affine transition*, Phys. Rev. E. **82**, 061902 (2010) [Chapter 5].

6. E.M. Huisman and T.C. Lubensky *Internal stresses, normal modes and nonaffinity in three-dimensional biopolymer networks*, Phys. Rev. Lett. **106**, 088301 (2011) [Chapter 4].

7. E.M. Huisman, Q. Wen, Y.-H. Wang, K. Cruz, G. Kitensbergs, K. Erglis, A. Zeltins, A. Cebers and P.A. Janmey *Gelation of rodlike polyelectrolytes by multivalent counterions*, submitted (2010)

Curriculum Vitae

In 1982 ben ik geboren in Leeuwarden, waarna ik mijn jeugd doorbracht in Hardegarijp en in Drachten. Ik bezocht het Gomarus College in Drachten en Groningen, waar ik in het jaar 2000 mijn VWO diploma behaalde. In datzelfde jaar begon ik aan mijn studie Natuurkunde aan de Rijksuniversiteit Groningen. In 2006 deed ik een experimentele stage aan het onderzoekscentrum LPN-CNRS in Marcoussis, vlakbij Parijs. Hier ontwikkelde ik een nieuwe methode om bewerkte silicon nanowafers te gebruiken voor het maken van vaste stof nanogaatjes. In januari 2007 studeerde ik af in de Technische Natuurkunde op een onderzoek naar de vervorming van drie-dimensionele actine netwerken, onder de supervisie van prof. dr. ir. E. van der Giessen, prof. dr. ir. P. R. Onck en dr. ir. T. van Dillen. Naast natuurkunde studeerde ik ook wijsbegeerte van de Natuurwetenschappen, waarmee ik in 2001 begon. In 2006 studeerde ik af in de wijsbegeerte op een onderzoek over de (on)mogelijkheid van een volledige reductie van mentale toestanden naar breintoestanden, onder begeleiding van prof. dr. T. A. F. Kuipers en dr. A. M. Tamminga. Tijdens mijn studie was ik student-assistent bij het vak 'Fysische Methoden' voor studenten van kunstmatige intelligentie, voor het vak 'Logica 1' voor eerstejaars studenten filosofie en van het algemeen vormende vak 'Argumenteren en Redeneren'. In 2005 was ik studentlid van het opleidingsbestuur van het opleidingsinstituut 'Natuurwetenschappen en techniek'.

In 2007 startte ik met mijn promotieonderzoek aan het Instituut-Lorentz voor Theoretische Natuurkunde van de Universiteit Leiden. Hier werkte ik onder begeleiding van prof. dr. G. T. Barkema en dr. C. Storm aan een numeriek onderzoek over de vervorming van drie-dimensionele netwerken van biopolymeren, waarvan de belangrijkste resultaten vermeld zijn in dit proefschrift. In de herfst van 2009 werkte ik in het biofysische laboratorium van prof. dr. P. Janmey aan de University of Pennsylvania. In die tijd startte ook mijn samenwerking met prof. dr. T. C. Lubensky.

Tijdens mijn onderzoeksperiode heb ik deelgenomen aan scholen in Cargèse, Leuven, Driebergen en Heeg. Ik heb mijn werk gepresenteerd op internationale conferenties in Warwick (2x) en Amsterdam en op nationale conferenties in Veldhoven, Dalfsen, Heeg en Arnemuiden. Ook heb ik voordrachten over mijn werk gegeven in Philadelphia en Göttingen. Ik heb in Leiden werkcolleges gegeven voor de vakken 'Quantummechanica 1' en 'Statistische en Thermische Fysica 1'.

In het najaar van 2010 nam ik deel aan de Nationale DenkTank 2010, een multidisciplinair team dat concrete oplossingen aandroeg om de vertrouwensrelatie tussen publieke organisaties en de burger te verbeteren.

Dankwoord

Vanuit Parijs solliciteerde ik in de herfst van 2006 naar een promotieplek bij het Instituut-Lorentz. Een bezoek aan Leiden maakte mij enthousiast, voor zowel het onderwerp van het mogelijke onderzoek, de begeleiders en het instituut. Reden genoeg om te besluiten ook daadwerkelijk in Leiden mijn promotieonderzoek te starten. Gerard Barkema en Kees Storm, ik wil jullie bij deze hartelijk bedanken voor alle tijd, ideeën, kritiek en vrijheid die jullie mij steeds weer hebben gegeven.

I am grateful for all the inspiring meetings I attended with the people from the Physics of Soft and Biological Matter group of the Vrije Universiteit, the Biological Soft Matter group of AMOLF and the Soft Condensed Matter Theory group, the Granular and Disorderd Media group and the group of Theoretical Physics of Life Processes of the Universiteit Leiden. It was a privilege to have these opportunities to discuss the research in the field of biophysics and soft matter physics. Chase Broedersz, graag wil ik je bedanken voor je aangename gezelschap tijdens onze gezamelijke tripjes, en je aanstekelijke enthousiasme voor het onderzoek.

In the autumn of 2009 I spent a couple of months in Philadelphia. Paul Janmey, I would like to thank you for the opportunity you gave me to do experiments and enjoy the dynamics of working in a biological lab. My thanks to all the members of the group for the time they took to teach me how to perform experiments. It was also in Philadelphia that I started to collaborate with Tom Lubensky. Tom, I would like to thank you for all time you invested in our project.

Een van de kenmerkende eigenschappen van het Instituut-Lorentz is dat tijdens de lunch- en koffiepauzes de grenzen verdwijnen tussen onderzoeksgroepen en tussen studenten, promovendi, postdocs, vast personeel en hoogleraren. Een andere eigenschap zijn de vele taarttractaties en de heerlijke kerstlunches. Beiden zijn door mij zeer gewaardeerd. Fran Ouwerkerk en Marianne Gouw, graag wil ik jullie bedanken voor alle hulpvaardigheid, administratieve ondersteuning en vooral ook gezellig gebabbel de afgelopen jaren. Warme herinneringen heb ik aan het ski-weekendje in Zwitserland, de vele schaatstochten, het beachvolleyballen, tennissen, de SOLA-estafette, wandklimmen, stranduitjes en de borrels op vrijdagmiddagen, met steeds weer wisselende collega's. Mariya Medvedyeva, it was a great pleasure to be your housemate and officemate during the last years, thanks for your nice company.

Lieve vrienden, dank voor jullie vriendschap. Zusjes, het is een waar genoegen jullie zusje te zijn. En lieve ouders, dank voor alle vrijheid die jullie mij altijd hebben

gegeven bij het maken van keuzes. Dank voor alle vertrouwen dat jullie mij steeds weer schenken. En dank voor alle liefde en aandacht, waarmee ik mij steeds omringd weet.